UNCLASSIFIED

SECURITY CLASSIFICATION OF THIS PAGE *(When Data Entered)*

REPORT DOCUMENTATION PAGE		READ INSTRUCTIONS BEFORE COMPLETING FORM
1. REPORT NUMBER AFGL-TR-82-0049	2. GOVT ACCESSION NO.	3. RECIPIENT'S CATALOG NUMBER
4. TITLE *(and Subtitle)* A REVIEW OF MEASURED ATMOSPHERIC OPTICAL PROPERTIES AND THEIR CONTEMPORARY AEROSOL SIZE DISTRIBUTIONS		5. TYPE OF REPORT & PERIOD COVERED Final Report 1 OCT 78 - 30 SEP 81
		6. PERFORMING ORG. REPORT NUMBER SIO Ref. 82-22
7. AUTHOR(s) Richard W. Johnson Bruce W. Fitch		8. CONTRACT OR GRANT NUMBER(s) F19628-78-C-0200
9. PERFORMING ORGANIZATION NAME AND ADDRESS University of California, San Diego Visibility Laboratory La Jolla, California 92093		10. PROGRAM ELEMENT, PROJECT, TASK AREA & WORK UNIT NUMBERS 62101F 7670-14-01
11. CONTROLLING OFFICE NAME AND ADDRESS Air Force Geophysics Laboratory Hanscom AFB, Massachusetts 01731 Contract Monitor: Major John D. Mill/OPA		12. REPORT DATE December 1981
		13. NUMBER OF PAGES 78
14. MONITORING AGENCY NAME & ADDRESS*(if different from Controlling Office)*		15. SECURITY CLASS. *(of this report)* UNCLASSIFIED
		15a. DECLASSIFICATION/DOWNGRADING SCHEDULE

16. DISTRIBUTION STATEMENT *(of this Report)*

Approved for public release; distribution unlimited.

17. DISTRIBUTION STATEMENT *(of the abstract entered in Block 20, if different from Report)*

18. SUPPLEMENTARY NOTES

19. KEY WORDS *(Continue on reverse side if necessary and identify by block number)*

Scattering Coefficient Profiles
Sky Radiances
Terrain Radiances
Atmospheric Aerosols
Aerosol Size Distributions

20. ABSTRACT *(Continue on reverse side if necessary and identify by block number)*

This report summarizes the results of a data reduction and analysis program addressing optical atmospheric properties in the western European environment. The data were collected in a cooperative but independent effort associated with the NATO Research Study Group 8 of Panel IV, AC243 and their Program OPAQUE. The optical measurements were collected during the Winter and Summer seasons of 1978 in a variety of geographic locations in western and northern Europe.

DD FORM 1 JAN 73 1473 EDITION OF 1 NOV 65 IS OBSOLETE
S/N 0102-014-6601

UNCLASSIFIED

SECURITY CLASSIFICATION OF THIS PAGE *(When Data Entered)*

20. ABSTRACT continued:

The daytime optical measurements included, but were not limited to, total volume scattering coefficients plus sky and terrain radiances measured in four spectral bands within the visible spectrum. There were two moderately narrow bands having mean wavelengths of 478 and 664 nanometers, one slightly wider band at 765 nanometers, and one relatively broad band representing the photopic response having a mean wavelength of 557 nanometers. Optical data from approximately 45 flights were processed and reported during this contract interval, and pertinent aspects of these data are summarized in this Final Report.

Measurements of atmospheric aerosol size distributions were made during each interval for which there were measurements of sky and terrain radiance. Data representing over 670 aerosol size distributions covering particle radii from 0.2 to 5.9 micrometers were collected during the flight program. These size distributions have been characterized by three additive log-normal distributions, one for each of the three volume modes observed in the data. The behavior of the model parameters as a function of altitude, humidity, season, and geographic site of measurement are analyzed, and the results of these analyses are summarized.

AFGL-TR-82-0049 SIO 82-22

A REVIEW OF MEASURED ATMOSPHERIC OPTICAL PROPERTIES AND THEIR CONTEMPORARY AEROSOL SIZE DISTRIBUTIONS

Richard W. Johnson
Bruce W. Fitch

Visibility Laboratory
University of California, San Diego
Scripps Institution of Oceanography
La Jolla, California 92093

Approved:

Roswell W. Austin, Director
Visibility Laboratory

Approved:

William A. Nierenberg, Director
Scripps Institution of Oceanography

CONTRACT NO. F19628-78-C-0200
Project No. 7670
Task No. 7670-14
Work Unit No. 7670-14-01

Final Report
1 OCT 78 - 30 SEP 81
December 1981

Contract Monitor
Major John D. Mill, Atmospheric Optics Branch, Optical Physics Division

Prepared for

AIR FORCE GEOPHYSICS LABORATORY
AIR FORCE SYSTEMS COMMAND
UNITED STATES AIR FORCE
HANSCOM AFB, MASSACHUSETTS 01731

SUMMARY

This Final Report under Contract No. F19628-78-C-0200 summarizes the results of a data reduction and analysis program addressing optical atmospheric properties in the western European environment. The data were collected in a cooperative, but independent effort associated with the NATO Research Study Group 8 of Panel IV, AC243 and their Program OPAQUE.

The Aircraft Data Reduction effort, task one under this two part research contract has concentrated on the measurements of visible spectrum atmospheric optical properties, primarily scattering coefficient profiles plus sky and terrain radiances, that were collected during the Winter and Summer seasons of 1978. During this interval there were approximately 45 data flights conducted throughout western and northern Europe. Over 670 aerosol size distributions covering particle radii from 0.2 to 5.9 micrometers were measured contemporaneously with the measurements of sky and terrain radiances during these flights. Both the optical and aerosol data are reviewed in this report.

Several general characteristics of the volume scattering coefficient profiles are illustrated showing the Trapani, Sicily profiles as clearly different from those measured in northern Europe. The Trapani profiles show significantly less low altitude structure, often with a complete lack of any abrupt haze top. Summer hazes in this Mediterranean area remain heavy throughout the entire 6 kilometer altitude regime.

Very low altitude scattering coefficient profiles measured between ground level and approximately 700m AGL, representing all four temporal seasons and all northern and southern sites, indicate that in forty-seven out of fifty-four (87%) instances, the profile is essentially constant in value within this very low altitude regime during the middle to late afternoon measurement intervals.

A high degree of radiance symmetry and uniformity is illustrated for sky and terrain radiances measured under full overcast conditions. Conversely, under conditions of highly variable cloud cover, the measured sky and terrain radiances tend to fluctuate both above and below the radiance distribution of a clear sky by a factor of two or more in some instances, but in general remain within about ± 50 percent of the clear sky radiance for corresponding paths of sight.

Several experimental uncertainties associated with the measurement of high altitude scattering coefficients, and near sun sky radiances have been addressed, and corrective procedures have been devised to reduce the errors existing in the original measurements. The early evidences of stray light errors in the nephelometer data resulted in several mechanical modifications to the instrument, but continuing analysis indicated an additional residual error in the measurements. These analyses indicated that the error was most probably the result of incomplete aerosol exchange within the nephelometer sampling volume as the measurement altitude increased. It is clear that an incomplete flushing of only a fraction of one percent of the low altitude aerosol concentration can result in a substantial erroneous signal when the true high altitude concentration has dropped over an order of magnitude. The evidences from these analyses are consistent in their predictions of the true optical scattering ratios $Q(z)$ being 1.3 to 2.6 at 6 kilometers altitude, roughly half the measured values. Sky radiance measurements made by the automatic 2π scanner system were found to contain stray light errors which consistently increased markedly in magnitude both as the instruments field of view approached within 25° of the solar disc, and as the atmospheric aerosol loading decreased. An approach to the correction of these near-sun radiance values has been presented earlier in Johnson (1981).

The aerosol size distributions were analyzed using the $dV/d \log r$ volumetric format resulting in characterization by three additive log-normal distributions, one for each of the three volume modes observed in the data.

The accumulation mode ($\bar{r} = 0.25$ to $0.47\mu m$, $\sigma = 0.11$) is found almost always confined to the mixing layer, and appears more frequently in the data collected at the northern stations than those in the south. The middle mode ($\bar{r} = 0.45$ to $1.4\mu m$, $\sigma = 0.3$) occurs only in the mixing layer, appearing most often in Winter and when the relative humidity is greater than 70 percent. The course particle mode ($\bar{r} = 5\mu m$, $\sigma = 0.2$) can exist above or within the mixing layer, and shows no preference for season, but appears most often in the data from southern stations and when relative humidity is less than 70 percent.

The data and comparisons with aerosol models imply that the volume modes are associated with specific aerosol sources, and therefore, with the history of the airmass in which the aerosol sample was measured.

TABLE OF CONTENTS

LIST OF TABLES AND ILLUSTRATIONS

A REVIEW OF MEASURED ATMOSPHERIC OPTICAL PROPERTIES AND THEIR CONTEMPORARY AEROSOL SIZE DISTRIBUTIONS

Richard W. Johnson
Bruce W. Fitch

1. INTRODUCTION

This Final Report has been prepared under AFGL Contract No. F19628-78-C-0200 and addresses the first of two tasks enumerated under the terms of the contract, the reduction and publication of previously unprocessed raw data collected by an instrumented C-130 aircraft during the life of a flight program which terminated in September, 1978. The flight program, related to the measurement of atmospheric optical properties, was conducted by the Visibility Laboratory of the University of California, San Diego under the sponsorship of, and in cooperation with the Air Force Geophysics Laboratory, Hanscom AFB, Massachusetts.

The instrumentation and experimental procedures used in the collection of the raw data processed during this contract interval were reviewed and summarized in Duntley *et al.* (1978), and thus will receive only minimal additional comment at this time. The airborne instrument system is illustrated in Fig. 1-1.

The optical measurements, which consisted primarily of profiles of atmospheric volume scattering coefficient and 4π sky and terrain radiances, were made in several spectral bands throughout the visible spectrum as illustrated by the curves in Fig. 1-2. The experimental flights, which were associated with the NATO program OPAQUE, were made along flight tracks throughout several European regions as illustrated in Duntley *et al.* (1978) and as summarized in Fig. 1-3 and Tables 1.1 and 1.2 which have been abstracted from that earlier report.

In addition to the radiometric measurements made by the various radiometer systems illustrated in Fig. 1-1, there were airborne measurements of particle size distributions at each of several altitudes during each data flight. These distributions were measured over the range 0.2 to 5.9 micrometers (μm) in particle radius using a Royco model 220 particle counter. An initial discussion of these aerosol measurements was presented by Cress (1980), and by Fitch and Cress (1981).

In the following sections of this Final Report on the Aircraft Data Reduction task, we will summarize and review the data processed and published subsequent to the status reported in Duntley *et al.* (1978). Section II will present a discussion of the radiometric data, and Section III will contain an analysis of additional measurements of aerosol size distributions.

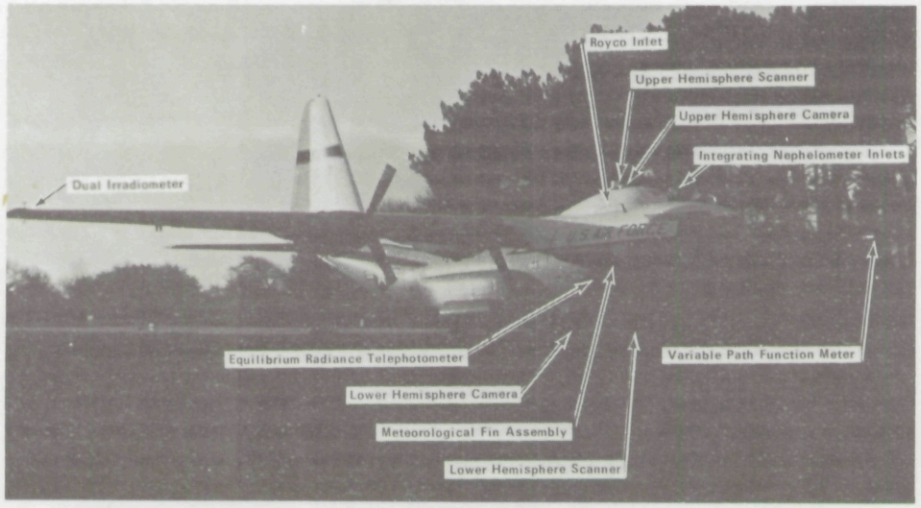

Fig. 1-1. C-130 airborne instrument system.

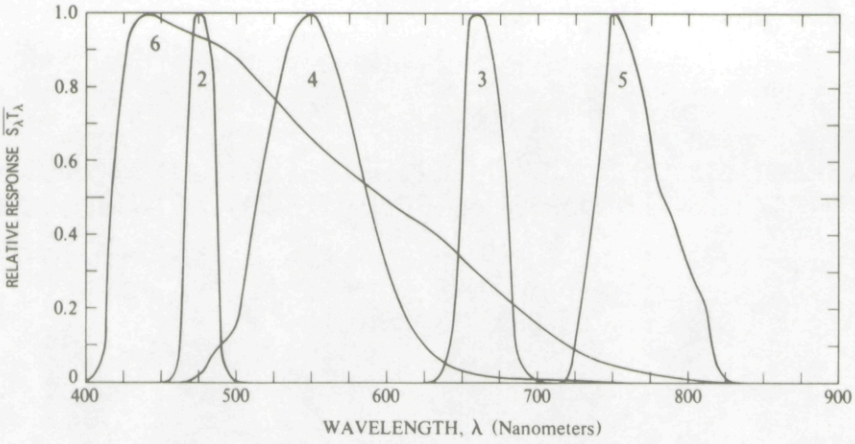

Fig. 1-2. Standard spectral responses. Peak wavelengths are: 2=475nm Blue, 3=660nm Red, 4=550nm Photopic, 5=750nm N.I.R., 6=440nm S-20.

Fig. 1-3. Typical OPAQUE flight tracks.

Table 1.1. Project OPAQUE Flight Track & Ground Sites Location & Ground Elevations.

Geographical Reference and Site Identification Code		Center of Flight Track		Ground Site		Approx Gnd Elev along track
		Latitude	Longitude	Latitude	Longitude	
Ground Sites						
Catania, Sicily	(CT)	-	-	37°24'N	14°55'E	-
Trapani, Sicily	(TR)	-	-	37°55'N	12°29'E	-
Bruz,France	(BR)	-	-	48°01'N	1°45'W	-
Birkhof, Germany	(BK)	-	-	48°13'N	9°11'E	-
Yeovilton, England	(YO)	-	-	51°01'N	2°37'W	-
Soesterberg, Netherlands	(SO)	-	-	52°08'N	5°17'E	-
Meppen, Germany	(MP)	-	-	52°52'N	7°23'E	-
Flight Tracks						
Sigonella, Sicily	(SG)	37°24'N	15°20'E	-	-	Sea Level
Trapani, Sicily	(TR)	37°33'N	12°30'E	-	-	Sea Level
Bruz, France	(BR)	48°01'N	1°41'W	-	-	50 m
Birkhof, Germany	(BK)	48°15'N	9°05'E	-	-	762 m
Yeovil, England	(YO)	50°56'N	2°27'W	-	-	60 m
Soesterberg, Netherlands	(SO)	51°56'N	5°35'E	-	-	6 m
Mildenhall, England	(ML)	52°24'N	1°41'E	-	-	Sea Level
Ahlhorn, Germany	(AL)	52°53'N	7°51'E	-	-	18 m.
Meppen, Germany	(MP)	53°00'N	7°37'E	-	-	18 m
Rodby, Denmark	(RB)	54°41'N	11°08'E	-	-	Sea Level

Table 1.2. Geographical Distribution of Project OPAQUE Data Flights.

Flight Track Ident	Attempted (and reported) Data Sequences				
	OPAQUE I Spring '76	OPAQUE II Fall '76	OPAQUE III Summer '77	OPAQUE IV Winter '78	OPAQUE V Summer '78
Sigonella, Sicily	0	0	0	2 (2)	0
Trapani, Sicily	0	0	0	3 (3)	4 (4)
Bruz, France	0	5 (5)	3 (3)	0	0
Birkhof, Germany	0	0	0	8 (7)	5 (4)
Yeovil, England	5 (3)	0	0	5 (5)	3 (3)
Soesterberg, Netherlands	1 (1)	0	1 (0)	2 (2)	3 (3)
Mildenhall, England	0	0	0	2 (2)	0
Ahlhorn, Germany	0	0	2 (2)	0	0
Meppen, Germany	5 (2)	4 (3)	3 (3)	3 (3)	3 (3)
Rodby, Denmark	2 (2)	4 (4)	4 (4)	2 (2)	2 (2)
TOTAL	13 (8)	13 (12)	13 (12)	27 (26)	20 (19)
Technical Report No.	AFGL-TR-77-0078	AFGL-TR-77-0239	AFGL-TR-78-0168	AFGL-TR 79-0159	AFGL-TR-80-0207

2. AIRBORNE RADIOMETRIC MEASUREMENTS

During the three year interval 1975-1978, there were five major overseas deployments of the airborne instrument system illustrated in Fig. 1-1 as an adjunct to the program OPAQUE. These five trips were planned to provide daytime atmospheric measurements as a function of altitude in the immediate vicinity of several different OPAQUE data stations. The plan was developed to ensure a reasonably diverse geographical sampling of vertical profile data during each of the four seasons of the year, Spring, Summer, Fall, and Winter. Data for the first three of these deployments was summarized and reviewed in Duntley *et al.* (1978). In a similar manner, the data from the last two deployments, Winter and Summer 1978 is summarized in the following paragraphs.

Table 1.1 lists the general location of each of the different flight tracks used during the OPAQUE deployments, and also the locations where the air transportable ground unit was established. The general locations are illustrated in Fig. 1-3, where the short, solid lines indicate the approximate orientation of each flight track. For further more detailed site location, the reader is referred to the site maps in Section 6 of Duntley *et al.* (1978).

2.1 Description of Winter and Summer Deployments

As a convenience to the reader, the deployment descriptions for the Winter 1978 and Summer 1978 field trips have been abstracted from Duntley *et al.* (1978), and reproduced below.

OPAQUE IV, WINTER 1978,
FLIGHT NOS. C-430 THROUGH C-456
AFGL-TR-79-0159

The Winter deployment began with the Visibility Laboratory team departing San Diego on Wednesday, 25 January 1978. The team returned on Monday, 10 April 1978. During this 72 day deployment, the longest of those up to this time, the joint Air Force and Visibility Laboratory team operated the aircraft out of four different bases in three different countries, not counting the initial staging into Rhein-Main Air Base. Two new bases, never before visited during the OPAQUE related missions, were added to the itinerary, one in Sicily and one in southern Germany. The chronological listing of the operational bases utilized during the OPAQUE IV deployment is shown below:

Order Visited	Staging Base Ident	Geographical Location
1.	Rhein-Main Air Base	near Frankfurt, Germany
2.	Sigonella Naval Air Facility	near Catania, Sicily
3.	Memmingen Air Base	S-W of Munich, Germany
4.	Mildenhall Air Base	N-W of Cambridge, England
5.	Wunstorf Air Base	near Hannover, Germany

The only major instrumentation modification implemented for the OPAQUE IV deployment was with respect to the MEMORY cutoff system. This modification was flown in prototype during OPAQUE III. The improved performance of the dual irradiometer system upon which this modification had been retrofitted was so impressive that the decision to extend the modification to all systems was made immediately upon return to the Laboratory in September, 1977. The modification was accomplished on all of the airborne and ground based radiometer systems used by the Visibility Laboratory team during OPAQUE IV.

The fly-away ground station, which again included both the CRM and integrating nephelometer systems, was operational in the vicinity of all four of the primary OPAQUE flight tracks. While the aircraft operated out of Sigonella Naval Air Facility the ground station was located at Birgi Air Base near Trapani, Sicily. This base was the location for the Italian OPAQUE data site. When airborne operations moved to Memmingen Air Base, the ground station was relocated to Birkhof, Germany which is the location of the German OPAQUE data site. Only in the United Kingdom was the fly-away ground station not located on the official OPAQUE site. While the aircraft was operating out of Mildenhall Air Base the ground station was located at HMS Heron, Yeovilton Royal Naval Air Station, Yeovilton, England. This site, approximately 35 miles northwest from the British OPAQUE site at Christchurch, was chosen for its proximity to the actual flight track and for its suitability for air transport of the ground-based equipment to and from the site. When airborne operations returned to Germany out of Wunstorf Air Base, the ground fly-away ground station was relocated to the Meppen test range which was the site of the United States supported OPAQUE data site.

In spite of the bad weather conditions that were anticipated for this Winter deployment, OPAQUE IV was the most productive of all the OPAQUE series. The weather was exceptionally permissive as is indicated by the completion of twenty five missions. The spectrum of weather conditions encountered was exceptionally broad, ranging from reasonably cloud free with moderate haze to low ceilings with rain and snow.

OPAQUE V, SUMMER 1978
FLIGHT NOS. C-460 THROUGH C-479
AFGL-TR-80-0207

This, the second Summer deployment, similar in season to OPAQUE III, began with the Visibility Laboratory team departing San Diego on Friday, 28 July 1978. The team returned on Saturday, 30 September 1978. During the 64 day intervening period, the joint Air Force and Visibility Laboratory team operated the aircraft out of six different air bases in four different countries. This represents the largest number of bases ever utilized during a single deployment. However, since all of these bases had been visited before, there were no operational difficulties and the exceptional cooperation of the host nation personnel made the exercise a remarkably smooth and efficient experience. The chronological listing of the operational bases utilized during this final OPAQUE deployment is shown below:

Order Visited	Staging Base Ident	Geographical Location
1.	Rhein-Main Air Base	near Frankfurt, Germany
2.	Sigonella Naval Air Facility	near Catania, Sicily
3.	Wunstorf Air Base	near Hannover, Germany
4.	Memmingen Air Base	S-W of Munich, Germany
5.	Mildenhall Air Base	N-W of Cambridge, England
6.	Vaerlose Air Base	near Copenhagen, Denmark

There were no instrumentation modifications imposed during the preparations for the OPAQUE V deployment, only normal maintenance and overhaul. The fly-away ground station was operational at or near four of the five primary OPAQUE flight tracks. As during the preceding OPAQUE IV deployment, it was in operation on the official OPAQUE data site at Trapani/Birgi Air Base, Sicily, and at both the Meppen and Birkhof sites in Germany. Similarly, the ground station was located at Yeovilton while the aircraft was operating out of Mildenhall, England.

The weather was much more cooperative during this second Summer deployment than it had been during the first, OPAQUE III. Even though there were few truly clear days, there were many marred only by minor cloud and haze conditions. Consequently, of the nineteen total missions, ten of them were classified as "full profile" missions, *i.e.* four straight and level altitudes in a total of

four spectral bands. The remaining nine were assorted flights of lesser quality ranging all the way down to 5000 ft. ceilings with haze and light rain.

In a manner similar to that used in Duntley *et al.* (1978), a tabular summary of the pertinent descriptive information related to the OPAQUE IV and V data flights has been abstracted from the parent data report covering each of these two deployments (AFGL-TR-79-0159 and AFGL-TR-80-0207), and reproduced as Tables 2.1 and 2.2. The times listed under the "Total Time of Data Taking" column are Greenwich Mean Time (GMT) and Local Civil Time (LCT). The sun zenith angles are tabulated for the time when data taking began, at the time of sun transit (minimum sun zenith angle), and at the conclusion of the last data taking event. The maximum and minimum flight altitudes in meters AGL (Above Ground Level) are noted in columns 12 and 13. The filter identification numbers refer to the spectral responses illustrated in Fig. 1-2.

Table 2.1. Flight Data Summary for OPAQUE IV (AFGL-TR-79-0159).

Flight No.	Date (1978)	Total Time of Data Taking				Filter	Sun Zenith Angle (degrees)			Flight Altitude meters (AGL)	
		Start		End							
		GMT	LCT	GMT	LCT		Start	Transit	End	Min	Max
C-430	31 Jan	1449	1559	1506	1606	2	73.1	-	75.8	150	6060
		1512	1612	1531	1631	3	76.8	-	80.0	150	6030
		1536	1636	1553	1653	4	80.8	-	83.8	150	6030
		1558	1658	1614	1714	5	84.5	-	87.5	150	6030
C-431	1 Feb	1029	1129	1212	1312	2,3	56.2	54.7	55.9	90	4560
		1217	1317	1340	1440	4,5	56.1	-	63.4	120	2850
C-432	3 Feb	1229	1329	1412	1512	4,5,2,3	56.2	-	67.0	120	6060
C-433	17 Feb	1211	1311	1217	1317	2	51.2	-	51.6	150	1860
		1224	1324	1232	1332	3	52.2	-	52.9	150	1800
		1236	1336	1246	1346	4	53.1	-	54.0	150	1770
		1250	1350	1259	1359	5	54.4	-	55.4	150	1770
C-434	18 Feb	0940	1040	1126	1226	2,3	53.7	49.1	49.2	150	6120
		1132	1232	1325	1425	4,5	49.3	-	58.1	120	6150
C-435	23 Feb	0832	0932	0921	1021	2,3	71.0	-	65.2	90	2310
		0927	1027	1015	1115	4,5	64.8	-	60.9	180	2280
C-436	23 Feb	1322	1422	1403	1503	2,3	62.5	-	66.5	240	2100
		1412	1512	1452	1552	4,5	67.4	-	72.2	120	1770
C-437	27 Feb	0925	1025	1126	1226	2,3	63.6	-	56.7	150	5160
		1133	1233	1326	1426	4,5	56.6	56.6	61.6	60	5130
C-438	1 Mar	0902	1002	0926	1026	2	65.3	-	62.8	210	1650
C-439	1 Mar	1257	1357	1342	1442	2,3	58.6	-	62.3	30	1650
		1352	1452	1433	1533	4,5	63.3	-	68.0	0	1620
C-440	2 Mar	1100	1200	1252	1352	4,5	56.1	55.5	58.0	30	5340
		1259	1359	1453	1553	2,3	58.4	-	70.3	180	4350
C-441	3 Mar	1506	1606	1552	1652	2,3	71.7	-	78.4	60	5280
		1556	1656	1641	1741	4,5	79.0	-	86.1	90	5280
C-442	9 Mar	1243	1243	1301	1301	2	57.5	-	58.2	180	4650
		1303	1303	1322	1322	3	58.3	-	59.2	120	4620
		1323	1323	1346	1346	4	59.3	-	60.8	120	4710
		1347	1347	1404	1404	5	60.9	-	62.3	150	4710
C-443	9 Mar	1413	1413	1453	1453	2,3	63.1	-	67.2	150	930
		1459	1459	1537	1537	4,5	67.9	-	72.5	150	930
C-444	11 Mar	1259	1259	1411	1411	2,3	55.3	-	59.6	120	2190
		1415	1415	1521	1521	4,5	60.0	-	66.9	120	2460
C-445	13 Mar	1115	1215	1134	1234	2	55.3	-	55.0	90	4560
		1136	1236	1153	1253	3	54.9	54.9	54.9	90	4620
		1152	1252	1206	1306	4	54.9	-	55.0	90	1200
		1207	1307	1215	1315	5	55.0	-	55.2	90	1200
C-446	15 Mar	1116	1116	1158	1158	2,3	54.8	-	53.3	90	870
		1204	1204	1238	1238	4,5	53.2	53.1	53.3	150	810
C-447	15 Mar	1247	1247	1303	1303	2	53.4	-	53.9	90	3570
		1305	1305	1342	1342	3	54.0	-	56.0	90	3510
		1344	1344	1401	1401	4	56.1	-	57.4	150	3510
		1402	1402	1415	1415	5	57.5	-	58.6	120	3510
C-448	17 Mar	1118	1118	1146	1146	2	53.9	-	52.8	90	5970
		1147	1147	1212	1212	3	52.7	-	52.3	90	5970
		1211	1211	1238	1238	4	52.3	52.3	52.5	60	6000
		1240	1240	1259	1259	5	52.5	-	53.0	30	5970
C-449	18 Mar	0945	0945	1122	1122	2,3	61.3	-	53.2	150	4590
		1126	1126	1316	1316	4,5	53.1	51.9	53.4	150	6180
C-450A	22 Mar	0945	1045	1020	1120	2,3	57.2	-	54.4	90	4020
		1023	1123	1040	1140	4	54.1	-	53.1	120	3990
		1042	1142	1056	1156	5	53.0	-	52.4	120	4020
C-450B	22 Mar	1100	1200	1136	1236	2,3	52.2	-	51.4	180	1080
		1140	1240	1227	1327	4,5	51.3	51.3	52.1	120	1140

Table 2.1 (con't.). Flight Data Summary for OPAQUE IV (AFGL-TR-79-0159).

Flight No.	Date (1978)	Total Time of Data Taking				Filter	Sun Zenith Angle (degrees)			Flight Altitude meters (AGL)	
		Start		End							
		GMT	LCT	GMT	LCT		Start	Transit	End	Min	Max
C-451	22 Mar	1308	1408	1325	1425	2	55.7	-	57.0	120	4560
		1327	1427	1344	1444	3	57.2	-	58.7	180	4560
		1343	1443	1401	1501	4	58.6	-	60.3	150	4590
		1402	1502	1418	1518	5	60.4	-	62.1	90	4590
C-452	23 Mar	1429	1529	1452	1552	2	63.0	-	65.8	150	5220
		1453	1553	1518	1618	3	66.0	-	69.1	120	5220
		1516	1616	1528	1628	4	68.9	-	70.5	150	1140
		1530	1630	1540	1640	5	70.7	-	72.1	120	1020
C-453	28 Mar	0841	0941	0856	0956	2	61.5	-	59.8	120	3060
		0858	0958	0916	1016	3	59.6	-	57.6	60	3060
		0918	1018	0931	1031	4	57.5	-	56.2	120	3030
		0933	1033	0952	1052	5	56.0	-	54.4	120	3030
C-454	28 Mar	1046	1146	1213	1313	2,3	52.2	51.7	52.8	150	4230
		1217	1317	1346	1446	4,5	53.0	-	59.5	120	4260
C-456A	31 Mar	1303	1403	1340	1440	2,3	54.7	-	58.0	120	1200
		1344	1444	1416	1516	4,5	58.3	-	61.8	120	780
C-456B	31 Mar	1429	1529	1444	1544	2	63.2	-	65.0	30	3660
		1445	1545	1501	1601	3	65.2	-	67.2	120	3660
		1503	1603	1519	1619	4	67.4	-	69.5	120	3630
		1520	1620	1534	1634	5	69.7	-	71.6	120	3630

Table 2.2. Flight Data Summary for OPAQUE V (AFGL-TR-80-0207).

Flight No.	Date (1978)	Total Time of Data Taking				Filter	Sun Zenith Angle (degrees)			Flight Altitude meters (AGL)	
		Start		End							
		GMT	LCT	GMT	LCT		Start	Transit	End	Min	Max
C-460	2 Aug	1142	1342	1346	1546	2,3	20.6	-	38.5	120	6210
		1350	1550	1501	1701	4,5	39.1	-	52.9	150	6090
C-461	3 Aug	0858	1058	1037	1237	2,3	36.3	-	21.8	90	4680
		1043	1243	1206	1406	4,5	21.3	20.0	22.8	120	4320
C-462	5 Aug	0851	1051	1043	1243	2,3	37.8	-	21.6	90	6120
		1049	1249	1240	1440	4,5	21.4	20.6	27.8	90	6120
C-463	7 Aug	0928	1128	1110	1310	2,3	31.7	-	21.1	90	6090
		1118	1318	1256	1456	4,5	21.1	-	30.7	120	6090
C-464	14 Aug	1159	1259	1238	1338	2,3	37.7	-	39.2	90	2130
		1243	1343	1322	1422	4,5	39.5	-	42.6	90	1500
C-465	14 Aug	1358	1458	1434	1534	2,3	48.0	-	52.5	90	1500
		1440	1540	1510	1610	4,5	53.1	-	57.4	90	1290
C-466	15 Aug	0919	1019	1056	1156	2,3	47.1	-	39.6	90	6000
		1104	1204	1303	1403	4,5	39.4	38.9	42.8	90	5910
C-467	18 Aug	1116	1216	1257	1357	2,3	39.1	38.8	41.8	120	4710
		1302	1402	1435	1535	4,5	42.1	-	52.2	90	4710
C-468	21 Aug	0920	1020	1058	1158	2,3	48.6	-	41.4	120	5820
		1102	1202	1244	1344	4,5	41.3	40.9	43.3	120	6210
C-469	22 Aug	1158	1258	1337	1437	2,3	40.3	-	46.7	90	5820
		1342	1442	1527	1627	4,5	47.0	-	60.5	90	5880
C-471	11 Sep	0739	0839	0812	0912	2,3	64.0	-	59.0	0	540
		0818	0918	0850	0950	4,5	58.4	-	54.0	0	540
C-472	11 Sep	1235	1335	1342	1442	2,3	46.6	-	53.3	0	5280
		1346	1446	1457	1557	4,5	53.7	-	63.6	0	5250
C-473	11 Sep	1513	1613	1617	1717	2,3	65.8	-	76.3	270	870
		1548	1648	1623	1723	4,5	71.5	-	77.2	0	840
C-474	13 Sep	0914	1014	1100	1200	2,3	51.8	-	44.6	30	5490
		1104	1204	1301	1401	4,5	44.5	44.4	49.5	0	5460
C-475	15 Sep	1301	1401	1458	1558	2,3	49.3	-	60.1	150	6180
		1506	1606	1652	1752	4,5	61.0	-	76.5	180	6150
C-476	16 Sep	1050	1150	1255	1355	2,3	50.7	48.3	49.4	150	6180
		1301	1401	1451	1551	4,5	49.7	-	59.6	180	6150
C-477	18 Sep	1103	1203	1211	1311	2,3	50.7	49.0	49.1	120	3480
		1222	1322	1334	1434	4,5	49.2	-	52.7	120	3480

Table 2.2 (con't.). Flight Data Summary for OPAQUE V (AFGL-TR-80-0207).

Flight No.	Date (1978)	Total Time of Data Taking				Filter	Sun Zenith Angle (degrees)			Flight Altitude meters (AGL)	
		Start		End							
		GMT	LCT	GMT	LCT		Start	Transit	End	Min	Max
C-478	25 Sep	1346	1446	1505	1605	2,3	64.4	-	73.8	150	6150
		1512	1612	1615	1715	4,5	74.7	-	83.4	180	6060
C-479	26 Sep	0926	1026	1105	1205	2,3	59.6	-	55.9	120	4620
		1109	1209	1251	1351	4,5	55.9	-	59.9	150	4590

Table 2.3. OPAQUE Related Aircraft Data Reports.

Report No.	Deployment		Data Type
	Series	Date	
AFGL-TR-77-0078	I	Spring '76	Scattering Coefficient Profiles & Related Meteorology
AFGL-TR-77-0239	II	Fall '76	Scattering Coefficient Profiles & Related Meteorology
AFGL-TR-78-0168	III	Summer '77	Scattering Coefficient Profiles & Related Meteorology
AFGL-TR-79-0159	IV	Winter '78	Scattering Coefficient Profiles & Related Meteorology
AFGL-TR-80-0207	V	Summer '78	Scattering Coefficient Profiles & Related Meteorology
AFGL-TR-80-0192	I,II,III	See Above	Aerosol Size Distributions and Analysis
AFGL-TR-81-0154	IV,V	"	Scattering Coefficient Very Low Altitude Profiles
AFGL-TR-81-0237	I,II,III	"	Scattering Coefficient Very Low Altitude Profiles
AFGL-TR-81-0275	II,III,V	"	Sky and Terrain Radiances
AFGL-TR-81-0317	I—V	"	Variations in Sky and Terrain Radiances

2.2 Selected Sample Data

Flight data resulting from the five OPAQUE deployments have been presented in a series of AFGL Technical Reports which are identified in Table 2.3. In general the data presentation reports are of three types. The first containing primarily scattering coefficient profiles, the second sky and terrain radiances, and the third containing aerosol size distributions.

In order to provide a quick overview of the data processed subsequent to that presented in Duntley *et al.* (1978), portions of the original OPAQUE data reports have been reproduced and presented herein with additional but typical descriptive and analytic comment. For this summary presentation, only composite plots of pseudo-photopic volume scattering coefficient and temperature which have been sorted by geographical location are included as representative of the profile type reports. In a similar manner, several composite representations of the sky and terrain radiance plots are also included. For more complete information regarding these data, the reader is referred to the parent reports as listed in Table 2.3.

Temperature

Temperature is generally a function of latitude and season with an expected diurnal and weather variability during any one season at a given latitude. The temperatures measured during each flight's several profile elements are averaged by altitude into a composite plot which typifies that individual flight. These resultant average temperature profiles for the OPAQUE IV and V deployments have been sorted into sets representing similar latitudes and presented in Figs. 2-1 and 2-2. These in-flight temperatures can be profitably compared to temperatures from the U.S. Standard Atmosphere Supplements (1966) which are shown as solid lines on the plots in Figs. 2-1 and 2-2. It should be noted that the altitude scale in these figures is in meters above mean sea level (m MSL), and the ground elevations at the test sites range from 0 meters at Trapani, Sigonella, Mildenhall and Rodby, to 762 m at Birkhof.

As noted in the parent reports, the temperature profiles are reasonable for the season and latitude of the measurement, although there are significant examples of low and mid-level inversions at all sites.

Total Volume Scattering Coefficient

Total volume scattering coefficients, as measured with the filter 4 pseudo-photopic spectral response for the OPAQUE IV and V deployments, are presented in Figs. 2-3 and 2-4. These plots, which have been abstracted from the previously issued reports listed in Table 1.2, have been sorted in a manner similar to the preceding temperature plots *i.e.* by approximate latitude and season. One should note that the altitude scales in Figs. 2-3 and 2-4 are in meters above ground level (m AGL) rather than on the MSL scale used for the temperature plots. Also note that the horizontal scale spans three decades for all of the plots except 2-3d, which spans only two.

As discussed in the OPAQUE IV parent report, the degree of fine structure in the nephelometer data that can be attributed to instrumentation and system noise is not more than ±5% of the reading. However, as illustrated by the profiles representing flight C-432 in Fig. 2-3a, a

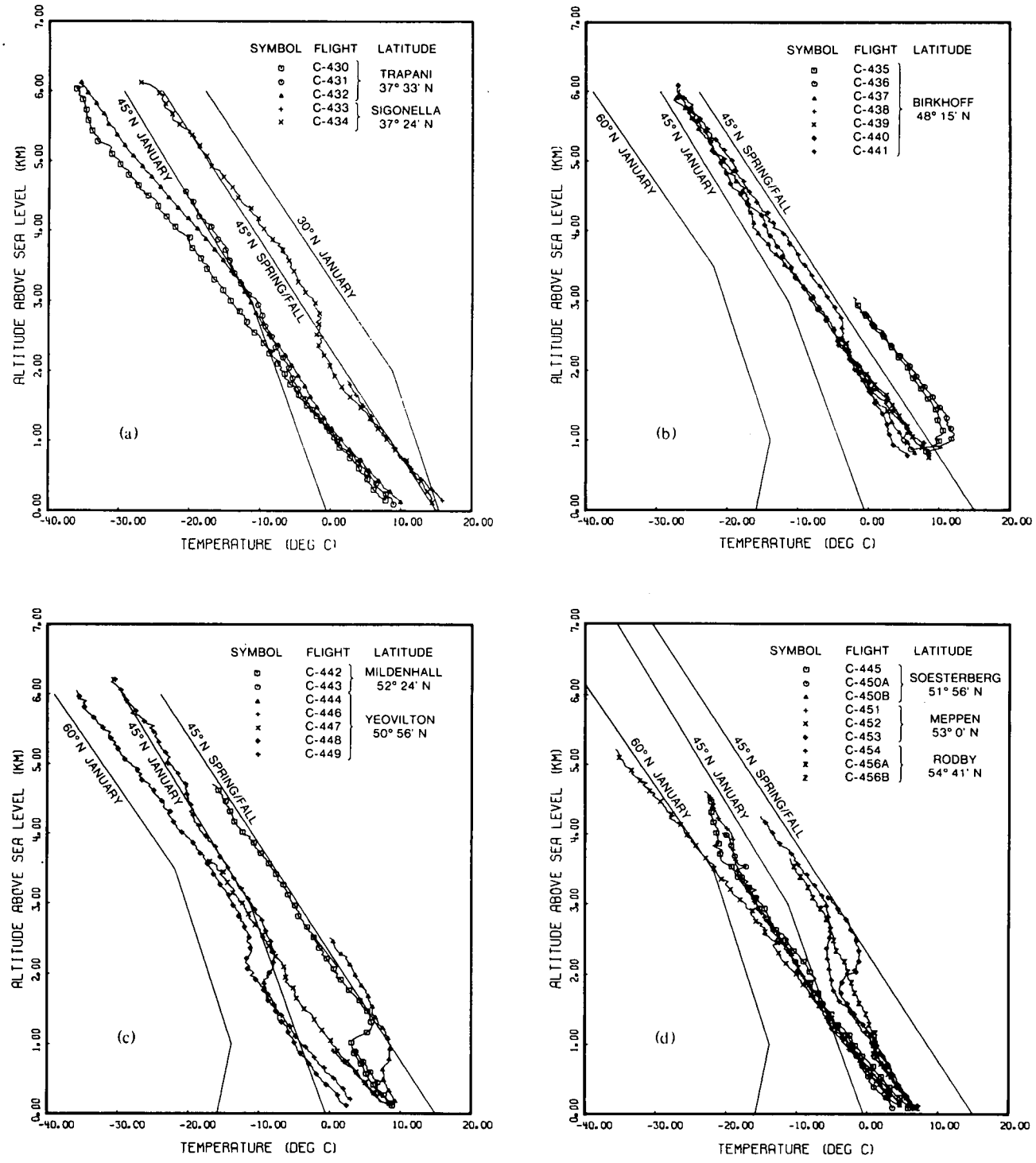

Fig. 2-1. Temperature for OPAQUE IV flights 31 January to 31 March 1978, compared to temperature from U.S. Standard Atmosphere Supplements (1966). (AFGL-TR-79-0159).

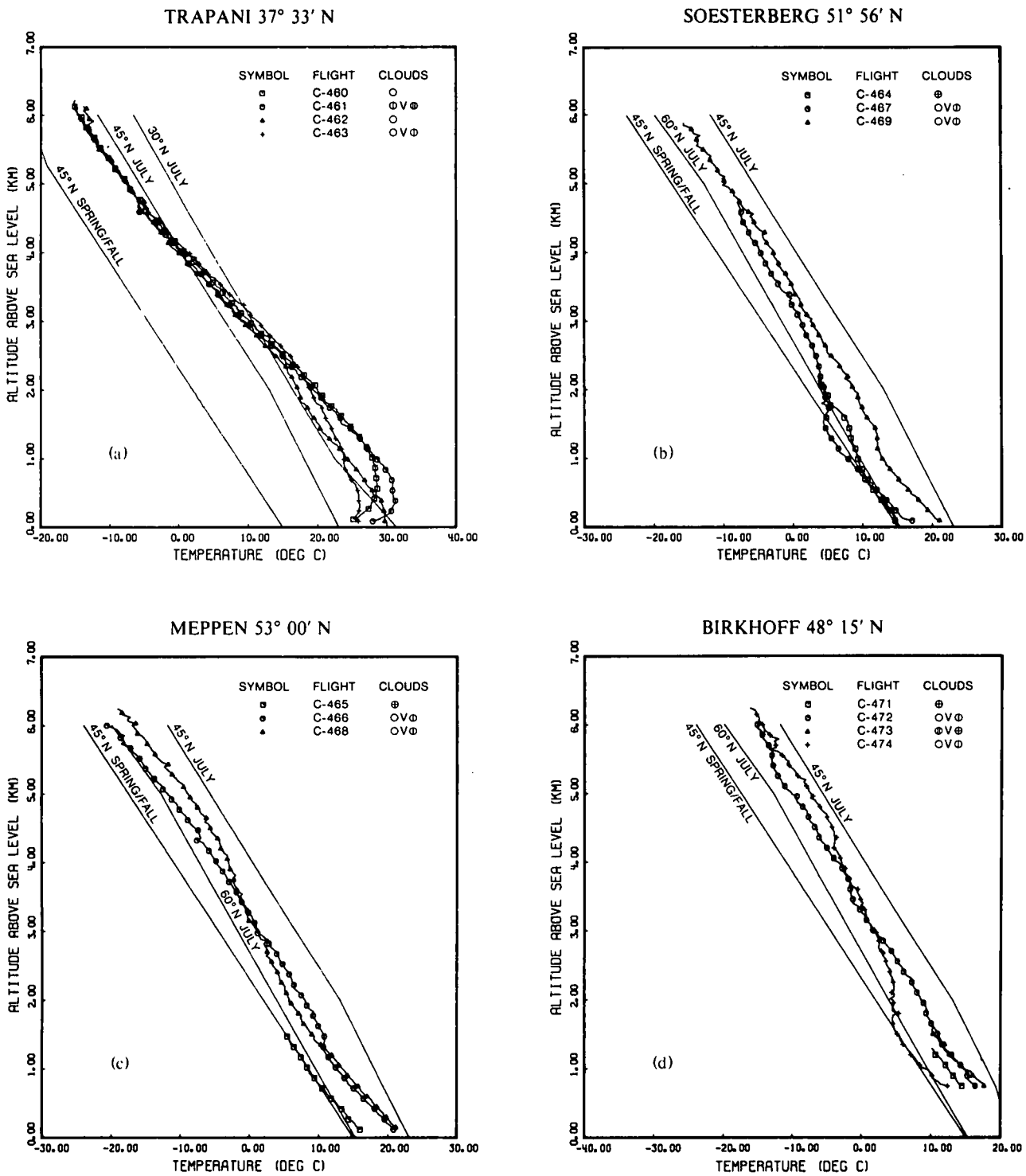

Fig. 2-2. Temperature for OPAQUE V flights 2 August to 26 September 1978, compared to temperature from U.S. Standard Atmosphere Supplements (1966). (AFGL-TR-80-0207).

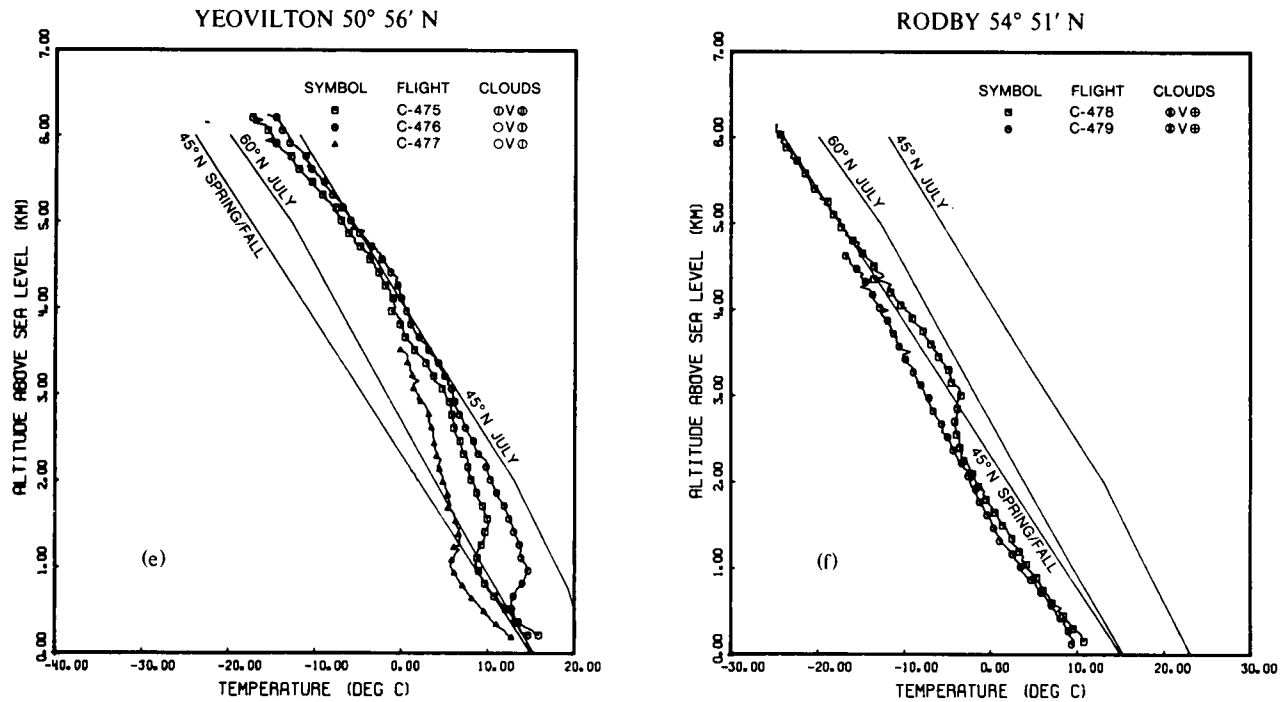

Fig. 2-2. (con't.) Temperature for OPAQUE V flights 2 August to 26 September 1978, compared to temperature from U.S. Standard Atmosphere Supplements (1966). (AFGL-TR-80-0207).

semi-square wave biasing voltage was imposed, during some flights, upon the data signal. This distortion of the profile data is of such a nature that the erroneous values are those representing the smaller value of scattering coefficient. These distortions appear to affect only the flights in Sicily and no determination of their cause has been completely established. Users should be aware of these circumstances during their evaluation of the suitability of these date for their specific application.

Users should also be advised that the potential stray light error that was discussed in each of the earlier reports listed in Table 1.2 has not been corrected in the data displays of Figs. 2-3 and 2-4, except for the Trapani data shown in Fig. 2-3a. For a complete discussion of this circumstance the reader is referred to Johnson and Gordon (1979).

Several general characteristics of the profiles illustrated in Figs. 2-3 and 2-4, briefly alluded to in the parent reports, are repeated here. In both the Winter and Summer data sets, the Trapani profiles are clearly different from their companion profiles measured in northern Europe. In the Winter set, the Trapani profiles, though noisy, show significantly less low altitude structure than any of the other sets, and have a complete lack of any abrupt haze top. Similarly the summer Trapani profiles show little structure and additionally maintain relatively high scattering coefficient values throughout the entire 6 km altitude band.

It appears, in general, that there is substantially more structural irregularity in the scattering coefficient profiles during the Winter set than during the Summer. This is particularly true for the northern European stations, Soesterberg, Meppen, and Rodby as illustrated in Fig. 2-3d and Figs. 2-4b, d and f.

A necessary but unfortunate artifact of the profile data discussed in the preceding paragraphs is that the measurements all terminate at some significant altitude above ground level. This being a necessary condition imposed by the safety of flight regulations which apply to all civil air space, and an unfortunate experimental constraint in view of the extreme sensitivity of slant path contrast transmittances to variations in the near surface haze conditions. The data contained in two of the reports listed in Table 2.3 (AFGL-TR-81-0154 and -0237), were provided to reduce the uncertainties in our knowledge of the scattering coefficients near-surface profile.

Several samples of these near surface profiles are presented as Figs. 2-5 and 2-6. There are, in general, only occasional variations of any substance within these low altitude profiles. In this sample of 54 low altitude daytime profiles, acquired in clear air away from clouds (*i.e.* under VFR conditions), 47 (87%) are represented by nearly constant scattering coefficients as a function of changing altitude. These stable conditions are clearly illustrated in Figs. 2-5a and 2-6b. Four of the seven anomalous profiles

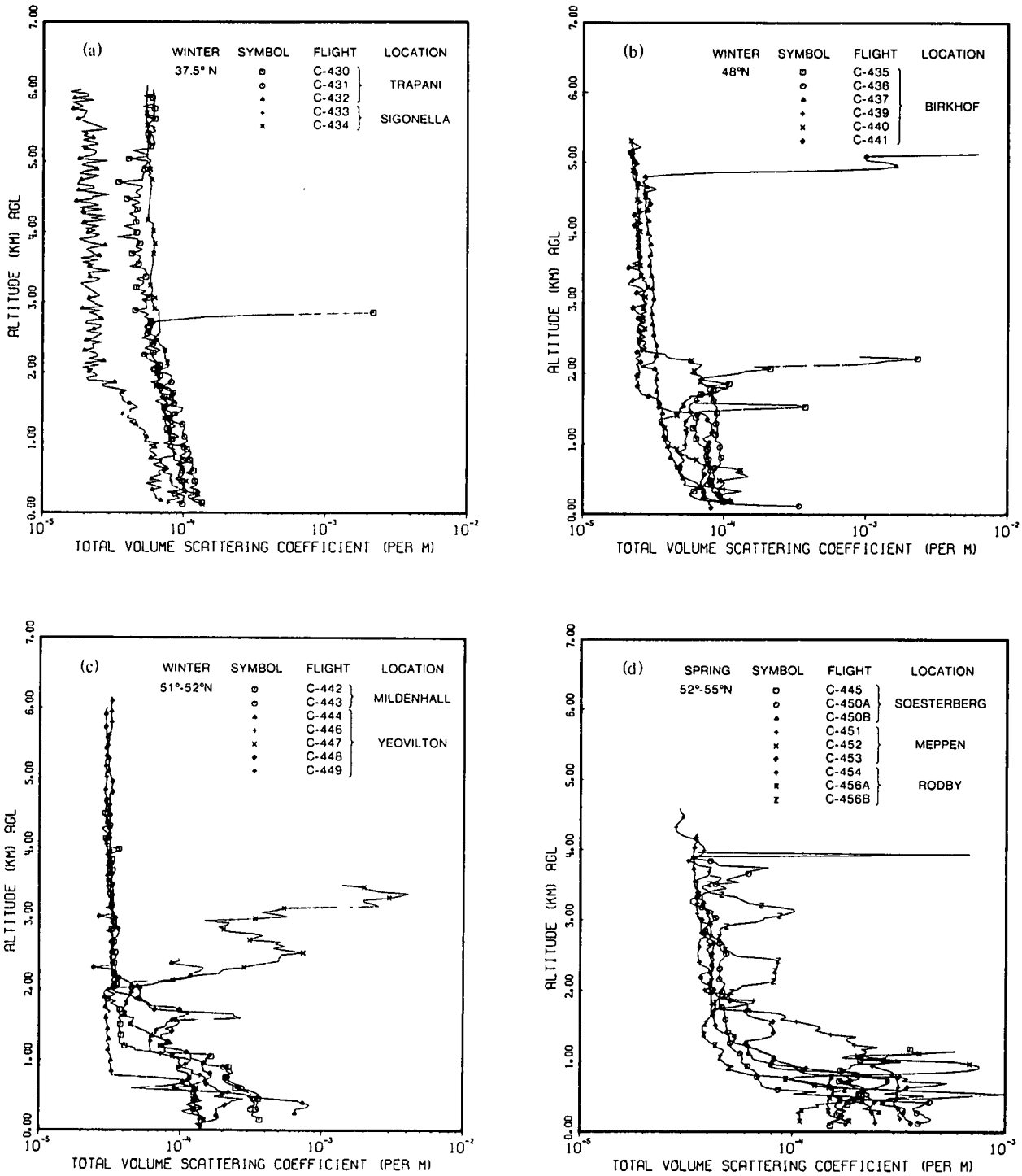

Fig. 2-3. Total volume scattering coefficient for filter 4 pseudo-photopic for OPAQUE IV flights 31 January through 31 March 1978 (AFGL-TR-79-0159).

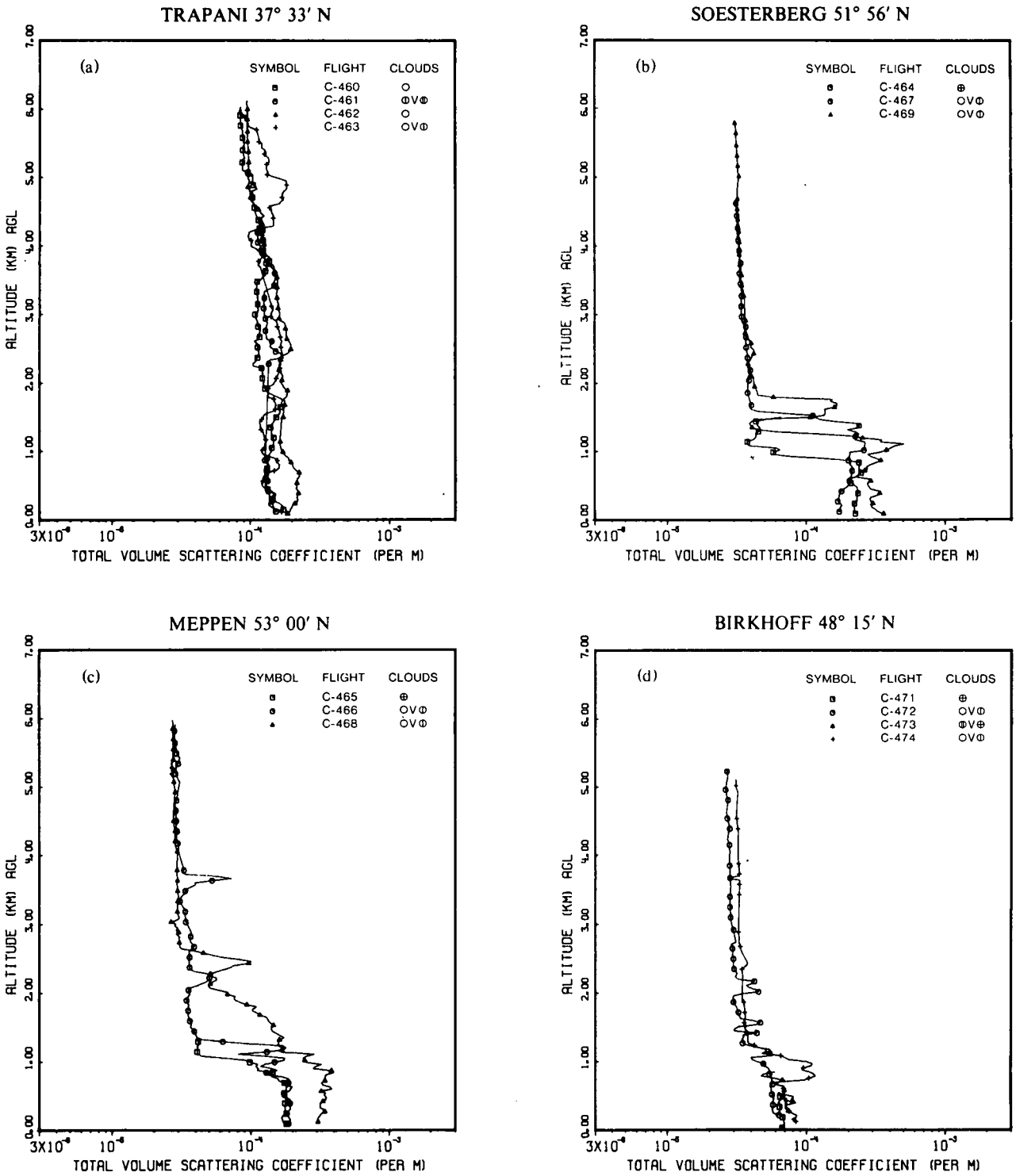

Fig. 2-4. Airborne nephelometer pseudo-photopic data for OPAQUE V flights from 2 August to 26 September 1978 (AFGL-TR-80-0207).

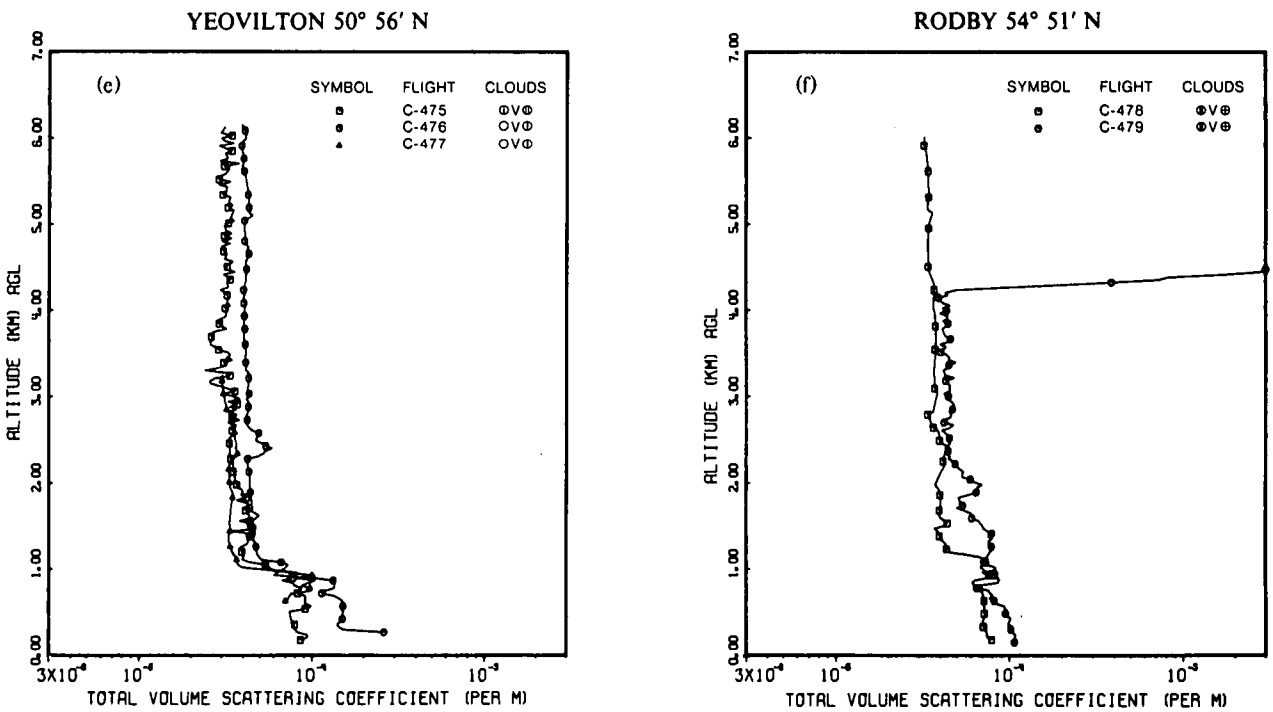

Fig. 2-4. (con't.) Airborne nephelometer pseudo-photopic data for OPAQUE V flights from 2 August to 26 September 1978 (AFGL-TR-80-0207).

that were measured are contained in the illustrations of Fig. 2-5b and 2-6a. As noted in the earlier reports, the identification of the conditions resulting in the seven profiles showing variations within their vertical structure will require additional analysis. In this regard, a supplementary set of precision local meteorological observations including local trajectories would be beneficial.

Sky and Terrain Radiances

As noted in Table 2.3, there were two general classes of radiometric data collected during a typical airborne measurement sequence. The first being primarily scattering coefficient profile data as illustrated in the immediately preceding figures and comments, and the second being measurements of sky and terrain radiances at selected assorted altitudes. This second complementary data set, introduced in Johnson (1981), includes angularly precise spectral measurements of the 4π radiance field surrounding the aircraft at several different altitudes throughout the zero to six kilometer altitude regime.

These radiance data enable one to characterize a broad variety of the environmental conditions extant during the flight episode and thus lead directly to the development of operationally useful predictive models. The radiance data, in conjunction with their companion scattering coefficient data, are readily applicable to the determination of slant path contrast transmittances, atmospheric optical depths, aerosol directional scattering characteristics, flux divergences and their attendant determinations of turbid atmosphere single scattering albedos.

For this brief overview, only a small sample of the nearly 500 radiance arrays that have been processed have been selected for presentation here. As with the preceding temperature and scattering coefficient data, these sky and terrain radiance displays have been abstracted from a previously published parent reports, Johnson (1981), and Johnson and Hering (1981).

The data displays presented in Figs. 2-8 through 2-11 are in the Composite Sky-Terrain Radiance format used in several earlier reports. In these composite plots, the radiance variations throughout the sun-zenith plane, in both the up-sun and down-sun directions, are plotted as a single curve, and labeled "PHI = 0 & -180". Similarly, the data in the cross-sun plane are plotted continuously and labeled "PHI = 90 & -270". In all cases a zenith view angle of 0° represents the point in the sky directly overhead, and a zenith view angle of 180° represents the point on the underlying terrain directly below. The negative signs associated with the angular indices are an artifact of the computer sorting technique, and should not be rigorously interpreted.

MILDENHALL, ENGLAND WINTER 1978

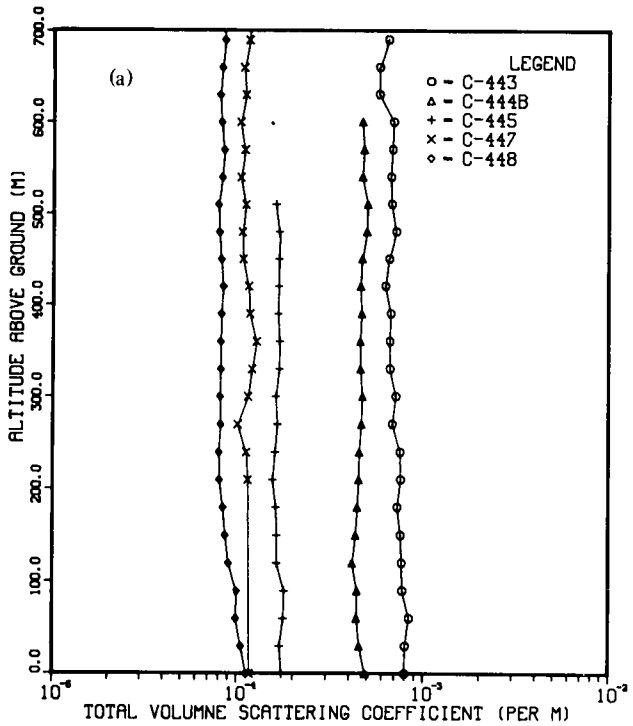

Altitude (m) AGL	Total Volume Scattering Coefficient (m^{-1}) C443	C444B	C445	C447	C448
810.				1.116E-04	
780.				1.232E-04	
750.				1.243E-04	
720.				1.164E-04	8.401E-05
690.	6.405E-04			1.148E-04	8.485E-05
660.	5.718E-04			1.077E-04	8.201E-05
630.	5.728E-04			1.101E-04	7.988E-05
600.	6.838E-04	4.661E-04		1.033E-04	8.163E-05
570.	6.734E-04	4.765E-04		1.089E-04	8.450E-05
540.	6.635E-04	4.678E-04		1.038E-04	8.237E-05
510.	6.709E-04	4.995E-04	1.605E-04	1.107E-04	7.880E-05
480.	7.103E-04	4.952E-04	1.673E-04	1.062E-04	8.000E-05
450.	6.521E-04	4.683E-04	1.670E-04	1.075E-04	8.206E-05
420.	6.227E-04	4.598E-04	1.665E-04	1.153E-04	8.409E-05
390.	6.657E-04	4.668E-04	1.654E-04	1.171E-04	8.228E-05
360.	6.597E-04	4.587E-04	1.687E-04	1.274E-04	8.181E-05
330.	6.615E-04	4.592E-04	1.683E-04	1.206E-04	8.176E-05
300.	7.122E-04	4.721E-04	1.617E-04	1.147E-04	8.107E-05
270.	6.817E-04	4.660E-04	1.648E-04	1.012E-04	8.169E-05
240.	7.524E-04	4.539E-04	1.602E-04	1.124E-04	8.019E-05
210.	7.595E-04	4.525E-04	1.554E-04	1.149E-04	8.053E-05
180.	7.260E-04	4.440E-04	1.623E-04	1.152E-04	8.434E-05
150.	7.584E-04	4.357E-04	1.642E-04	1.155E-04	8.680E-05
120.	7.685E-04	4.165E-04	1.642E-04	1.158E-04	9.077E-05
90.	7.755E-04	4.424E-04	1.798E-04	1.161E-04	1.000E-04
60.	8.448E-04	4.406E-04	1.777E-04	1.164E-04	9.925E-05
30.	8.040E-04	4.554E-04	1.697E-04	1.167E-04	1.057E-04
0.	7.992E-04	4.898E-04	1.745E-04	1.170E-04	1.128E-04
Visibility (km)	>11.2	>11.2	>11.2	5	MSG
Visual Range (km)	4	6	17		17
Illumination (lux)	16500	10800	35600	21900	20400
Landing Time (GMT)	1557	1624	1326	1504	1449

MEMMINGEN, GERMANY WINTER 1978

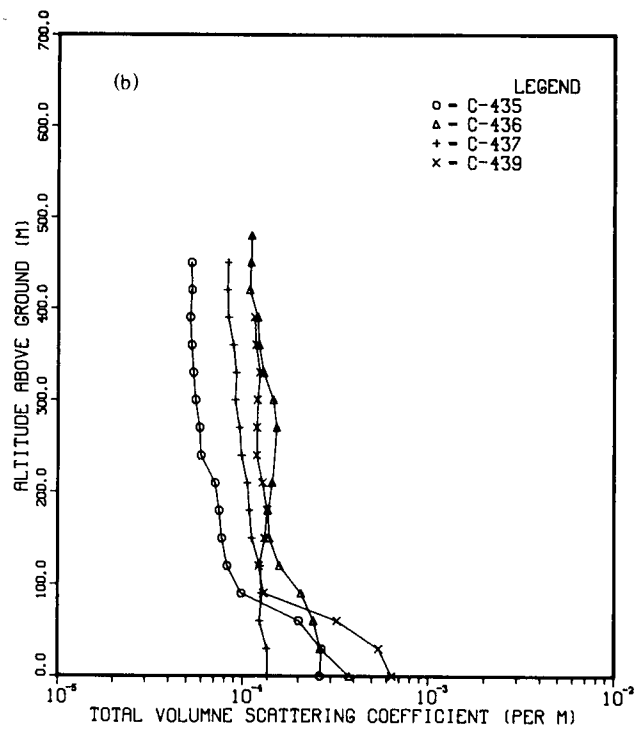

Altitude (m) AGL	Total Volume Scattering Coefficient (m^{-1}) C435	C436	C437	C439
480		1.110E-04		
450	5.273E-05	1.100E-04	8.281E-05	
420	5.295E-05	1.083E-04	8.227E-05	
390	5.188E-05	1.197E-04	8.321E-05	1.147E-04
360	5.279E-05	1.215E-04	8.863E-05	1.169E-04
330.	5.408E-05	1.287E-04	9.167E-05	1.227E-04
300	5.566E-05	1.454E-04	9.077E-05	1.192E-04
270	5.863E-05	1.516E-04	9.578E-05	1.184E-04
240	5.949E-05	1.476E-04	9.842E-05	1.186E-04
210.	7.090E-05	1.436E-04	1.056E-04	1.275E-04
180.	7.465E-05	1.364E-04	1.081E-04	1.350E-04
150.	7.721E-05	1.390E-04	1.116E-04	1.308E-04
120	8.243E-05	1.582E-04	1.239E-04	1.218E-04
90	9.837E-05	2.064E-04	1.261E-04	1.295E-04
60.	2.006E-04	2.411E-04	1.232E-04	3.231E-04
30	2.671E-04	2.633E-04	1.351E-04	5.433E-04
0	2.605E-04	3.775E-04	1.356E-04	6.409E-04
Visibility (km)	>11.2	>11.2	>11.2	5
Visual Range (km)	11	8	22	5
Illumination (lux)	55100	14000	26900	2100
Landing Time (GMT)	1043	1524	1358	1456

Fig. 2-5. Low altitude scattering coefficients, Winter, 1978.

As an aid to the interpretation of the radiance distributions illustrated in Figs. 2-8 through 2-11, a pictorial representation of the measurement field is shown in Fig. 2-7. This artist's conception of the 4π radiance field which surrounds the aircraft is annotated with the angular notations and terminologies used in the data displays and discussions which follow.

WUNSTORF, GERMANY FALL 1976

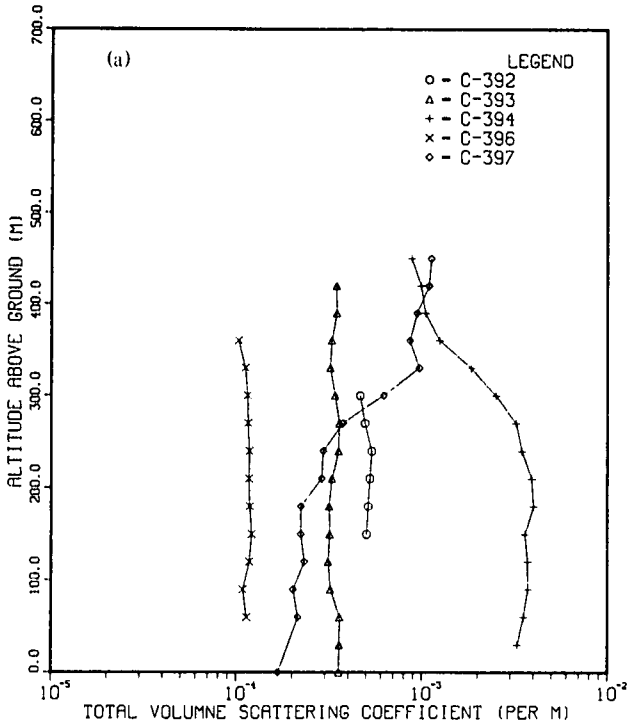

Altitude (m) AGL	Total Volume Scattering Coefficient (m^{-1}) C392	C393	C394	C396	C397
450			8.782E-04		1.120E-03
420		3.443E-04	9.862E-04		1.088E-03
390		3.459E-04	1.042E-03		9.347E-04
360		3.258E-04	1.244E-03	1.025E-04	8.595E-04
330		3.199E-04	1.847E-03	1.114E-04	9.665E-04
300	4.639E-04	3.394E-04	2.509E-03	1.147E-04	6.203E-04
270	4.927E-04	3.583E-04	3.225E-03	1.154E-04	3.734E-04
240	5.351E-04	3.545E-04	3.472E-03	1.175E-04	2.937E-04
210	5.230E-04	3.270E-04	3.914E-03	1.169E-04	2.877E-04
180	5.131E-04	3.162E-04	4.001E-03	1.182E-04	2.226E-04
150	5.026E-04	3.193E-04	3.598E-03	1.210E-04	2.224E-04
120		3.128E-04	3.716E-03	1.176E-04	2.325E-04
90		3.216E-04	3.721E-03	1.083E-04	2.023E-04
60		3.597E-04	3.524E-03	1.135E-04	2.147E-04
30		3.585E-04	3.260E-03	1.135E-04	1.911E-04
0		3.555E-04	3.260E-03	1.135E-04	1.674E-04
Reported Visibility (km)	MSG	≥11.2	1.7	≥11.2	≥11.2
Visual Range (km)	6.0	8.3	9.1	26.5	18.0
Illumination (lux)	23500	32000	3100	11000	2300
Landing Time (GMT)	1323	1150	1358	1105	1410

WUNSTORF, GERMANY SUMMER 1976

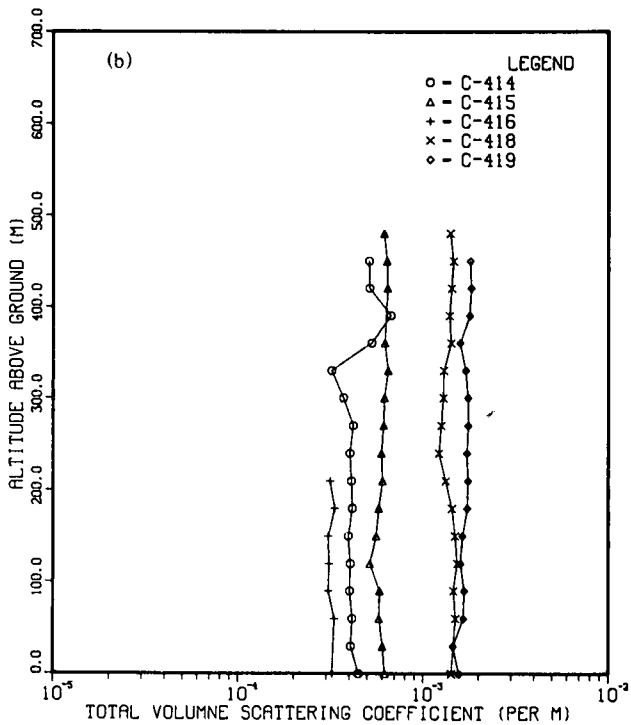

Altitude (m) AGL	Total Volume Scattering Coefficient (m^{-1}) C414	C415	C416	C418	C419
480		6.105E-04		1.397E-03	
450	5.065E-04	6.333E-04		1.452E-03	1.794E-03
420	5.105E-04	6.380E-04		1.421E-03	1.816E-03
390	6.640E-04	6.275E-04		1.385E-03	1.777E-03
360	5.250E-04	6.170E-04		1.414E-03	1.581E-03
330	3.186E-04	6.426E-04		1.289E-03	1.695E-03
300	3.696E-04	6.122E-04		1.281E-03	1.743E-03
270	4.167E-04	6.080E-04		1.247E-03	1.747E-03
240	3.999E-04	5.928E-04		1.213E-03	1.716E-03
210	4.082E-04	6.001E-04	3.139E-04	1.321E-03	1.744E-03
180	4.136E-04	5.736E-04	3.321E-04	1.429E-03	1.729E-03
150	3.930E-04	5.566E-04	3.072E-04	1.486E-03	1.632E-03
120	4.037E-04	5.143E-04	3.095E-04	1.527E-03	1.590E-03
90	4.004E-04	5.798E-04	3.074E-04	1.456E-03	1.668E-03
60	4.130E-04	5.771E-04	3.308E-04	1.497E-03	1.651E-03
30	4.066E-04	6.033E-04	3.266E-04	1.460E-03	1.449E-03
0	4.480E-04	6.196E-04	3.223E-04	1.422E-03	1.569E-03
Reported Visibility (km)	≥11.2	≥11.2	≥11.2	6.0	4.9
Visual Range (km)	6.7	4.8	9.4	2.1	1.9
Illumination (lux)	49300	58800	34200	53600	22000
Landing Time (GMT)	1159	1249	1536	1046	1647

Fig. 2-6. Low altitude scattering coefficients, Fall and Summer, 1976.

Six radiance plots representing portions of three different data flights have been abstracted from the parent reports referenced above and reproduced as Fig. 2-8. These six displays are the standard computer output for data of this type and thus present one data point at every five degree increment in zenith angle. Radiances measured in the near-sun regions which go off-scale, as in Fig. 2-8e, have been automatically truncated at the maximum plot boundary *i.e.* $10^5\ w\Omega^{-1}m^{-2}\mu m^{-1}$, and thus should not be interpreted as reliable measurements. Neither have these data been corrected for the near-sun stray light errors discussed in Johnson (1981). Therefore radiance measurements made within ±25° from the solar disc will contain a stray light component which is dependent upon the aerosol loading of the atmosphere above the measurement altitude. As noted in Johnson (1981), the near-sun stray light effects can range from zero, as in the full overcast case of Fig. 2-8a, to as much as a factor of 25 in cases

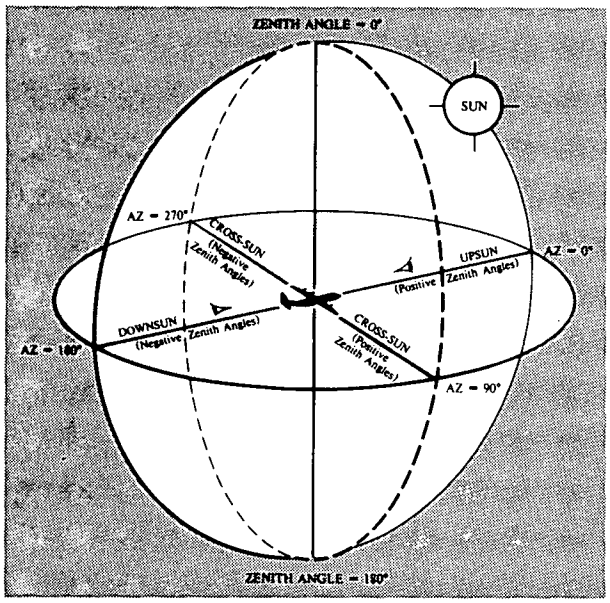

Fig. 2-7. Sky and terrain coordinate system.

similar to the clear high altitude situations shown in Fig. 2-8d.

It is clear however, that even with the above caveats, there are several readily distinguishable characteristics inherent in the data plots of Fig. 2-8.

The data in Fig. 2-8a represents one of the most symmetric radiance distributions retrieved from the OPAQUE series. This example, one of eight in the parent report, illustrates radiances in all four cardinal azimuths from the sun showing nearly identical gradients as a function of zenith angle with very little sky structure. One should note the relatively large radiance difference between the overhead sky and the underlying ocean surface, and contrast this difference with the data in Fig. 2-8b. In Fig. 2-8b the data represent a similar overcast sky condition over a completely different underlying terrain. The relatively high reflectance of the snow covered plateau underlying the Birkhof flight track has produced the most directionally constant radiance levels retrieved from the OPAQUE series.

The characteristics of radiance uniformity and symmetry illustrated by the data from flights C-422 and C-435 are relatively unique and can be considered to represent one extreme in the overall spectrum of sky and terrain radiance distributions.

Just as the fully overcast conditions illustrated in Figs. 2-8a&b illustrate one end of the meteorological spectrum, the clear sky conditions of flight C-379, Figs. 2-8c&d, represent the other. These plots, two of the fourteen which appear in the parent report, represent clear sky conditions whose radiance patterns are typically well behaved and tell a consistent story with respect to upper and lower hemisphere characteristics, both as a function of observational wavelength and altitude. The bright horizons and highly asymmetric up-sun and down-sun radiance levels are consistent and clearly discernible. For this over water track, the uniformity of the down-sun and cross-sun sea surface radiances is well illustrated as is the obvious glitter pattern which appears as a broad high radiance peak in the up-sun data of Fig. 2-8c and narrows as the flight altitude increases to 6 km in Fig. 2-8d. The relatively high radiance of the nearby shoreline gradually appears in the down-sun lower hemisphere measurements as the altitude of observation increases, also shown clearly in Fig. 2-8d.

Flight C-468 provided fifteen data plots, two of which are shown here as Figs. 2-8e&f. These data were measured on a nominally clear day that was, however, dominated by high, thin cirrus. The subtlety and difficulty of precisely identifying cirrus effects are illustrated by comparing plots c&d with plots e&f. In this example, both of the low altitude plots c&e show very similar cross-sun and down-sun patterns although the Rodby data (c) was taken under clear sky and the Meppen (e) under thin cirrus. In the high altitude pair, the Rodby data (d) show the irregular cross-sun and down-sun characteristics of the low altitude data, apparently cirrus contaminated, while the Meppen plots (f) show the regular and well matched characteristic normally anticipated from high altitude clear sky measurements.

Several additional comparisons of sky and terrain radiance characteristics are illustrated in Figs. 2-9, 2-10 and 2-11 which have been abstracted from Johnson and Hering (1981). In these composite plots, several flight sequences have been combined on a single display in order to more clearly illustrate the characteristic of interest. The three characteristics illustrated in this particular series are radiance variations as a function of spectral passband, variations as a function of altitude and variations as a function of cloud cover.

Comparative measurements of the sky and terrain radiance fields as a function of wavelength for flight C-466 are shown in Fig. 2-9. Since the coefficient for Rayleigh (*i.e.* molecular) scattering varies very nearly as the -4th power of the wavelength, λ, and the Mie (*i.e.* aerosol) scattering coefficient varies roughly in the range $\lambda^{-0.5}$ to $\lambda^{-1.5}$, the radiance field has a strong spectral dependence. This dependence is illustrated clearly in Figs. 2-9a&b by the very pronounced decrease in sky radiance with increasing wavelength through this visible spectrum interval. Note also that the spectral variations of the measured apparent terrain radiance, while heavily cluttered by the influence of small scale fluctuations in surface reflectivity, still illustrate significant spectral separations. A prominent feature in this regard is the relatively large apparent terrain radiance measured in the 750nm spectral band. These high radiances result from the characteristically large surface reflectance for rural farm and wooded areas in the near infrared portions of the spectrum.

The data from flight C-466 also can be used to illustrate the variation in sky and terrain radiances as a function of altitude. These altitude dependent characteristics are presented in Fig. 2-10.

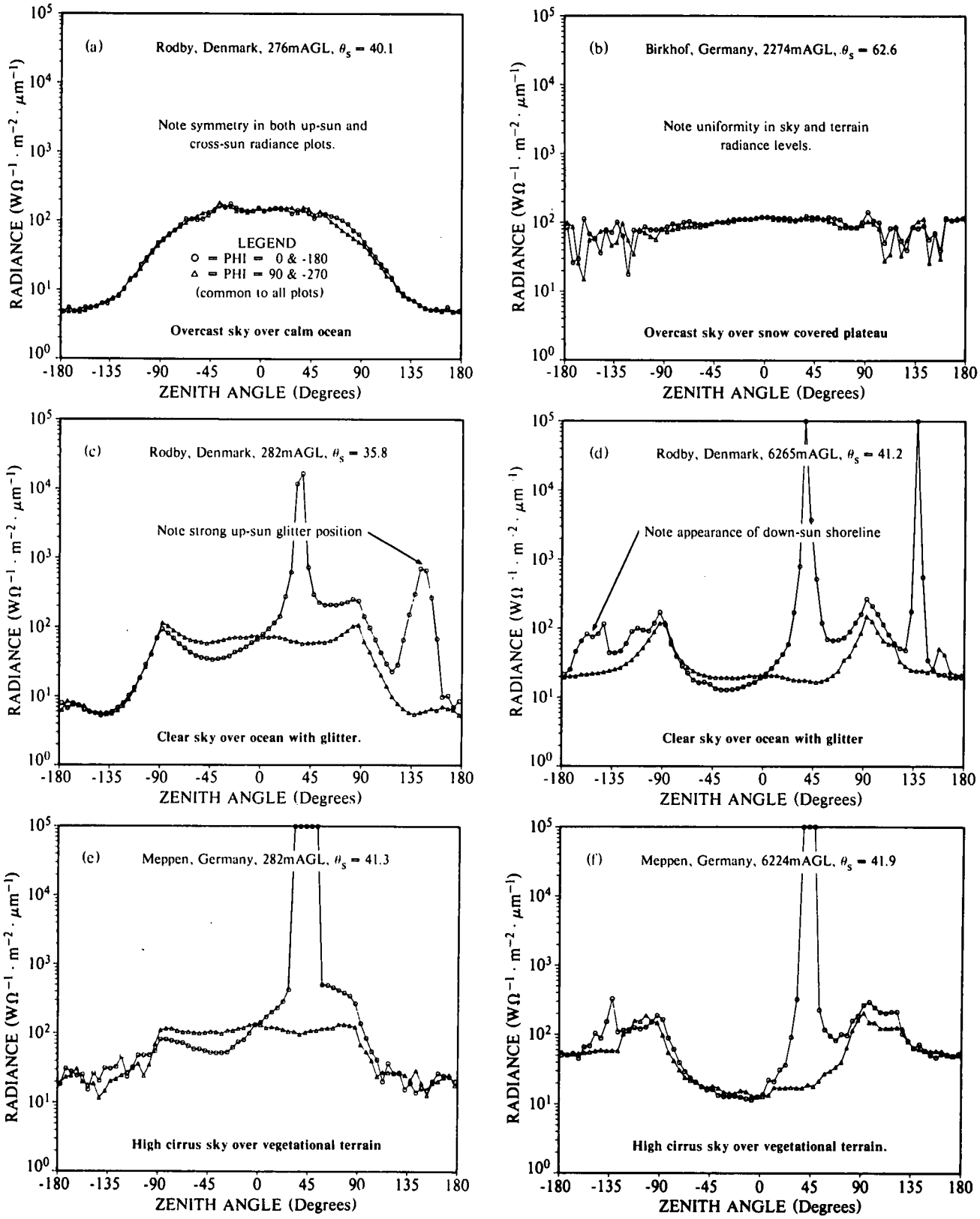

Fig. 2-8. Selected sky and terrain radiance plots from flights C-379, C-422, C-435 and C-468. Plots a, c, and e are low altitude (~ 27m AGL). Plots b, d, and f are high altitude (> 2500 m AGL).

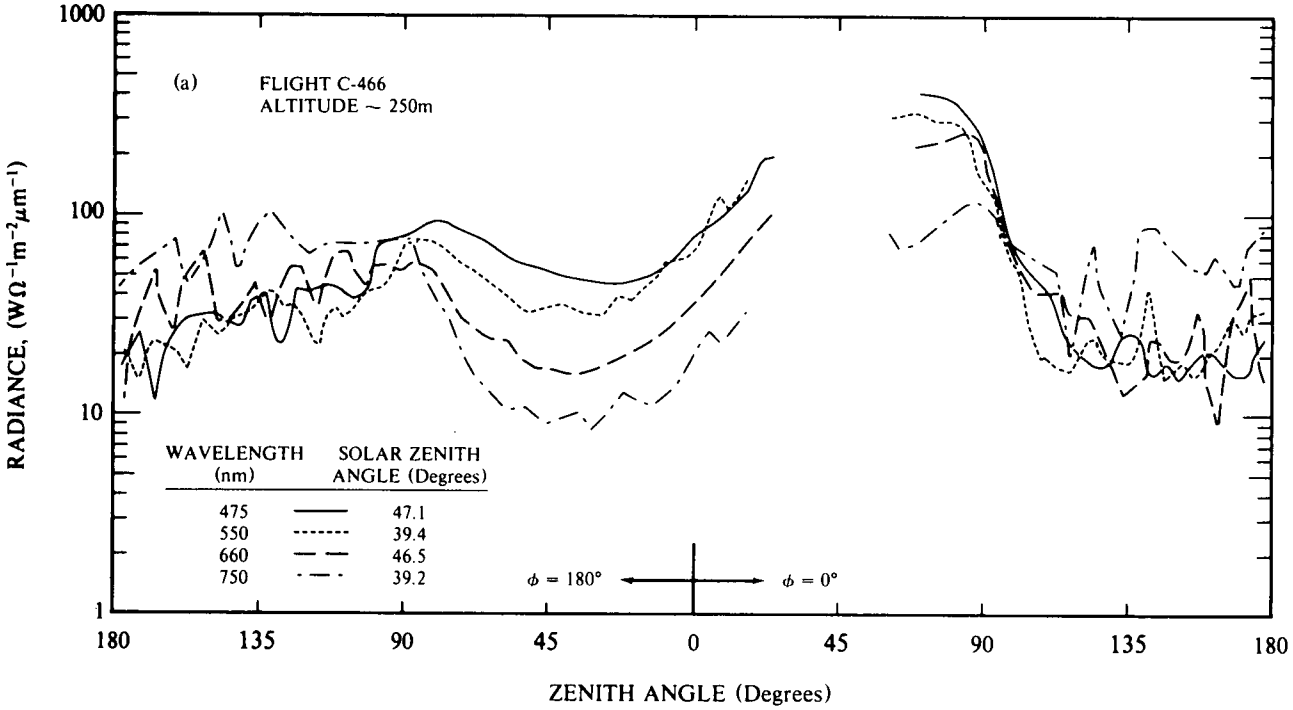

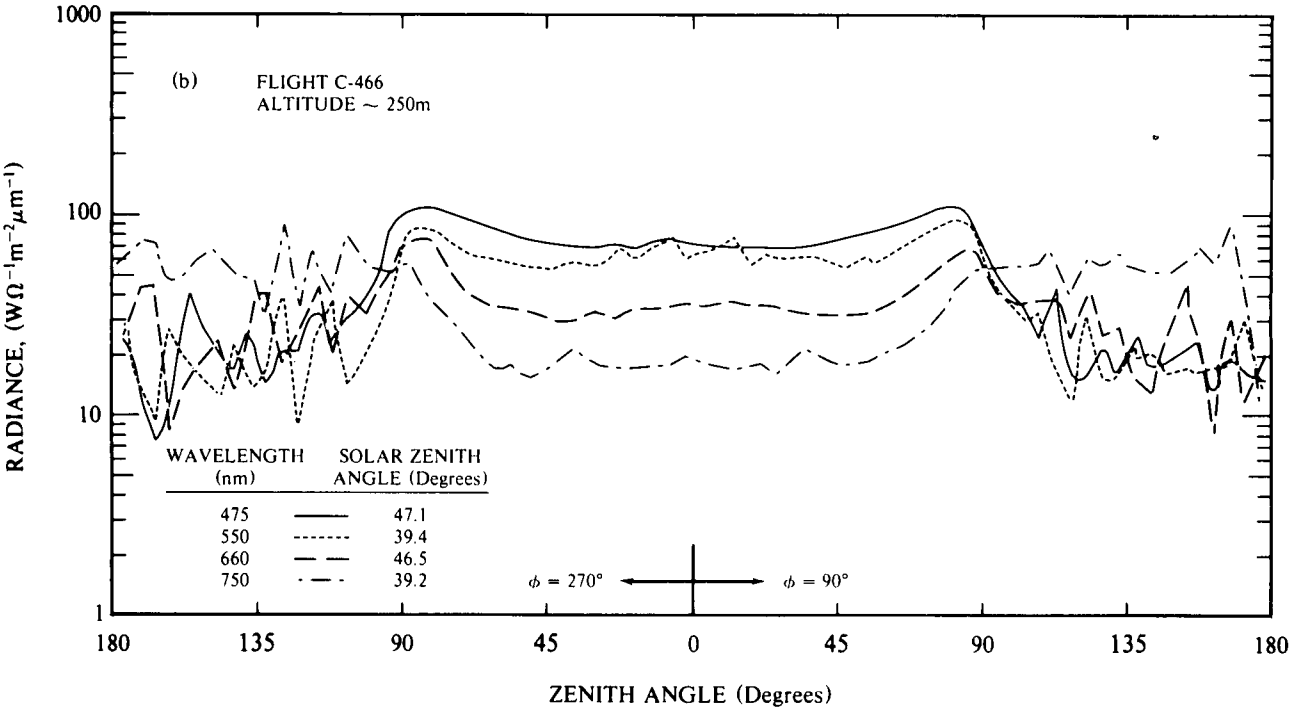

Fig. 2-9. Sky and terrain radiance variations *vs* wavelength.

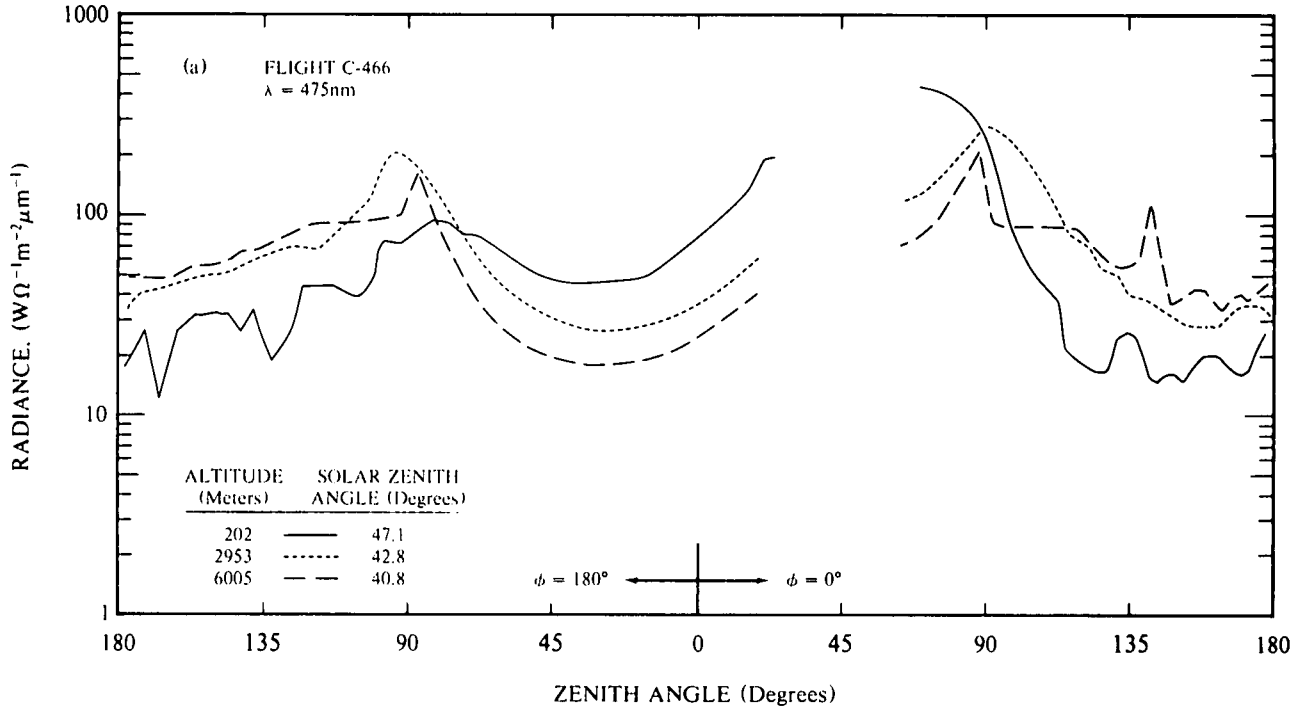

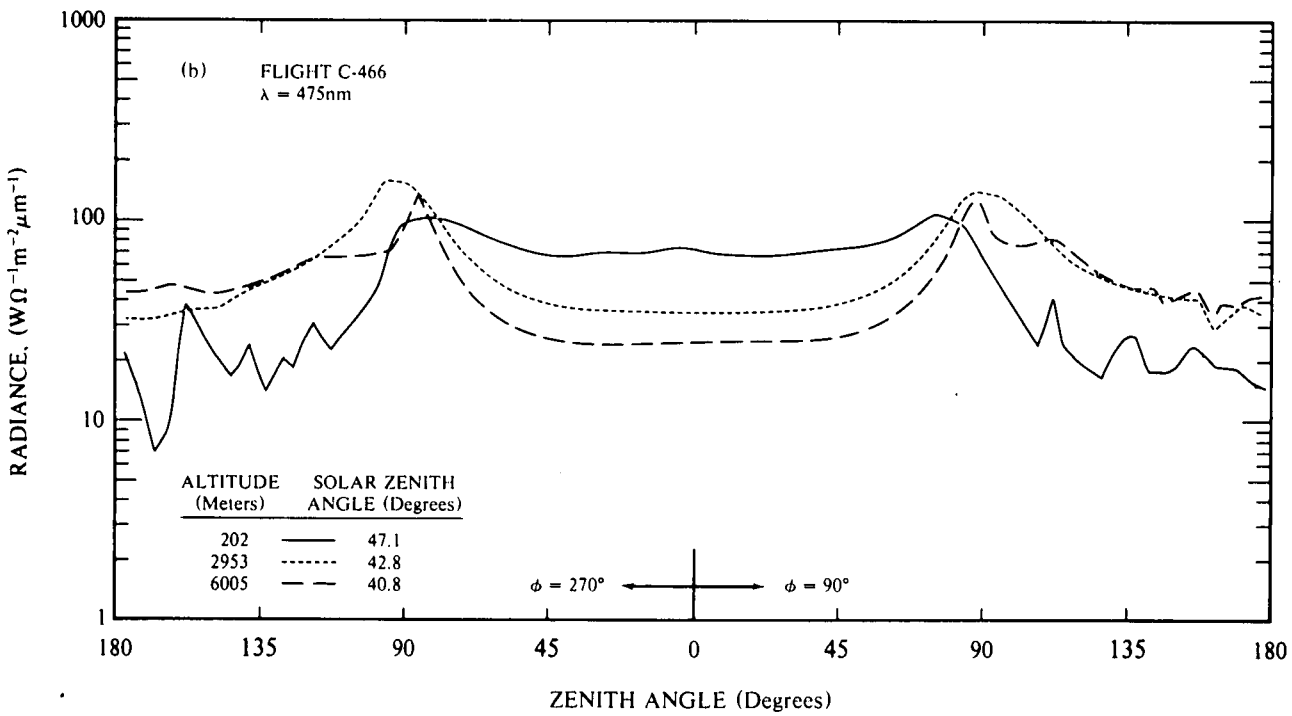

Fig. 2-10. Sky and terrain radiance variations *vs* altitude.

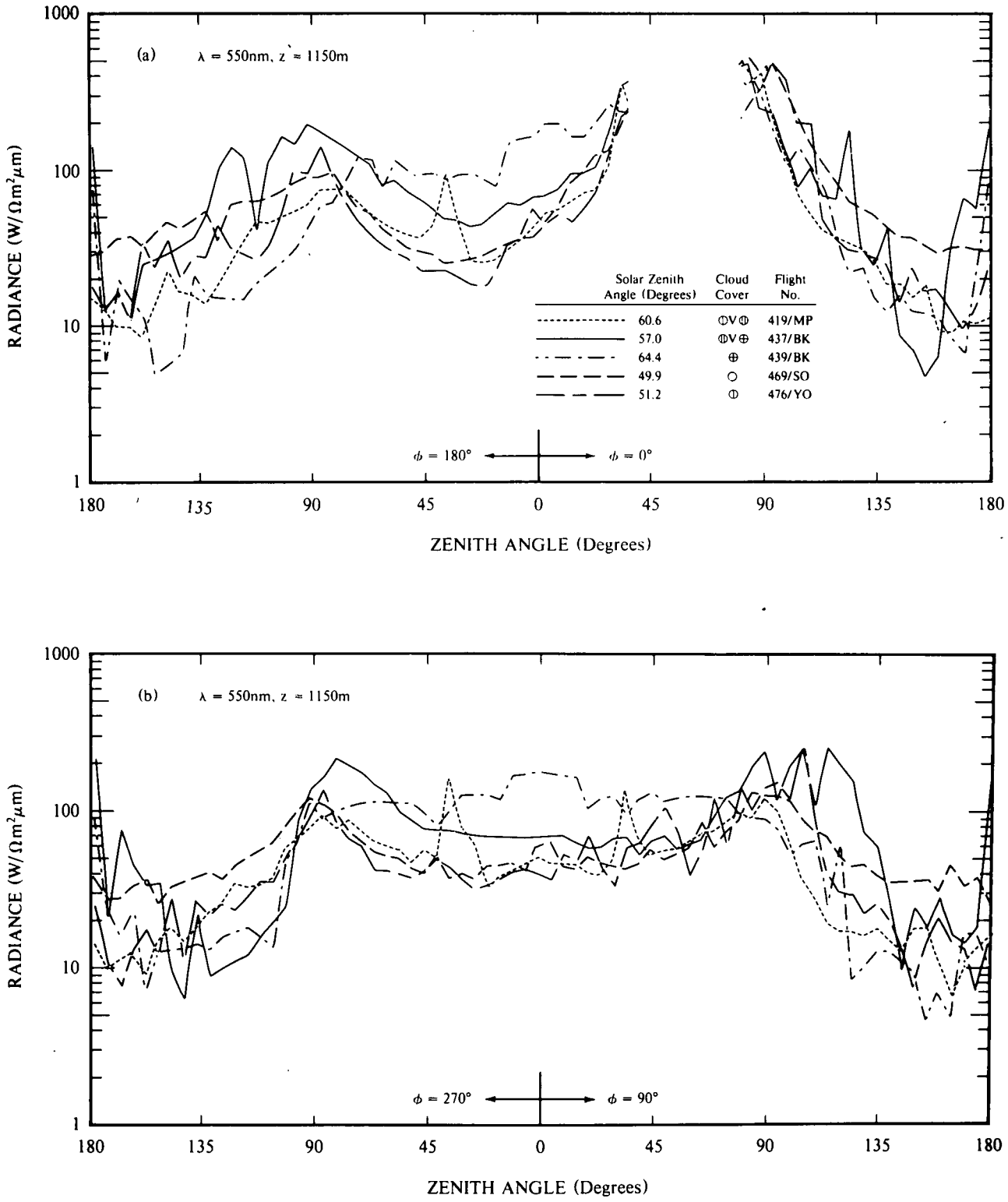

Fig. 2-11. Sky and terrain radiance variations *vs* cloud cover.

The influence of atmospheric path radiance upon the apparent radiance of both the sky and terrain is clearly demonstrated in both Figs. 2-10a&b. At the wavelength chosen for illustration, λ = 475nm, as well as for those not shown here but included in the parent report Johnson and Hering (1981), the systematic decrease in apparent sky radiance as the altitude of measurement increases is obvious, as is the corollary increase in apparent terrain radiance. One should note the tendency for the percent change in sky radiance between specific altitude levels to be much the same over a wide range of viewing angles as is discussed from an analytic point of view in the parent report.

To illustrate the variation of sky and terrain radiances as a function of variable cloud cover, a composite plot containing data from five separate flights is presented as Fig. 2-11. All of the measurements selected for this comparison were made in the pseudo-photopic passband *i.e.* $\bar{\lambda}$ = 550nm, see Fig. 1-2. These five flight episodes represent a broad variety of conditions, ranging from clear, O, to overcast, ⊕, as measured from an intermediate altitude of approximately 1150 m AGL.

One notes that the measured sky and terrain radiances for these cloudy cases tend to fluctuate both above and below the radiance distribution for the clear sky, see Johnson and Hering (1981), depending upon the scattering and reflectance properties of the clouds, haze and terrain. The measured cloudy sky radiance is found to be a factor of two or more larger in some instances, but in general remains within about ±50 percent of the clear sky radiance for corresponding paths of sight. It is appropriate to keep in mind the significant differences in terrain characteristics for the flights shown in Fig. 2-11a&b. The Meppen (MP), Soesterberg (SO), and Yeovilton (YO) flights were made over cultivated farmland, and the two Birkhof flights were made over a snow covered, wooded plateau. The influence of these different terrain reflectances upon their associated path radiances can be significant and is appropriate for study using fast operational models such as that described by Hering (1981).

2.3 Data Evaluations

In the preceding sections, a variety of profile and fixed altitude radiometric measurements of total volume scattering coefficient and sky radiances have been presented as an overview of the data reductions accomplished as part one of this two part contract. Over a period of several years, as the various experimental measurements and data reduction activities progressed, there were intermittent but continuing evidences of instrumentally induced error, in one system or another, that often were persistently unyielding in identifying the source of the suspected error. In most cases adequate identification of the system malfunction was accomplished through a study of the automatic diagnostic tests applied to the data in the early stages of processing. However, there were two instances where an uncertainty in the measurements continued throughout the program. Since these uncertainties relate to the primary instrument systems and their data, *i.e.* the integrating nephelometer, and the upper hemisphere scanner, some further comment seems appropriate.

Total Volume Scattering Coefficient

As discussed in several earlier reports, among them Duntley *et al.* (1975), and Duntley *et al.* (1978), the airborne integrating nephelometer underwent a major reconfiguration shortly before the initial OPAQUE deployment in the Spring of 1976. As an outgrowth of this reconfiguration the essentially in-line flow through device, as illustrated in Fig. 3-1 of Duntley *et al.* (1975), was converted into the folded path, compact design illustrated in Fig. 3-4 of Duntley *et al.* (1978). There were several stray light problems associated with this new design which became apparent during the analysis of the resultant data, particularly with respect to the high altitude data collected well above the primary haze layer. A discussion of this problem and the development of a corrective procedure is outlined in Duntley *et al.* (1977). A similar discussion related to the data from each of the five OPAQUE deployments was included in each of the five OPAQUE data reports listed at the bottom of Table 1.2.

Continuing analysis, as referred to in Johnson and Gordon (1980), of both the total volume scattering coefficient measurements, as well as the directional scattering function measurements at scattering angles β = 30° and 150°, led to the conclusion that in most cases, the measurements of the upper altitude total volume scattering coefficients were too high. Thus, several additional procedures were employed to try and specify the character of the error and to develop a reasonable corrective procedure.

Two separate data sets were employed in the evaluation of the probable error in the total volume scattering coefficient data. The first was that containing the nephelometers contemporary measurements of directional scattering function at scattering angles, β = 30° and 150°. The second was that containing the sky radiance distributions illustrated in Fig. 2-8, which also were made simultaneously with the nephelometer sets. Two procedures were used with each set, and were essentially unanimous in their predictions, which are summarized in Table 2.4, and discussed briefly in the following paragraphs. In both cases the procedures were conducted in terms of the optical scattering ratio Q where $Q(z)$ is defined by the ratio of the total volume scattering coefficient at altitude z, to the Rayleigh (*i.e.* Molecular) volume scattering coefficient for a given spectral band at the same altitude [Hering (1981)].

Predictions Based Upon Directional Scattering Function Measurements

Comparisons of directional scattering functions measured using the Visibility Laboratory nephelometer, with those measured by Barteneva (1960) indicate a strong correlation between the two sets of measurements. This relationship has been illustrated in each of the reports

Table 2.4. Comparison of Optical Scattering Ratio Determinations for the Region 6-10 km AGL.

Data Source and Technique	Optical Scattering Ratio, $Q(z)$		
	Filter 2	Filter 4	Filter 3
Flight C-466 @ 5545m AGL			
Nephelometer $s(z)$ meas.	**4.4**	**5.2**	**6.4**
Barteneva $\beta 30/\beta 150$	1.8	2.6	3.2
Hering $\beta 30/\beta 150$	1.6	2.5	2.4
Almucantar, $\beta 55$	1.4	1.5	1.7
Sky Radiance Ratio	1.2	2.7	5.2
Flight C-468 @ 6038m AGL			
Nephelometer $s(z)$ meas.	**4.1**	**5.6**	**7.1**
Barteneva $\beta 30/\beta 150$	1.3	1.4	1.4
Hering $\beta 30/\beta 150$	1.2	1.3	1.4
Almucantar $\beta 55$	1.3	1.3	1.4
Sky Radiance Ratio	1.6	1.6	4.3

listed in Table 2.1, and is repeated here as Fig. 2-12, which has been abstracted from Johnson and Gordon (1980). Based upon these data, one may readily accept the premise that the optical scattering ratio $Q(z)$ can be predicted on the basis of measurements of the volume scattering function ratio $\mathcal{Q}(z,\beta)$. The functional relationship may be established either by using the Barteneva data whose median values are shown in Fig. 2-12, or by establishing another analytic representation such as the Henyey-Greenstein functions (Irvine, 1968) which were used by Hering (1981). Estimates of $Q(z)$ were made using each of these representations with the measured values of $\mathcal{Q}(z,\beta)$, where $\mathcal{Q}(z,\beta)$ is defined by the ratio of the total volume scattering function at altitude z and scattering angle β, to the molecular (or Rayleigh) volume scattering function at the same altitude and scattering angle, and are listed in Table 2.4.

Predictions Based Upon Sky Radiance Measurements

Proceeding from the development by Livshits and Pavlov (1970), it can be shown that aerosol optical thickness may be obtained from measurements of solar almucantar radiances. It is clear therefore, that if one were to use the high altitude *i.e.* (6 km AGL) sky radiance data as measured by the airborne scanner system described in Johnson (1981) to determine the aerosol optical thickness above, and if one makes reasonable assumptions regarding the composition of the regions above 10 km, then one

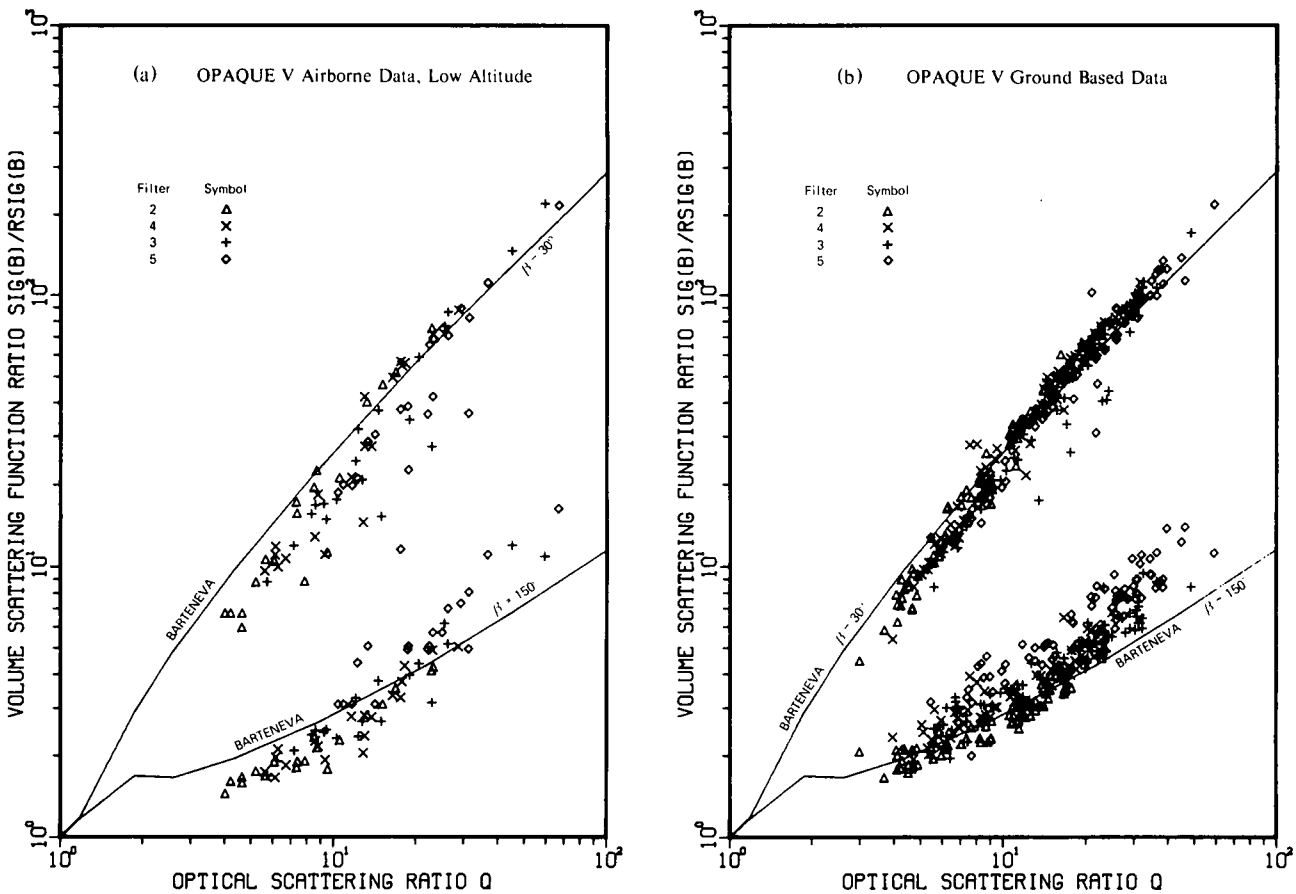

Fig. 2-12. Nephelometer directional scattering data for OPAQUE V.

might deduce an accurate estimate of the optical scattering ratio Q within the 6 km to 10 km regime. Thus, using measured solar almucantar data at $\beta 55°$ and estimates of the almucantar radiance at $\beta 125°$ where necessary, estimates of aerosol optical thickness and thence estimates for optical scattering ratio were determined for flights C-466 and C-468. The estimated values also appear in Table 2.4.

It is a straight forward procedure to determine atmospheric transmittance due to scattering from measurements of sky radiance using the radiance ratio technique of Kushpil and Petrova (1971). This technique has been used often by the Visibility Laboratory, in its computerized form, using the 2π radiance arrays produced by the airborne scanner system. These transmittances, if determined from the sky radiances measured at 6 km AGL and corrected for nominal ozone absorption can also be converted to optical depth (*i.e.* optical thickness) and used to estimate the optical scattering ratio Q much as in the preceding paragraph. This alternate technique was also used with the data from flights C-466 and C-468 resulting in the additional estimates shown in Table 2.4.

It is clear that while each of the four procedures outlined above are derived from a valid and fairly rigorous theoretical analysis, each also has in its application a necessary uncertainty due to assumptions primarily regarding the upper atmospheres constitution and absorption properties, and the radiometric measurements themselves. It is however equally clear that the consistency in their estimated values of optical scattering ratio give strong credence to the contention that the measured values (bold face in Table 2.4) are consistently too high.

An attractive and technically profitable program would result from an increased effort in the development of these techniques and their application to the existing data bases representing the altitude regime defined by the 6 km AGL measurements.

Near-Sun Sky Radiances

The measurement of the 4π radiance field which surrounded the airborne instrument system at each flight altitude has provided a data base of wide utility. The general scope of the 4π radiance data base has been discussed and illustrated by Johnson and Hering (1981), and a basic fault existing in each of the arrays due to stray light influences, has been addressed in Johnson (1981).

As discussed at length in Johnson (1981), both the comparison of irradiances calculated from scanner radiance arrays with directly measured irradiances, and comparison of measured near-sun radiance gradients with model predictions, indicated conclusively that the near-sun radiance measurements were consistently too high. Subsequent laboratory measurements indicated that off-axis light entering the scanner's optical system was substantial at all viewing angles near the sun, and would consistently increase markedly both as the instrument's field of view approached the solar disc and as the atmospheric aerosol loading decreased.

The implications to be derived from the measurements just discussed were that high altitude or clear day measurements of sky radiances within 10° of the solar disc will have stray light ratios of as much as 20 to 35, whereas low altitude near-sun measurements through more turbid atmospheres will have substantially lower stray light ratios of about 3 to 6 at the same angular distance from the disc. There were no detectable stray light influences upon measurements made beyond 25° from the disc under any of the conditions tested. Thus, using sky radiances to predict optical scattering ratios as discussed in the preceding paragraphs will not be influenced by these effects since most of the radiances used were at scattering angles of 55° or more.

Recommendation

The application of the measured atmospheric optical properties discussed in the preceding paragraphs has led to the development of a reliable and fast operational model, Hering (1981). It is quite appropriate at this point to use the model in conjunction with the procedures outlined in Section 2.3 to provide a fully corrected set of selected scattering coefficient profiles and their associated sky and terrain radiances. These optimized data sets would provide a valuable tool in the development of next generation models, as well as accurate specifications for the identification of typical meteorological boundary conditions.

3. AIRBORNE AEROSOL MEASUREMENTS

3.1 Introduction

Aerosols play an important role in determining the characteristics of skylight, the transmittance of light, and other optical properties of the atmosphere. The more rigorous radiative transfer calculations used to predict these atmospheric optical properties need as input a model of the aerosol size distribution. Some of the models commonly used have been the modified gamma function, used by Deirmendjian (1969) to construct his haze models; the power-law size distribution function of Junge (1963); and the log-normal distribution as described by Aitchison and Brown (1957), Raabe (1971), Davies (1974), and Jaenicke and Davies (1976).

To define an aerosol distribution for a specific situation, the model fit parameters must be expressed in terms of predictable physical observables such as altitude, location, and the meteorological variables. Many research investigations have been devoted to just such a description of a maritime aerosol in the marine boundry layer. The Munn-Katz marine aerosol model, presented in Hughes and Richter (1980), and the parent model of Wells *et al.* (1977) are examples. The fit parameters of the Munn-Katz model are expressed as functions of altitude, relative humidity, and the wind speed at the sea surface. The expense and difficulty in making aerosol measurements, however, makes it difficult to investigate the behavior of the model parameters for the wide variety of atmospheric conditions that can occur in a continental or maritime environment.

The following sections present a discussion of an extensive set of measurements of the aerosol size distribution in the lower troposphere taken during the spring and fall of 1976, the summer of 1977, and the summer and winter of 1978 at eight sites in Europe and Great Britain. The data are used to explore the characteristics of the measured aerosol as a function of altitude, season, location, and relative humidity. Comparisons of the measured distributions are made to some of the more commonly used model distributions.

In a previous report by Fitch and Cress (1981), hereafter termed report 1, the characteristics and behavior of the aerosol volume distribution were explored for part of the almost 600 total measured distributions. The analysis of report 1 concentrated on the characteristics of the submicrometer volume mode, showing that it was well fit by a log-normal curve and that the behavior of the fit parameters was regular. In this report, the entire data set is analyzed and the characteristics of the entire measured volume distribution explored.

3.2 Method of Measurement

Aircraft measurements of the number and size distribution of the atmospheric aerosol were conducted along tracks of constant altitude above the ground near Yeovil and RAF Mildenhall (Great Britain), Rodby (Denmark), Meppen, Ahlhorn, and Birkhof (W. Germany), Soesterberg (Netherlands), Bruz (France), and Trapani (Italy). The Ahlhorn data was included in the Meppen data for this study because of the close proximity of the two aircraft tracks to one another, approximately 15 kilometers. All of the 50 km long sampling tracks, the locations of which are shown in Fig. 1-3 and tabulated in Table 3.2, were over land, except for the Rodby track which was over the Baltic Sea, Trapani which was over the Mediterranean Sea, and the Mildenhall track which was over the North Sea. The procedure and the instrumentation used in the measurement program have been described in detail in report 1 and by Cress (1980), and so will only be briefly reviewed here.

The aerosol number distribution was measured over particle radii from 0.2 to 5.9μm using an 89 channel Royco 220 single particle counter carried on board the C-130 aircraft illustrated in Fig. 1-1. Samples were taken in cloud free air at altitudes ranging from 150 to 6100 meters (m) above the surface. The sampling time of the Royco was typically four minutes, but occasionally samples were taken for one minute or as long as ten minutes, depending on the situation and the density of particles being counted. Sample air for the Royco was provided at about 47 cubic centimeters per second by a ram air, approximately isokinetic probe located on top of the aircraft fuselage 33 cm above the aircraft skin. The entire Royco system consisted of the Royco counter, a Technical Measurement Corporation Model 102 Gamma Scope II Pulse Height Analyzer, and a Hewlett-Packard Clock/Printer.

The Royco is a right-angle scattering counter that was calibrated with submicrometer size polystyrene spheres. Since the instrument is a right-angle scattering device, a major source of error is an inadequate knowledge of the index of refraction of the ambient aerosol. The refractive index is, unfortunately, difficult to measure and so is rarely known in measurements of size distributions. The error in measured particle size associated with the effects of refractive index can be estimated from laboratory measurements for an average range of probable indices. In such an investigation Quenzel (1969) found a maximum sizing error of a factor of 2 to 3. A ground based intercomparison study between a Royco 220 and active and classical Particle Measurement Systems aerosol counters showed agreement to within a factor of 2 to 5 in particle concentration (Cress, 1980).

Another source of error may have been the modification of the physical properties of the ambient aerosol sample as it passed from outside the aircraft to the Royco scattering chamber. Possible modifications to the aerosol sample could have been the result of a drying of the particles or a selective loss of particles. The small number of changes in the direction of flow within the plumbing probably minimized the effects of particle loss. According to the investigations of report 1 and Cress (1980), the characteristics of the measured aerosol probably represent the influence of a relative humidity of lower value than the measured ambient value. Although this could have reduced the sizes overall, the shape of the major features of the distribution were likely preserved due to the small size range measured. Comparison of consecutive one minute data samples indicate that the repeatability of the airborne Royco was good.

3.3 Results of Measurements

For many years size distribution data has been presented in figures of $\log(dN/d\log r)$ versus $\log r$ where r is the particle radius and N is the total number density of particles smaller than r. The measured distributions are generally compared to a common size distribution formula such as the one developed by Junge (1963): $dN/d\log r = cr^{-\beta}$ where c is a constant depending on the total number of particles and β is estimated to be about 3 for particle radii between 0.3 and 10μm, (Junge and Jaenicke, 1971). This power-law size distribution was fit to the data collected in Great Britain and Europe and the results presented in Cress (1980). The investigation shows that, overall, the value of β is in the range 3 to 6 for data collected within the mixing layer and has a value close to 2 for data collected above the layer.

Departures of the measured size distribution from the power-law distribution appear small on the four or five log cycles traditionally used in figures of aerosol number distribution. These small departures were found, however, to yield multi-mode curves when the data were plotted as volume (or mass) versus particle size, as pointed out by Whitby *et al.* (1972) and Shettle (1975). The appearance of a volume mode is demonstrated in Fig. 3-1 which presents an aerosol distribution measured at Mep-

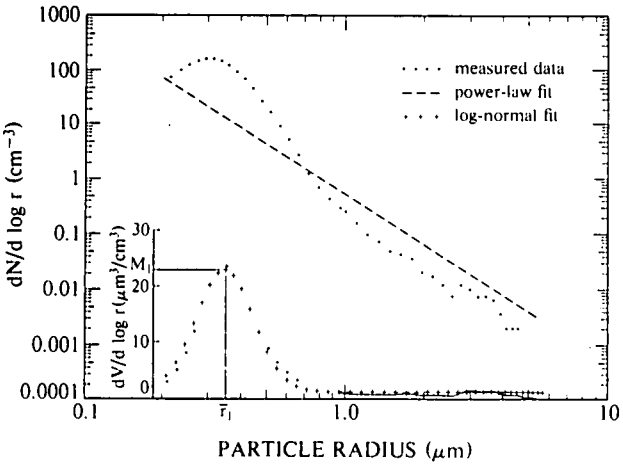

Fig. 3-1. A comparison of the aerosol number and volume distributions as a function of particle radius for data taken at Meppen during August at an altitude of 457m above the ground. The fit of a power-law distribution with a slope of -3 to the number distribution (dashed line) and the fit of Eq. (3.1) to the volume distribution (+) are, also, shown.

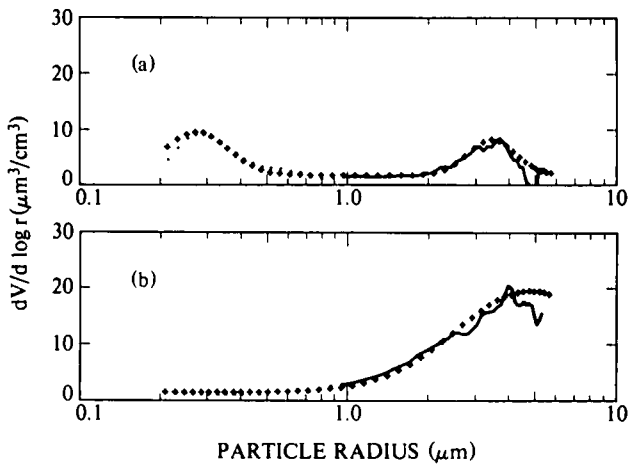

Fig. 3-2. The volume distribution sampled at Soesterberg during August at an altitude of 152m (a) and at Birkhof during February at an altitude of 1219m (b). The fit of Eq. (1) to the data (+) is shown for comparison.

pen during the month of August at an altitude of 457m above the ground. The data is displayed in terms of a number distribution $dN/d\log r$ and a volume distribution $dV/d\log r$ where $dV/d\log r = 4/3\ \pi\ r^3\ dN/d\log r$. Only the data from every other Royco channel, as shown by dots, is displayed. The data at particle radii greater than $1\mu m$ was smoothed using an equally weighted seven point average. The smoothed data is shown as a solid line in the volume display.

The curves of Fig. 3-1 demonstrate that departures of a measured number distribution from a fitted Junge distribution with β=3 (dashed line) can translate into modes when the data are plotted as a volume distribution. A Junge distribution with β=3 would appear as a straight horizontal line in the volume display. The mode in the submicron region was termed the accumulation mode by Whitby (1978), who stated that its main source of mass is from the coagulation of the smaller size aerosols and from gas to particle conversion of generally anthropogenic origin. A similarly shaped mode centered at radii greater than $3\mu m$, shown later in Fig. 3-2, was termed the coarse mode by Whitby (1978) and is considered to have sources such as wind blown dust and sea spray, which tend to make its characteristics independent of those of the accumulation mode. A fit of the volume distribution with a log-normal curve (+) is shown in Fig. 3-1 for comparison and will be discussed in the next section.

The limited number of investigations into the nature of an aerosol's volume distribution and the large spread in the values of β from the power-law fit to the data (Cress, 1980) prompted an analysis of the data using the volume size display. This analysis does not represent an attempt to define a new aerosol model but is intended to demonstrate the detail with which an aerosol distribution can be described using the volume display. The first part presents a mathematical description of the volume distribution. Subsequent sections discuss the relationships between the fitting parameters and how the aerosol distribution behaves as a function of altitude, humidity, season, and site of measurement.

3.4 Fitting Function

An examination of volume distributions for the entire data set revealed that a majority of the modes fall into the accumulation or coarse particle mode categories. There are a small but significant number of cases, however, when the volume display showed the presence of a mode centered between the regions generally assigned to the accumulation and coarse particle modes. The presence of this middle mode, necessitated a model fit consisting of three log-normal distributions. By using three separate log-normal curves to fit the data, the features of the accumulation and coarse particle modes, together with the characteristics of the curious middle mode, could be studied individually. The model used to fit the data was

$$\frac{dV}{d\log r} = \sum_{i=1}^{3} M_i \exp\{-0.5[(\log r - \log \bar{r}_i)/\sigma_i]^2\} + k \quad (3.1)$$

where k is a constant, σ the standard deviation, $\bar{r}$ the mode radius, and M the value of $dV/d\log r$ occurring at the mode radius, as demonstrated for the accumulation mode in Fig. 3-1. The values i = 1-3 refer to the accumulation, middle, and coarse modes, respectively. The quantity M may also be expressed as $M = V/\sigma(2\pi)^{1/2}$, where V is the total particle volume of the mode. To more easily

visualize the character of the entire volume distribution the value M was used instead of the equivalent expression containing V. The least-squares fit of Eq. (3.1) to the volume distribution was performed using the algorithm of Marquardt (Bevington, 1969).

The result of fitting Eq. (3.1) to a volume distribution containing an accumulation mode was shown in Fig. 3-1. To obtain a good fit for this example, only the constant and one log-normal curve were needed. A bimodal distribution is shown in Fig. 3-2a for data collected at Soesterberg in August at an altitude of 152m above the ground. The data is well fit using the constant of Eq. (3.1) and two log-normal curves, one to fit the accumulation mode and the other to fit the coarse particle mode. Cases were found not only of the accumulation mode existing solo, as shown in Fig. 3-1, but also of the coarse particle mode as the only mode in the measured volume distribution. Figure 3-2b shows a coarse particle mode measured at Birkhof in February at an altitude of 1219m. The data are well fit in this case with only one log-normal distribution and the constant. Two measured aerosol distributions showing the middle mode are depicted in Fig. 3-3 for Yeovil in March at 152m, Fig. 3-3a, and for Rodby in March at 152m, Fig. 3-3b. In addition to existing solo or with an accumulation mode, as shown in Fig. 3-3, the middle mode was found in the presence of the accumulation and coarse particle modes together (not shown).

The fit of a log-normal distribution to the accumulation modes presented in Figs. 3-1, 3-2a, and 3-3b shows that Eq. (3.1) consistently overestimates the data in the first eight to ten Royco channels. Remember that only every other data channel is shown in the figures. This over estimation may be the result of a modification to the aerosol distribution in the Royco plumbing or a departure of the actual aerosol distribution from a log-normal distribution.

To judge how well Eq. (3.1) fit the entire data set, the value chi-square was calculated, but it is only a relative indication of how good the fit is because the uncertainty of the data is unknown. For purposes of comparison, the values of chi-square for Figs. 3-3a and 3-3b, which are almost equal, were exceeded by 20 to 25% of the fitted data and for twice the values of chi-square by about 10% of the data. A majority of the large values of chi-square are associated with the presence of a coarse particle mode. Even though a coarse particle mode appears large compared to one of the other volume modes it can be heavily influenced by random errors in counting since it may represent a much smaller number of counted particles per channel. For example, a value of $20\mu m^3/cm^3$ represents about 3000 times the number of counted particles for the Royco channel with a mean radius of $0.3\mu m$ than for the channel with a mean radius of $4.0\mu m$.

In the next section the characteristics of the three modes and the constant will be discussed individually. After which, the frequency of occurrence of the modes in different combinations as a function of altitude, season, relative humidity, and site of measurement will be presented.

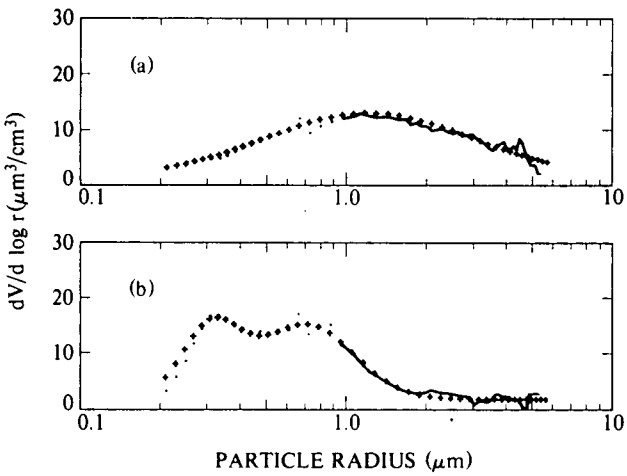

Fig. 3-3. The volume distribution sampled at Yeovil (a) and at Rodby (b) during March at an altitude of 152m. The fit of Eq. (1) to the data (+) is shown for comparison.

3.5 Results of the Fit

Three parameters (M, $\bar{r}$, and σ) are required to define each of the three log-normal curves used to fit the volume modes. The behavior of these three parameters and the constant, defined in Eq. (3.1), is of interest in ascertaining the predictability of a mode's characteristics. The accumulation mode is heavily influenced by anthropogenic sources of aerosol, and dominates scattering of radiation in the visible part of the spectrum.

Accumulation Mode

A radiative transfer model used to calculate the distribution of light in the atmosphere must in some manner approximate the behavior of this mode as a function of altitude. The characteristics of this mode, for the aerosol samples collected at the many different sites and under differing meteorological conditions, were compared by plotting these characteristics against the ratio of the measurement altitude to the altitude of the inversion base (altitude ratio). The height of the inversion was determined by two methods. The first method used the temperature profile of the atmosphere measured using the airborne temperature transducer during ascents and descents of the aircraft. The second was based on estimates of the top of the surface haze layer made by an on-board observer. A comparison of the inversion height estimated from both these methods, shown in Fig. 3-4, shows that the two methods are in general agreement with one another. Data departures from the expected straight line agreement may be in part due to differences of two to three hours between the times the on-board observer estimated the inversion height and the aircraft flew a vertical profile.

The behavior of the accumulation mode with altitude is illustrated in Fig. 3-5 which shows values of the fit parameter M_1 versus altitude ratio. The figure shows that

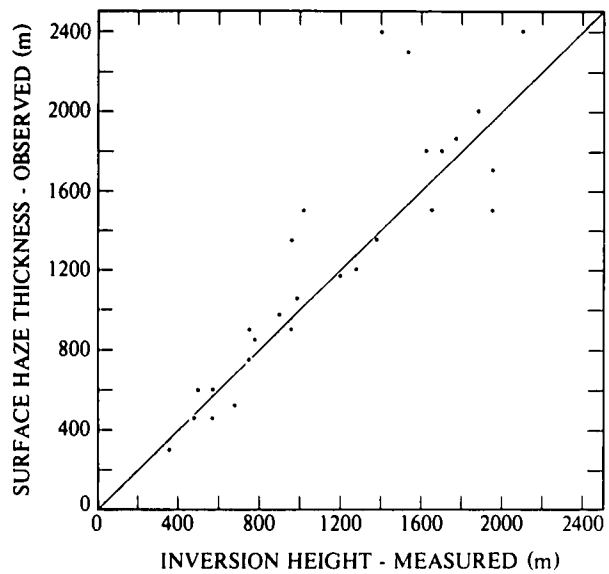

Fig. 3-4. A comparison between the thickness of the surface haze layer as estimated by the on-board observer and the height of the inversion base as determined from the measured temperature profile.

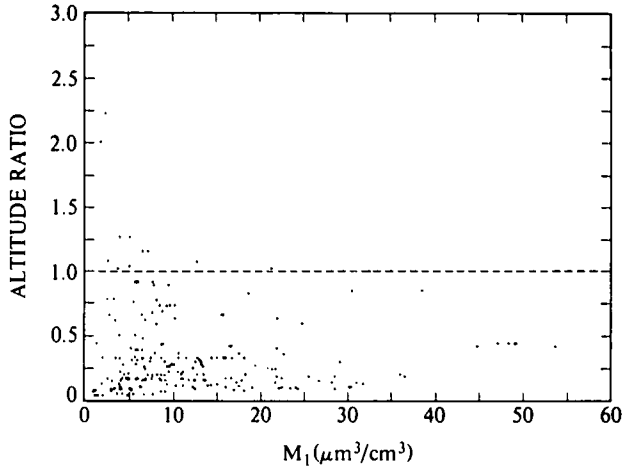

Fig. 3-5. The altitude ratio, *i.e.* ratio of the aircraft altitude during measurement to the thickness of the mixing layer, as a function of the maximum volume concentration in the accumulation mode, M_1.

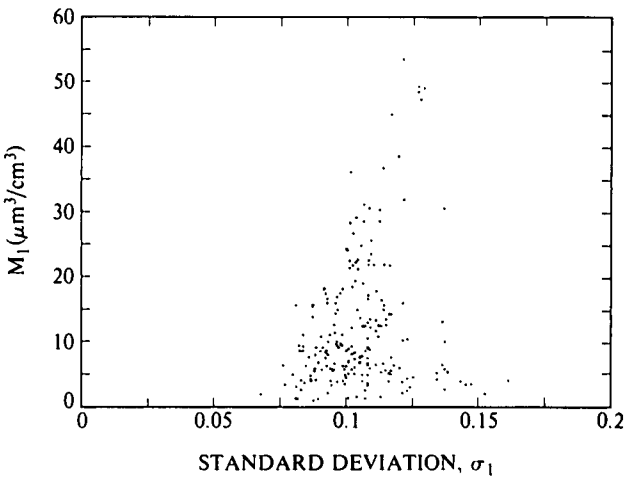

Fig. 3-6. The maximum volume concentration M_1 as a function of the standard deviation σ_1 for the accumulation mode.

for this data set the accumulation mode rarely exists above the inversion layer, an altitude ratio of 1.0. Of the nearly 200 occurrences of this mode shown in the figure, only 9 clearly exist above the mixing layer. To eliminate modes artificially created by the fitting routine, cases where M_1 was less than $0.5\mu m^3/cm^3$ and $\bar{r}_1$ was less than $0.25\mu m$ - the fifth Royco channel - were ignored.

Often times in the literature, the accumulation mode is presented in terms of its total particle volume concentration V which for a log-normal distribution is equal to $M_1\,\sigma_1(2\pi)^{0.5}$. A knowledge of σ_1 as a function of M_1 would simplify determinations of V and would reduce the number of independent variables in Eq. (3.1). The values of σ_1 are compared to the corresponding value of M_1 in Fig. 3-6. The fairly narrow distribution of the data points about the average value of σ_1 for the data of the figure indicates that σ_1 may be a constant, independent of the value M_1. The average value of σ_1 is 0.11. It is possible, though, that random error has masked a relationship between M_1 and σ_1. The five data points existing in the region of M_1 greater than $45\mu m^3/cm^3$ and $\sigma_1 \approx 0.125$ represent data collected at Rodby on October 25 and 26 in a very heavy haze near the surface of the Baltic Sea. The Cambridge dewpoint hygrometer measured values of relative humidity of over 90% when these samples were collected. These five points might be representative of conditions in a heavy haze.

A comparison between the values of M_1 and $\bar{r}_1$ is shown in Fig. 3-7. The data, which shows increasing values of M_1 with increasing values of $\bar{r}_1$, are fit remarkably well by a straight line as shown in the figure. The regression line (solid line) was fit to the data using the least squares criterion and explains 89% of the observed variation in the values of $\bar{r}_1$ from the values of M_1. The linearity of the data distribution is a result of opposing trends in $\bar{r}_1^3$ and $dN/d\log\bar{r}$, upon which M_1 depends. The dashed line in Fig. 3-7 is a curve of the values $M_1=4/3\,\pi\,\bar{r}_1^3\,70$, where $dN/d\log r$ has been fixed at 70 particles per cm^3. In comparison, the trend in the values of $dN/d\log r$ are represented in Fig. 3-8, which shows the measured values $M_1/\bar{r}_1^3$ averaged over increments of $0.025\mu m$ in radius. The solid line, the result of a hand fit to the averages, shows the trend in $dN/d\log r$. It appears that the opposing trends - sign of the second derivative - of the $\bar{r}_1^3$ and the $M_1/\bar{r}_1^3$ dependence shown in Figs. 3-7

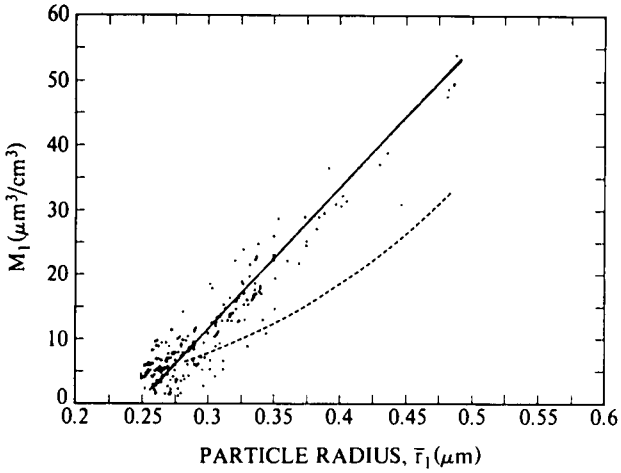

Fig. 3-7. The maximum volume concentration M_1 as a function of the mode radius $\bar{r}_1$ for the accumulation mode. A straight line fit to the data (solid line) and the $\bar{r}^3$ dependence of M (dashed line) are shown for comparison.

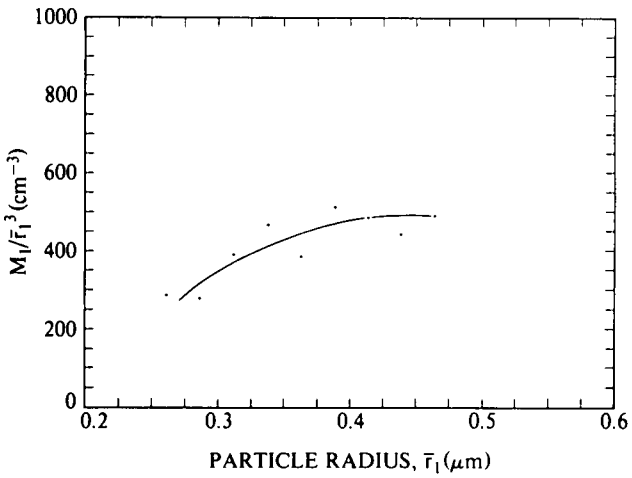

Fig. 3-8. The relative change in number density at the mode radius of the accumulation mode as expressed by the ratio $M_1/\bar{r}^3$.

and 3-8, respectively, is responsible for the linearity of the relationship between M_1 and $\bar{r}_1$ for this data set.

There is no tendency for the relative humidity to be high for the larger values of $\bar{r}_1$. This dependency was explored in report 1 in which it was found that any dependence on humidity was mainly due to the influence of the Rodby data collected in a heavy haze. When the entire data set, as shown in Fig. 3-7, is used no tendency is found for the relative humidity to be greater than or equal to 70% when the value of $\bar{r}_1$ is greater than or equal to $0.34\mu m$. The probability is almost 0.2 that the value of chi-square will be equaled or exceeded by a random sample. The lack of an apparent dependence of $\bar{r}_1$ on relative

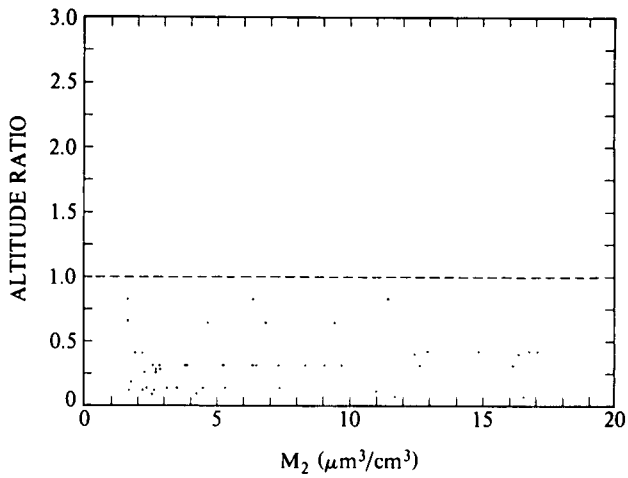

Fig. 3-9. The altitude ratio as a function of the maximum volume concentration M_2 for the middle mode.

humidity may be due to a possible drying of the aerosol sample by this particular measuring system.

Middle Mode

As shown in Fig. 3-3 there is a mode that exists between the regions generally associated with the accumulation and coarse particle modes. A plot of the values of the fit parameter M_2 for the middle mode as a function of altitude ratio is shown in Fig. 3-9. The data of the figure show that the middle mode exists only within the mixing layer and, most often, in the lower half of the layer. The values M_2 for the middle mode never get as large as the values M_1 for the accumulation mode as seen by comparing Figs. 3-9 and 3-5. To reduce the influence of errors associated with low particle counts, only values of $M_2 \geq 1.5\mu m^3/cm^3$ are presented. False middle modes caused by deviations between the log-normal fit to either an accumulation or a coarse particle mode were reduced by ignoring cases where the value M_2 was less than 20% of the value M for the accumulation or coarse modes when present.

The standard deviation for the middle mode σ_2 is compared to M_2 in Fig. 3-10 for all of the cases presented in Fig. 3-9. The data are broadly distributed around the average value of σ_2, which is 0.29 for the data shown in the figure. The variation in the data is not associated with any one set of aerosol samples but appears to be the result of random errors. The discrepancy in the data can be approximated by examining the differences in the values σ_2 for two middle modes measured within 6 minutes (0.1 hrs.) of each other. The average value of the difference in σ is 0.08, which represents errors in particle counting, nonhomogenities in the aerosol distribution at a given altitude and errors in fitting Eq. (3.1) to the data.

The values of $\bar{r}_2$ for the middle mode are presented in Fig. 3-11 along with the corresponding values of M_2 as

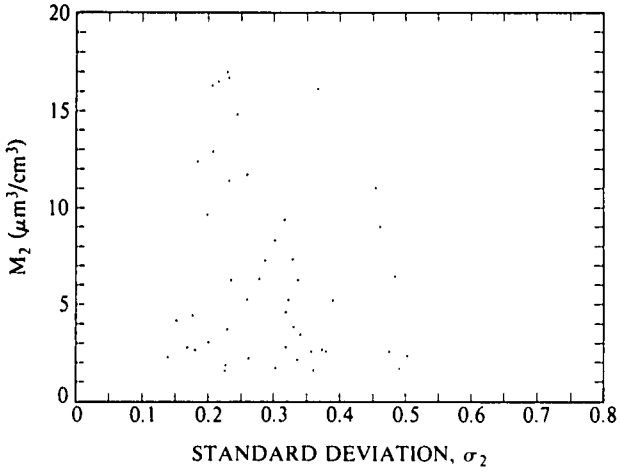

Fig. 3-10. The maximum volume concentration M_2 as a function of the standard deviation σ_2 for the middle mode.

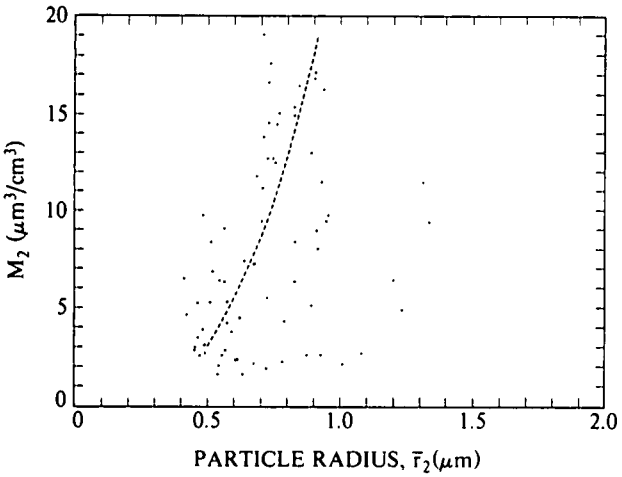

Fig. 3-11. The maximum volume concentration M_2 as a function of the mode radius $\bar{r}_2$ for the middle mode. The $\bar{r}^3$ dependence of M is shown for comparison (dashed line).

determined from the fit. Shown in the figure for comparison is the $\bar{r}^3$ dependence of M for constant particle number (dashed line). The figure shows that the middle mode most frequently occurs in the size range 0.5 to $1\mu m$. The data points existing at $\bar{r} > 1\mu m$ were not collected at one particular data site and probably represent the ambient aerosol, even though they are based on relatively small particle counts. A $dV/d\log r$ value of $5\mu m^3/cm^3$ at $\bar{r} = 0.6\mu m$ represents about seven times the number of particles than at $\bar{r} = 1.2\mu m$. When the data of the figure are plotted as $M_2/\bar{r}_2^3$, a general trend of decreasing particle number is seen.

Coarse Particle Mode

The third mode appearing in the volume distribution

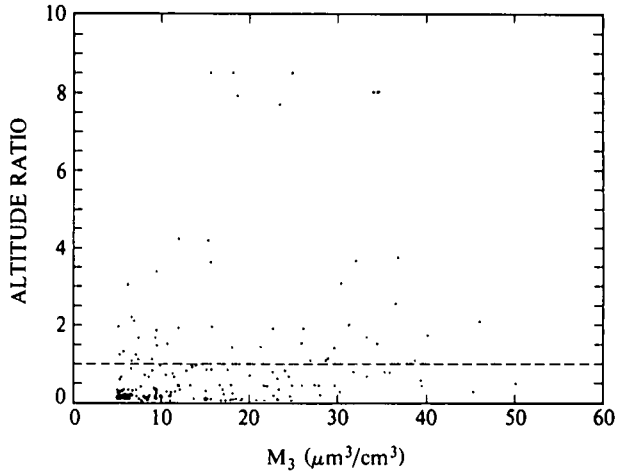

Fig. 3-12. The altitude ratio as a function of the maximum volume concentration M_3 for the coarse mode.

plots of the data is the coarse particle mode. Its source is generally considered to be the result of mechanical processes, such as wind blown dust. A representation of its behavior with altitude is demonstrated in Fig. 3-12 which shows values of M_3 for the coarse mode as a function of altitude ratio. To reduce the influence of errors associated with low particle counts, only values of $M_3 \geq 5\mu m^3/cm^3$ have been displayed. The figure clearly demonstrates that the coarse mode is not confined to the mixing layer as were the accumulation and middle modes. On numerous occasions the on-board observer reported the existence of haze layers above the surface haze layer. Individual examples of haze layers existing at altitude ratios greater than 1.0, which appear to contain coarse mode particles but no accumulation mode particles, were presented in report 1. The set of seven data points in Fig. 3-12 centered around the altitude ratio 8 are from measurements taken at Rodby and Birkhof. The Rodby data were collected in the altitude range 5000 to 6000m above the sea surface, while the Birkhof data were collected at an altitude of about 3000m above the ground. It is possible that this high altitude aerosol was transported from the south since a majority of the occurrences of the coarse particle mode occurred at Trapani, as will be shown in Table 3.2 in the following section. A trajectory analysis of the air mass containing the coarse mode particles would be necessary to confirm this.

The fit parameter σ_3 is plotted in Fig. 3-13 as a function of M_3 for all of the data presented in Fig. 3-12. The large spread in the data, which may well be masking a dependence between M_3 and σ_3, is probably mostly due to noise. The average deviation in σ_3 is 0.09 for data samples collected within 6 minutes of one another. The data are fairly well distributed about the value 0.21, the average value of σ_3. The data points near the upper right hand corner of the figure, with σ_3 in the range 0.3 to $0.4\mu m$, do not represent data from one particular station or month.

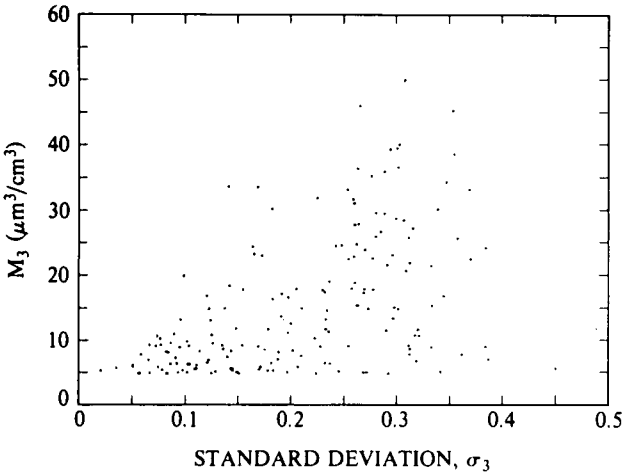

Fig. 3-13. The maximum volume concentration M_3 as a function of the standard deviation σ_3 for the coarse mode.

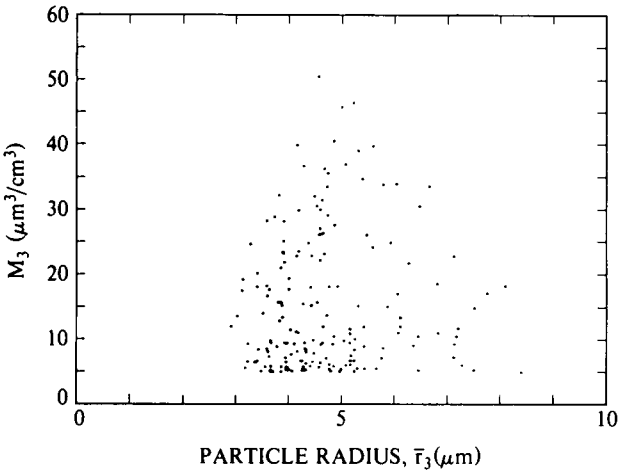

Fig. 3-14. The maximum volume concentration M_3 as a function of the mode radius $\bar{r}_3$ for the coarse mode.

The values of $\bar{r}_3$ for the coarse particle mode are shown in Fig. 3-14 with the corresponding values of M_3. The distribution of data points in the figure is noticeably asymmetric around the average value of the mode radius for the data, $\bar{r}_3 = 5\mu m$. The lack of any data points in the region $M_3 > 5\mu m^3/cm^3$ and $\bar{r} < 3\mu m$ is not the result of a deliberate filtering of the data. It should be noted that the last channel of the fitted Royco data had a mean radius of $5.9\mu m$, which is probably responsible for the lack of symmetry in the data. Modes with a value of $\bar{r}_3$ in the region of $5.9\mu m$ or greater may, therefore, be an artifact of the model fit which assumes a log-normal shape for the coarse mode. A comparison between the values of $\bar{r}$ for the middle and coarse particle modes, as shown in Figs. 3-11 and 3-14, respectively, shows a distinct break between these

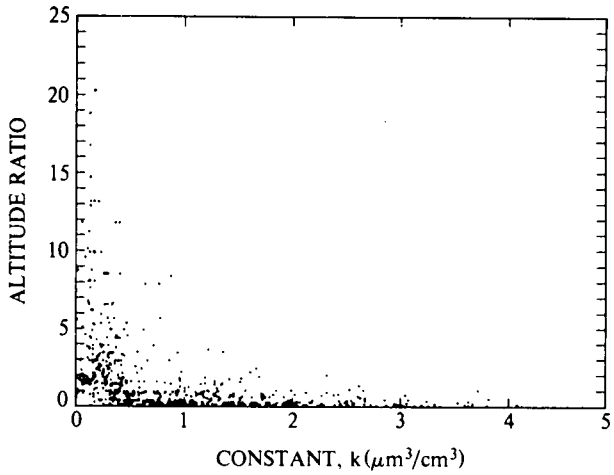

Fig. 3-15. The altitude ratio as a function of the constant k of Eq. (3.1).

modes at a particle radius centered around $2\mu m$.

The Constant

In addition to the three log-normal distributions that were used to describe the volume modes, a constant k was included in Eq. (3.1). The need for the constant is demonstrated by the zero offset of the example aerosol distributions presented in Figs. 3-1 to 3-3 and by the many cases where there is no discernible mode present in the volume distribution. The value of the constant as a function of altitude ratio is shown in Fig. 3-15 for all of the fitted data. As seen in the figure, the value of k appears to decrease with increasing altitude ratio, reaching a maximum of about $4\mu m^3/cm^3$ near the ground and close to $0.2\mu m^3/cm^3$ at the highest altitude where measurements were made.

Values of k averaged over atmospheric layers of increasing thickness with increasing height are shown in Fig. 3-16 plotted against the mean value of altitude ratio for the slab layer (circled points). At altitude ratios of greater than 1 the average values of the constant are fit well by an equation of the form

$$\bar{k} = 0.12 + 0.82(1/z) \qquad (3.2)$$

where $\bar{k}$ is the average and z is altitude ratio. This equation explains 96% of the variation in $\bar{k}$. A straight line was fit to the three values of $\bar{k}$ below z=1.

The value of k represents an estimation of the residual total particle volume of the aerosol distribution after the log-normal approximations to the modes, if present, are subtracted out. No clear relationship between k and the values of M for the three modes could be found. It appears that there is a trend of increasing k with increasing total particle volume of the three modes, but the

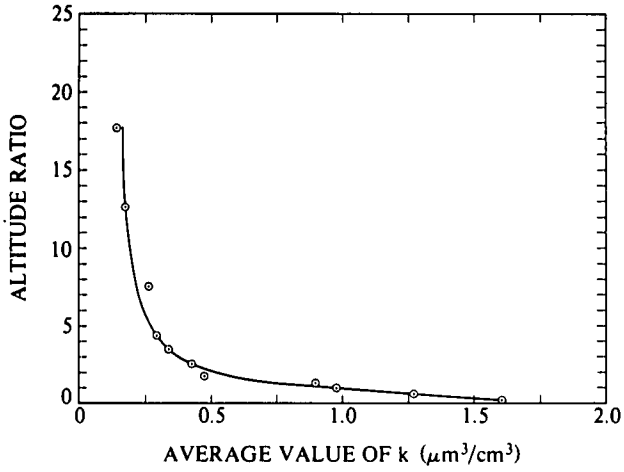

Fig. 3-16. The altitude ratio as a function of k averaged over atmospheric layers of increasing thickness with increasing height. The solid line represents a functional fit to the average values of k.

scatter in the data is great. Depending on how accurate the aerosol data need to be fit, it may be possible to drop the constant from Eq. (3.1) when a volume mode is present. For example, report 1 showed that the measured volume scattering coefficient at the wavelength $0.66\mu m$ was well correlated with the value M_1 of the accumulation mode, independent of the value k.

3.6 Combinations of the Modes

In the previous section, the behavior of the three modes and the constant with altitude was studied, along with the dependence of $\bar{r}$ and σ on M for each of the modes. It is of interest, now, to explore how frequently in the data base various combinations of the modes occur and if the frequency of occurrence of the combinations shows a preference toward altitude, season, relative humidity, or site of measurement.

The first two columns of Table 3.1 present the number of occurrences of the different combinations of the modes within and above the mixing layer. Each of the possible combinations are labeled using *a*, *m*, or *c* to denote the accumulation, middle, or coarse particle modes, respectively. The label none refers to the absence of a discernible mode. The volume distributions listed under none were fit with only the constant of Eq. (3.1), which, for this case only, is equivalent to a fit of the aerosol number distribution using a Junge distribution with $\beta=3$. The figures in parenthesis give the distribution which would be expected if there were no tendency for the different mode combinations to exist either at $z \leqslant 1$ or $z > 1$. The table shows that combinations containing the accumulation or middle modes rarely exist above the mixing layer, as seen in Figs. 3-5 and 3-9. In contrast, the coarse mode solo, row *c*, is equally likely to occur above as within the mixing layer as seen by the small differences

Table 3.1. The occurence of different combinations of the modes as a function of altitude ratio, season, and relative humidity.

	$z \leqslant 1$	$z > 1$	Summer	Winter	RH<70	RH≥70
a	85 (53)	3 (35)	58 (39)	30 (49)	35 (39)	50 (46)
a-m	15 (9)	0 (6)	1 (7)	14 (8)	4 (7)	11 (8)
a-c	53 (34)	4 (23)	46 (25)	11 (32)	33 (23)	18 (28)
m	19 (11)	0 (8)	4 (8)	15 (11)	4 (9)	15 (10)
m-c	5 (3)	0 (2)	0 (2)	5 (3)	3 (2)	2 (3)
a-m-c	18 (11)	0 (7)	2 (8)	16 (10)	3 (8)	15 (10)
c	43 (48)	37 (32)	35 (35)	45 (45)	29 (17)	8 (20)
none	88 (157)	175 (106)	94 (116)	169 (147)	30 (35)	47 (42)

between the measured number of occurrences above and within the mixing layer and those expected from chance. Samples taken within 10 minutes of one another at the same altitude were counted as one sample to help reduce the bias introduced by multiply sampling the same ambient aerosol. In addition to showing where the different mode combinations are likely to occur in the atmosphere, the first two columns of Table 3.1 indicate what combinations are least prevalent. For $z > 1$, it is likely that no mode will be observed in a volume distribution plot as seen from the large number of occurrences of none compared to the other possible combinations. The combination of a middle mode with another mode at $z \leqslant 1$ will probably be measured infrequently according to this data base. It is more likely that at $z \leqslant 1$ an accumulation mode will be measured solo or in combination with a coarse mode.

The third and fourth columns of Table 3.1 indicate the seasonal preference of the combinations. The summer season was defined for this investigation to include the months April to August, the other months of the year defining the winter season. The table shows that the middle mode, either solo or in a combination, tends to occur in the winter months. The coarse mode by itself shows no preference toward season, while the combinations *a* and *a-c* are likely to occur in summer. Combinations including *a* and *m*, which show a tendency to occur in the summer and winter seasons, respectively, show the largest values of M in those respective seasons. The combination none indicates a preference toward winter.

The last two columns of Table 3.1 indicate the preference of the various combinations for high or low humidity. The data presented in these columns represent aerosol samples collected within the mixing layer only, thus avoiding freezing temperatures that can occur at higher altitudes. The total number of measured samples in the last two columns may be less than the number of samples in the first column, for a given combination, since for some samples no value of relative humidity is available. As shown in the table, the combinations *m*, *a-m*, and *a-m-c* which contain the middle mode show a strong tendency to exist at the higher values of relative humidity. The coarse mode, in contrast, shows a strong tendency to exist at the lower values of relative humidity when in combinations of *a-c* and *c*. The apparent preference of *a*, *a-m*, and none toward the higher values of humidity is not large enough to be statistically significant.

Table 3.2. The Occurrence of Different Combinations of the Modes as a Function of Site.

$z \leq 1$	Trapani		Birkhof		Rodby		Meppen		Soesterberg		Bruz		Mildenhall		Yeovil	
	Num.	%	Num.	%	Num.	%	Num.	%	Num.	%	Num.	%	Num.	%	Num.	%
a	2	3	6	13	19	45	24	41	12	44	8	24	3	38	11	31
a-m	0	0	0	0	5	12	7	12	1	4	0	0	1	13	1	3
a-c	18	24	2	4	0	0	8	14	6	22	12	35	2	25	5	14
m	2	3	0	0	4	10	5	9	0	0	1	3	0	0	7	20
m-c	0	0	0	0	0	0	1	2	0	0	0	0	0	0	4	11
a-m-c	0	0	0	0	6	14	4	7	5	19	1	3	2	25	0	0
c	28	38	11	23	0	0	1	2	1	4	1	3	0	0	1	3
none	24	32	29	60	8	19	8	14	2	7	11	32	0	0	6	17
$z > 1$																
c	9	27	17	26	6	20	0	0	1	7	3	18	0	0	1	3
none	24	73	48	74	24	80	18	100	14	93	14	82	2	100	31	97

The number of times the different mode combinations appear in the volume distributions for the different sites of measurement is shown in Table 3.2. The percent of the total number of flights each combination represents within and above the mixing layer, separately, is shown for each site. The two most southeastern sites, Trapani and Birkhof, show the highest percent of occurrence of the coarse particle mode solo, row *c*, both within and above the mixing layer. From examination of synoptic charts at the time of these measurements it is possible that the coarse mode material had its origin in Northern Africa. It is interesting that the solo coarse mode exists both above and within the mixing layer for the two most southeastern sites, but its existence for the other stations is mainly confined to altitudes above the inversion height. Table 3.2 shows that the accumulation mode, row *a*, occurs more frequently for the northern most stations. The middle mode in combination with other modes and solo appears to predominate at Rodby, Meppen, Soesterberg, and Yeovil. The percent of occurrence in which there was no discernible volume mode is large at altitudes above the mixing layer, as seen in the table. Within the mixing layer, the southern most stations Trapani, Birkhof, and Bruz show the greater occurrence of the combination none. The number of measured aerosol samples from Mildenhall are too small to see a pattern for this site.

The data presented in Tables 3.1 and 3.2 indicate that the volume modes are tied to the characteristics of the air mass containing the aerosol sample. There is a definite dependence of the modes on altitude, season, and site. The dependence on relative humidity was very strong for the combinations *c* and *a-c*, which were frequently measured at values of low humidity. The dependence was not as definite for the combinations showing a preference for the higher values of humidity, a possible result of a drying of the sample in the intake plumbing.

3.7 Discussion and Conclusions

An extensive set of aerosol size distributions measured in the lower troposphere over Europe and Great Britain were analyzed using a volume (mass) display. As has been recognized in the past, departures of the aerosol number distribution from a power-law distribution give rise to volume modes. The analysis of the characteristics and behavior of the volume modes supports the following conclusions:

1. The volume distribution can be described well by Eq. (3.1), which uses a log-normal distribution to describe the individual volume modes. The data show that there are three distinct modes: accumulation, middle, and coarse.
2. The accumulation mode almost always exists within the mixing layer. Its value of mode radius is in the range 0.25 to 0.47μm and it is well described as a linear function of the maximum volume of the mode, M_1. The standard deviation σ_1 is probably a constant of value 0.11.
3. The middle mode is confined to the mixing layer and, generally, to the lower half of the layer. The values of $\bar{r}_2$ are in the range 0.45 to 1.4μm. Most of the data follows a trend of increasing M_2 with increasing $\bar{r}_2$, however, all the data show a general trend of decreasing $M_2/\bar{r}_2^3$ with increasing $\bar{r}_2$. The values of σ_2 appeared to be centered around a mean value of 0.3.
4. The data indicate that the coarse particle mode can exist either above or within the mixing layer. Any relationships between M_3, σ_3, and $\bar{r}_3$ that may exist for this mode are masked by what appears to be the influence of random noise. The mean values of σ_3 and $\bar{r}_3$ for the fitted data set are 0.2 and 5μm, respectively.
5. In addition to the three log-normal distributions used to describe the aerosol volume distribution, a constant was used in Eq. (3.1). The value of the constant is generally less than the value of M for

any of the modes analyzed. The values of the constant averaged over intervals of altitude ratio are found to be well described by an equation of the form $\bar{k} = a+b/z$ where a and b are constants, z is altitude ratio, and $\bar{k}$ is the average value of the constant.

6. Within the mixing layer the most common combinations of the modes are: no mode at all, the accumulation mode solo, the accumulation and coarse mode together (bimodal distribution), and the coarse mode solo. There is a small but significant number of occurrences of the combinations: middle mode solo; accumulation, middle, and coarse modes together; and accumulation and middle modes together. The combination of the middle and coarse modes rarely occurs. Above the mixing layer the combination no mode predominates.
7. The middle mode tends to be measured in the winter season, while the accumulation mode solo appeared more often in the summer data than expected from random chance. The occurrence of the coarse particle mode solo showed no preference toward season.
8. The middle mode appears more often when the relative humidity is high, but the coarse particle mode shows a preference toward the low values of humidity. The accumulation mode shows no significant dependence on relative humidity. The relative humidity dependence may have been affected by a drying of the aerosol in the intake plumbing.
9. The northern most stations, Rodby, Meppen, and Soesterberg, show a higher occurrence of the accumulation mode than the southern sites. The southern sites, in contrast, show a larger number of measured coarse particle modes than the northern stations. The middle mode seems to occur most frequently at Rodby, Meppen, Soesterberg, and Yeovil.

There have been a number of aerosol models developed over the last two decades that have been used to describe the aerosol size distribution, as mentioned in the introduction. Several of these models, presented in a volume display, are shown in Fig. 3-17. The curves labeled 1 to 4 of Fig. 3-17a represent the aerosol distribution predicted from the Munn-Katz maritime model. The model consists of a background continental component which is a function of relative humidity only, and a maritime contribution which is considered to be a function of relative humidity, wind speed, and altitude. For the four curves the respective values of relative humidity, wind speed, and altitude are: 1) 70%, 6m/s, 150m, 2) 80%, 4m/s, 150m, 3) 70%, 4m/s, 150m, and 4) 70%, 4m/s, 1200m. The continental component appears as a straight horizontal line in the volume display. While the model does depend on several scaling factors, the four curves show that the effects of the maritime component predominate at particle radii greater than $1\mu m$. The rural and maritime models of Shettle and Fenn (1979), who use a

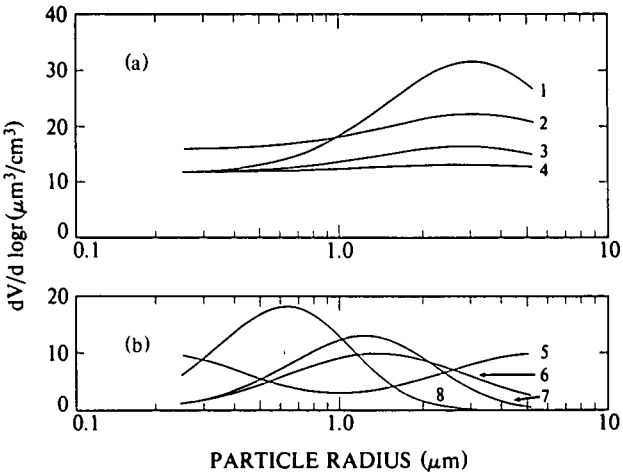

Fig. 3-17. Volume distribution plots based on the Munn-Katz maritime aerosol, curves 1 to 4 (Hughes and Richter, 1980); a rural and maritime model, curves 5 and 6, respectively (Shettle and Fenn, 1979); and the Haze *M* and Haze *L* models, curves 7 and 8, respectively (Deirmendjian, 1969).

log-normal distribution, are shown by curves 5 and 6, respectively, of Fig. 3-17b for a relative humidity of 70%. The shape of curve 5 implies a bimodal distribution. The model standard deviations are constants of value 0.35 for the maritime and the submicrometer rural modes and 0.4 for the rural coarse particle mode. As the relative humidity changes from 0 to 99%, the mode radii vary from 0.19 to 0.37, 5.5 to 15, and 1.1 to $5.3\mu m$ for the two modes of the rural model and the single mode of the maritime model, respectively. The curves labeled 7 and 8 represent the Haze *M* (marine or coastal) and Haze *L* (continental) models, respectively, of Deirmendjian (1969), as taken from his Table 5. The total particle volume of the Haze *M* model was adjusted for the purpose of display. The difference between the mode radii of the similar curves 6 and 7 and the curves of the Munn-Katz model might represent differences in the formation history of the aerosols stressed by these maritime models. The Munn-Katz model may stress a pure wind generated aerosol while curves 6 and 7 may represent a more mature maritime aerosol with some continental influence.

It is interesting that the models presented in Fig. 3-17 not only give rise to volume modes of a similar shape to those seen in the data but suggest the presence of three separate aerosol regimes. The submicrometer continental aerosol modes of curves 5 and 8 form the first region with mode radii in the range 0.2 to about $0.6\mu m$, the second region is composed of the maritime modes of curves 1 to 4, 6, and 7 with mode radii in the range from about 1 to $3\mu m$, and the large particle mode of curve 5 forms the third region in the range 5 to $15\mu m$. A similar division is implied by the behavior and characteristics of the volume modes of the fitted data set, though the range of the regimes is slightly different. The measured accumulation mode exists from the lower limit of the Royco to about

0.47μm, the middle mode exists from 0.45 to 1.4μm, and the coarse particle mode is in the region 3μm to the Royco's upper limit, 5.9μm. Such a division also appears in the aerosol volume distributions presented in Patterson and Gillette (1977) and Patterson *et al.* (1980). These investigators describe a submicrometer mode composed of anthropogenic aerosols, a maritime aerosol mode centered at a radius of about 1μm, and an aerosol mode at about 3μm composed of soil particles.

The values of mode radius and standard deviation for the different volume modes have been summarized in Table 3.3. The symbol -- indicates that no value was given for this parameter. The mode radii for the accumulation and coarse particle modes appear to agree fairly well. The standard deviations of these modes for the aircraft data are, however, significantly less than those found in the data of Whitby (1978) and Patterson and Gillette (1977) and the rural model of Shettle and Fenn (1979). For the coarse mode, this may be a result of low particle counts and an incomplete sampling of the entire mode which was often measured near the upper limit of the Royco counter. Investigations of the discrepancy existing for the accumulation mode are continuing. Preliminary analysis of the submicrometer mode measured near the ground at Meppen, with a separate particle counter, show standard deviations of about the same values as those determined from the aircraft data. The mean standard deviation of the fitted middle mode approximates the value used in the maritime model of Shettle and Fenn (1979). The volume mean radius of 1μm measured by Patterson *et al.* (1980) for a Pacific marine boundary-layer aerosol is in the range of the mode radii determined from the aircraft data for the middle mode. Care must be exercised in interpreting the middle mode of the aircraft data as a marine aerosol, since the source of the aerosol is not known.

Recommendation

In future aerosol studies it is recommended that a greater effort be placed on determining the history of the air mass containing the aerosol sample. The dependencies on altitude, season, and site shown in the two tables for the different combinations of the modes could be better explained if the history of the aerosol sample were known.

Table 3.3. Summary of the Volume Mode Parameters.

Source	Accumulation $\bar{r}(\mu m)$	σ	Middle $\bar{r}(\mu m)$	σ	Coarse $\bar{r}(\mu m)$	σ
Fitch and Cress	0.25 - 0.47	0.11	0.45 - 1.4	0.3	5	0.2
Whitby (1978) average continental aerosol	0.15	0.31			3	0.33
Patterson and Gillette (1977) tropospheric aerosol with dust	0.14	0.19			2.8	0.34
Patterson *et al.* (1980) maritime aerosol	<0.5	--	1	--		
Shettle and Fenn (1979) rural model	0.19 - 0.37	0.35			5.5 - 15	0.4
maritime model			1.1 - 5.3	0.35		

The data suggest that the accumulation mode is strongly associated with anthropogenic sources of aerosol, the middle mode with a maritime environment, the coarse mode with wind blown dust, and the constant with an average background aerosol. Such a division of the aerosol size range would be of aid in predicting the optical characteristics of an aerosol.

4. SUMMARY

This Final Report under contract F19628-78-C-0200 has addressed the reduction and publication of previously unprocessed raw data gathered during the period 1970 through 1978 by the airborne instrument system and measurement program summarized in Duntley *et al.* (1978). The Aircraft Data Reduction effort, task one under this two part research contract, has concentrated on the measurements of atmospheric optical properties, primarily scattering coefficient profiles plus sky and terrain radiances, that were collected during the Winter and Summer seasons of 1978. During this interval, there were approximately 45 data flights conducted throughout western and northern Europe. The atmospheric optical data from these and other flights have been published in six of the ten OPAQUE related AFGL Technical Reports listed in Table 2.3. Over 670 aerosol size distributions covering particle radii from 0.2 to 5.9 micrometers were measured contemporaneously with the measurements of sky and terrain radiances during these flights. As noted in Table 2.3, portions of these aerosol data have also been previously reported during this contract interval.

The basic data types which have been processed and reported during this contract interval, and thus summarized and reviewed in this Final Report, fall into the following general categories: a) altitude profiles of atmospheric volume scattering coefficient, b) fixed altitude measurements of sky and terrain radiances, and c) fixed altitude measurements of aerosol size distributions.

Several general characteristics of the full 6 kilometer profiles of volume scattering coefficients can be summarized as follows. In both the Winter and Summer data sets, the Trapani profiles are clearly different from their companion profiles measured in northern Europe. In the Winter set, the Trapani profiles show significantly less low altitude structure than any of the other sets, and have a complete lack of any abrupt haze top. Similarly, the Summer Trapani profiles show little structure and additionally maintain relatively high scattering coefficient values throughout the entire 6 km altitude band. It appears that there is substantially more structural irregularity in the scattering coefficient profiles during the Winter set than during the Summer. This is particularly true for the northern European stations, Soesterberg, Meppen and Rodby.

Several illustrations of very low altitude *i.e.* ground level to 700m AGL, photopic volume scattering coefficient profiles are presented from the fifty-four profiles previously reported. The basic question addressed by these data is whether or not the scattering coefficient profile

remains reasonably constant as one approaches the surface from an altitude of several hundred meters. These data, representing all four temporal seasons, indicate that in forty-seven out of fifty-four (87%) instances, the profile is essentially constant in value within this very low altitude regime.

Sky and terrain radiance distributions selected from data measured during all five OPAQUE deployments illustrate the full gamut of meteorological conditions from clear and cloud free to fully overcast. A remarkable degree of radiance symmetry and uniformity is illustrated for the full overcast conditions. However, under less extreme coverages, a consistent pattern of well behaved radiance patterns, both as a function spectral band and of altitude, is easily recognized. One notes, that under conditions of highly variable cloud cover, the measured sky and terrain radiances tend to fluctuate both above and below the radiance distribution of a clear sky by a factor of two or more in some instances, but in general remain within about ± 50 percent of the clear sky radiance for corresponding paths of sight.

Corrective techniques developed during this contract interval have been applied to selected sub-sets of scattering coefficient and sky radiance measurements. Analysis of these data, plus additional measurements of directional scattering function at scattering angles of 30 and 150 degrees led to the conclusion that, in most cases, the measurements of the upper altitude total volume scattering coefficients were too high. The evidences are consistent in their predictions of photopic optical scattering ratios $Q(z)$ of from 1.3 to 2.6 at 6 kilometers altitude, roughly half the measured value. Additional validations of the techniques are recommended.

Measured near-sun radiances were found to be consistently too high due to off-axis stray light entering the scanner's optical system as its field of view swept through the solar disc. The implications of subsequent testing were that high altitude or clear day measurements of sky radiance within 10° of the solar disc will have stray light ratios of as much as 20 to 35, whereas low altitude near-sun measurements through more turbid atmospheres will have substantially lower stray light ratios of about 3 to 6 at the same angular distance from the disc. There were no detectable stray light influences upon measurements made beyond 25° from the disc under any of the conditions tested.

More than 670 aerosol size distributions covering particle radii for 0.2 to $5.9\mu m$ were collected contemporaneously with the measurements of sky and terrain radiances. The measured volume (mode) - size distributions were characterized by three additive log-normal distributions, one for each of the three volume modes observed in the data. The behavior of the modal parameters for each of the three volume modes and of the modes as a function of altitude, humidity, season, and geographic site of measurement were examined resulting in the following conclusions:

1. The accumulation mode is almost always confined to the mixing layer. The mode radius $\bar{r}$ ranges from 0.25 to $0.47\mu m$ and its standard deviation σ is a constant of approximate value 0.11. The mode radius is a linear function of the value $dV/d\log r$ at the $\bar{r}$. The accumulation mode is the most prevalent volume mode occurring as the only mode more often in the summer season than in the winter season data. It shows no significant dependence on relative humidity. The accumulation mode appears more frequently in the data collected at the northern stations than the southern stations.
2. The middle mode occurs only within the mixing layer, most often in the lower half of the layer. The mode radius ranges from 0.45 to $1.4\mu m$ and its standard deviation appears to be a constant of value 0.3. The middle mode appears more often in the winter than in the summer season data and more often when the relative humidity is greater than 70% than when it is less than 70%.
3. The coarse particle mode can exist above or within the mixing layer. The mean values of σ and $\bar{r}$ for this mode are 0.2 and $5\mu m$, respectively. The coarse mode shows no preference toward season, but appears more often in the low, less than 70%, humidity data. The mode appears more often in the data collected from the southern most sites.
4. At altitudes above the mixing layer the volume display typically shows no discernible modes and is well fit by a constant.
5. The data and comparisons with aerosol models imply that the volume modes are associated with specific aerosol sources and, therefore, with the history of the airmass in which the aerosol sample was measured.

5. ACKNOWLEDGEMENTS

This final report has been prepared for the Air Force Geophysics Laboratory under Contract No. F19628-78-C-0200. The authors wish to thank the members of the Visibility Laboratory technical staff for their assistance in preparing these data, and the members of the Atmospheric Optics Branch of the Air Force Geophysics Laboratory for their technical support and council.

We particularly thank Mr. Nils R. Persson, Jr., our senior computer specialist, Ms. Alicia G. Hill and Mr. John C. Brown, our specialists in computer assisted document preparation, for many diligent hours devoted to generating this final copy.

The corrective techniques and supporting analyses of Section 2 represent major contributions by Ms. Jacqueline I. Gordon and Mr. Wayne S. Hering.

Special thanks to Lt.Col. Ted S. Cress for his many thoughtful and provacative contributions to the analysis of the aerosol size distribution data.

6. REFERENCES

Aitchison, J. and J. A. C. Brown, *The Log-Normal Distribution,* (Cambridge University Press, New York, 1957).

Bevington, Philip R., "*Data Reduction and Error Analysis for the Physical Sciences*" (McGraw-Hill Book Co., New York, 1969).

Blifford, Jr., I. H. and L. D. Ringer, "The Size and Number Distribution of Aerosols in the Continental Troposphere", J. Atmos. Sci., **26**, 716-726 (1969).

Cress, T. S., "Airborne Measurements of Aerosol Size Distributions Over Northern Europe, Vol. 1", AFGL-TR-80-0178, Air Force Geophysics Laboratory, Hanscom AFB, Massachusetts (1980).

Davies, C. N., "Size Distribution of Atmospheric Particles", Aerosol Sci., **5**, 293-300 (1974).

Deirmendjian, D., *Electromagnetic Scattering on Spherical Polydispersions* (American Elsevier, New York, 1969).

Duntley, S. Q., R. W. Johnson and J. I. Gordon, "Airborne Measurements of Optical Atmospheric Properties, Summary and Review II", University of California, San Diego, Scripps Institution of Oceanography, Visibility Laboratory, SIO Ref. 75-26, AFCRL-TR-75-0457, NTIS No. ADA 022 675 (1975).

Duntley, S. Q. R. W. Johnson, and J. I. Gordon, "Airborne Measurements of Atmospheric Volume Scattering Coefficients in Northern Europe, Spring 1976", University of California, San Diego, Scripps Institution of Oceanography, Visibility Laboratory, SIO Ref. 77-8, AFGL-TR-77-0078, NTIS No. ADA 046 290 (1977).

Duntley, S. Q., R. W. Johnson, J. I. Gordon, "Airborne Measurements of Optical Atmospheric Properties, Summary and Review III", University of California, San Diego, Scripps Institution of Oceanography, Visibility Laboratory, SIO Ref. 79-5, AFGL-TR-78-0286, NTIS No. ADA 073 121 (1978).

Fitch, B. W. and T. S. Cress, "Measurements of Aerosol Size Distributions in the Lower Troposphere Over Northern Europe", J. Appl. Meteor., **20**, 1119-1128 (1981).

Hering, W. S., "An Operational Technique for Estimating Visible Spectrum Contrast Transmittance", University of California, San Diego, Scripps Institution of Oceanography, Visibility Laboratory, SIO Ref. 82-1, AFGL-TR-81-0198 (1981).

Hughes, H. G. and J. H. Richter, "Extinction Coefficients Calculated from Aerosol Size Distributions Measured in a Marine Environment", Optical Engineering, **19**, 616-620 (1980).

Irvine, W.M., "Multiple Scattering by Large Particles II Optically Thick Layers", Astrophys. J., **152**, 823-834 (1968).

Jaenicke, R. and C. N. Davies, "The Mathematical Expression of the Size Distribution of Atmospheric Aerosols", J. Aerosol Sci., **7**, 255-259 (1976).

Johnson, R. W., and J. I. Gordon, "Airborne Measurements of Atmospheric Volume Scattering Coefficients in Northern Europe, Winter 1978", University of California, San Diego, Scripps Institution of Oceanography, Visibility Laboratory, SIO Ref. 79-25, AFGL-TR-79-0159, NTIS No. ADA 082 044 (1979).

Johnson, R. W. and J. I. Gordon, "Airborne Measurements of Atmospheric Volume / Scattering Coefficients in Northern Europe, Summer 1978", University of California, San Diego, Scripps Institution of Oceanography, Visibility Laboratory, SIO Ref. 80-20, AFGL-TR-80-0207, NTIS No. ADA 097 134 (1980).

Johnson, R. W. and W. S. Hering, "An Analysis of Natural Variations in Measured European Sky and Terrain Radiances", University of California, San Diego, Scripps Institution of Oceanography, Visibility Laboratory, SIO Ref. 82-00, AFGL-TR-81-0317 (1981).

Johnson, R. W., "Airborne Measurements of European Sky and Terrain Radiances", University of California, San Diego, Scripps Institution of Oceanography, Visibility Laboratory, SIO Ref. 81-00, AFGL-TR-81-0275 (1981).

Johnson, R. W., "Winter and Summer Measurements of European Very Low Altitude Volume Scattering Coefficients", University of California, San Diego, Scripps Institution of Oceanography, Visibility Laboratory, SIO Ref. 81-26, AFGL-TR-81-0154, NTIS No. ADA 106 363 (1981).

Johnson, R. W., "Spring and Fall Measurements of European Very Low Altitude Volume Scattering Coefficients", University of California, San Diego, Scripps Institution of Oceanography, Visibility Laboratory, SIO Ref. 81-33, AFGL-TR-81-0237, NTIS No. ADA 108 879 (1981).

Junge, C. E., *Air Chemistry and Radioactivity,* (Academic Press, New York 1963).

Junge, C. and R. Jaenicke, "New Results in Background Aerosols Studies from the Atlantic Expedition of the R. V. Meteor, Spring 1969", Aerosol Sci., **2**, 305-314 (1971).

Kushpil', V.I., and L.F. Petrova, "Determination of the Atmospheric Transmittance from Sky Brightness Distribution", Optical Technology **38**, No. 4, 191-193 (1971).

Livshits, G. Sh. and V.E. Pavlov, "Atmospheric Transmittance and the Interrelationships of Certain Optical Parameters", in *Atmospheric Optics,* Nikolai B. Divari, Ed., translated by S.B. Dresner, (Plenum Publishing Corp., New York, 1970), pp. 53-56.

Patterson, E.M., C.S. Kiang, A.C. Delany, A.F. Wartburg, A.C.D. Leslie, and B.J. Hulbert, "Global Measurements of Aerosols in Remote Continental and Marine Regions: Concentrations, Size Distributions, and Optical Properties", J. Geophys. Res., **85**, 7361-7376 (1980).

Patterson, E.M. and D.A. Gillette, "Commonalities in Measured Size Distributions for Aerosols Having a Soil-Derived Component", J. Geophys. Res., **82**, 2074-2082 (1977).

Quenzel, H., "Influence of Reflective Index on the Accuracy of Size Determination of Aerosol Particles with Light-Scattering Aerosol Counters", Appl. Opt., **8**, 165-169 (1969).

Raabe, Otto G., "Particle Size Analysis Utilizing Grouped Data and the Log-Normal Distribution", Aerosol Sci., **2**, 289-303 (1971).

Shettle, E. P., Comment on "Atmospheric Aerosol Size Spectra, Rapid Concentration Fluctuations and Bimodality", by T. E. Graedel and J. P. Franey, J. Geophys. Res., **80**, 3050-3051 (1975).

Shettle, E. P. and R. W. Fenn, "Models for the Aerosols of the Lower Atmosphere and the Effects of Humidity Variations on their Optical Properties", AFGL-TR-79-0214, Air Force Geophysics Laboratory, Hanscom AFB, Massachusetts (1979).

U.S. Standard Atmosphere Supplements, U.S. Government Printing Office, Washington, D.C. 20402 (1966).

Wells, W. C., G. Gal, and M. W. Munn, "Aerosol Distributions in Maritime Air and Predicted Scattering Coefficients in the Infrared", Appl. Opt., **16**, 654-659 (1977).

Whitby, K. T., "The Physical Characteristics of Sulfur Aerosols", Atmos. Env., **12**, 135-159 (1978).

Whitby, K. T., R. B. Husar, and B. Y. H. Liu, "The Aerosol Size Distribution of Los Angeles Smog", J. Colloid and Interface Sco., **39**, 177-204. Reprinted in *Aerosols and Atmos. Chem.*, G. M. Hidy, Ed. (Academic Press, New York, 1972) pp. 237-264.

APPENDIX A

VISIBILITY LABORATORY CONTRACTS AND RELATED PUBLICATIONS

Previous Related Contracts:
F19628-73-C-0013, F19628-76-C-0004

PUBLICATIONS:

Duntley, S. Q., R. W. Johnson, J. I. Gordon, and A. R. Boileau, "Airborne Measurements of Optical Atmospheric Properties at Night", University of California, San Diego, Scripps Institution of Oceanography, Visibility Laboratory, SIO Ref. 70-7, AFCRL-70-0137, NTIS No. AD 870 734 (1970).

Duntley, S. Q., R. W. Johnson, and J. I. Gordon, "Airborne Measurements of Optical Atmospheric Properties in Southern Germany", University of California, San Diego, Scripps Institution of Oceanography, Visibility Laboratory, SIO Ref. 72-64, AFCRL-72-0255, NTIS No. AD 747 490 (1972a).

Duntley, S. Q., R. W. Johnson, and J. I. Gordon, "Airborne and Ground-Based Measurements of Optical Atmospheric Properties in Central New Mexico", University of California, San Diego, Scripps Institution of Oceanography, Visibility Laboratory, SIO Ref. 72-71, AFCRL-72-0461, NTIS No. AD 751 936 (1972b).

Duntley, S. Q., R. W. Johnson, and J. I. Gordon, "Airborne Measurements of Optical Atmospheric Properties, Summary and Review", University of California, San Diego, Scripps Institution of Oceanography, Visibility Laboratory, SIO Ref. 72-82, AFCRL-72-0593, NTIS No. AD 754 898 (1972c).

Duntley, S. Q., R. W. Johnson, and J. I. Gordon, "Airborne Measurements of Optical Atmospheric Properties in Southern Illinois", University of California, San Diego, Scripps Institution of Oceanography, Visibility Laboratory, SIO Ref. 73-24, AFCRL-TR-73-0422, NTIS No. AD 774 597 (1973).

Duntley, S. Q., R. W. Johnson, and J. I. Gordon, "Airborne and Ground-Based Measurements of Optical Atmospheric Properties in Southern Illinois", University of California, San Diego, Scripps Institution of Oceanography, Visibility Laboratory, SIO Ref. 74-25, AFCRL-TR-74-0298, NTIS No. ADA 013 164 (1974).

Duntley, S. Q., R. W. Johnson, and J. I. Gordon, "Airborne Measurements of Optical Atmospheric Properties in Western Washington", University of California, San Diego, Scripps Institution of Oceanography, Visibility Laboratory, SIO Ref. 75-24, AFCRL-TR-75-0414, NTIS No. ADA 026 036 (1975).

Duntley, S. Q., R. W. Johnson, and J. I. Gordon, "Airborne Measurements of Optical Atmospheric Properties, Summary and Review II", University of California, San Diego, Scripps Institution of Oceanography, Visibility Laboratory, SIO Ref. 75-26, AFCRL-TR-75-0457, NTIS No. ADA 022 675 (1975).

Duntley, S. Q., R. W. Johnson, and J. I. Gordon, "Airborne Measurements of Optical Atmospheric Properties in Northern Germany", University of California, San Diego, Scripps Institution of Oceanography, Visibility Laboratory, SIO Ref. 76-17, AFGL-TR-76-0188, NTIS No. ADA 035 571 (1976).

Duntley, S. Q., R. W. Johnson, and J. I. Gordon, "Airborne Measurements of Atmospheric Volume Scattering Coefficients in Northern Europe, Spring 1976", University of California, San Diego, Scripps Institution of Oceanography, Visibility Laboratory, SIO Ref. 77-8, AFGL-TR-77-0078, NTIS No. ADA 046 290 (1977).

Duntley, S. Q., R. W. Johnson, and J. I. Gordon, "Airborne Measurements of Atmospheric Volume Scattering Coefficients in Northern Europe, Fall 1976", University of California, San Diego, Scripps Institution of Oceanography, Visibility Laboratory, SIO Ref. 78-3, AFGL-TR-77-0239, NTIS No. ADA 057 144 (1978a).

Duntley, S. Q., R. W. Johnson, and J. I. Gordon, "Airborne Measurements of Atmospheric Volume Scattering Coefficients in Northern Europe, Summer 1977", University of California, San Diego, Scripps Institution of Oceanography, Visibility Laboratory, SIO Ref. 78-28, AFGL-TR-78-0168, NTIS No. ADA 068 611 (1978b).

Duntley, S. Q., R. W. Johnson, and J. I. Gordon, "Airborne Measurements of Optical Atmospheric Properties, Summary and Review III", University of California, San Diego, Scripps Institution of Oceanography, Visibility Laboratory, SIO Ref. 79-5, AFGL-TR-78-0286, NTIS No. ADA 073 121 (1978c).

Fitch, B. W., "Measurements of Aerosol Size Distribution in the Lower Troposphere over Northern Europe", University of California, San Diego, Scripps Institution of Oceanography, Visibility Laboratory, SIO Ref. 81-18, AFGL-TR-80-0192 (1981).

Gordon, J. I., J. L. Harris, Sr., and S. Q. Duntley, "Measuring Earth-to-Space Contrast Transmittance from Ground Stations", Appl. Opt. **12**, 1317-1324 (1973).

Gordon, J. I., C. F. Edgerton, and S. Q. Duntley, "Signal-Light Nomogram", J. Opt. Soc. Am. **65**, 111-118 (1975).

Gordon, J. I., "Daytime Visibility, A Conceptual Review", University of California, San Diego, Scripps Institution of Oceanography, Visibility Laboratory, SIO Ref. 80-1, AFGL-TR-79-0257, NTIS No. ADA 085 451 (1979).

Hering, W. S., "An Operational Technique for Estimating Visible Spectrum Contrast Transmittance", University of California, San Diego, Scripps Institution of Oceanography, Visibility Laboratory, SIO Ref. 82-1 AFGL-TR-81-0198 (1981).

Johnson, R. W., and J. I. Gordon. "Airborne Measurements of Atmospheric Volume Scattering Coefficients in Northern Europe, Winter 1978", University of California, San Diego, Scripps Institution of Oceanography, Visibility Laboratory, SIO Ref. 79-25, AFGL-TR-79-0159, NTIS No. ADA 082 044 (1979).

Johnson, R. W., W. S. Hering, J. I. Gordon, B. W. Fitch, and J. S. Shields, "Preliminary Analysis & Modelling Based Upon Project OPAQUE Profile and Surface Data", University of California, San Diego, Scripps Institution of Oceanography, Visibility Laboratory, SIO Ref. 80-5, AFGL-TR-79-0285, NTIS No. ADB 085 451L (1979).

Johnson, R. W. and J. I. Gordon, "Airborne Measurements of Atmospheric Volume Scattering Coefficients in Northern Europe, Summer 1978", University of California, San Diego, Scripps Institution of Oceanography, Visibility Laboratory, SIO Ref. 80-20, AFGL-TR-80-0207, NTIS No. ADA 097 134 (1980).

Johnson, R. W. and W. S. Hering, "An Analysis of Natural Variations in Measured European Sky and Terrain Radiances", University of California, San Diego, Scripps Institution of Oceanography, Visibility Laboratory, SIO Ref. 82-6, AFGL-TR-81-0317 (1981).

Johnson, R. W., "Winter and Summer Measurements of European Very Low Altitude Volume Scattering Coefficients," University of California, San Diego, Scripps Institution of Oceanography, SIO Ref. 81-26, AFGL-TR-81-0154, NTIS No. ADA 106 363 (1981a).

Johnson, R. W., "Spring and Fall Measurements of European Very Low Altitude Volume Scattering Coefficients", University of California, San Diego, Scripps Institution of Oceanography, Visibility Laboratory, SIO Ref. 81-33, AFGL-TR-81-0237 (1981b).

Johnson, R. W., "Daytime Visibility and Nephelometer Measurements Related to its Determination", Atmospheric Environment, **15**, 10/11, 1835 (1981c).

Johnson, R. W., "Airborne Measurements of European Sky and Terrain Radiances", University of California, San Diego, Scripps Institution of Oceanography, Visibility Laboratory, SIO Ref. 82-2, AFGL-TR-81-0275 (1981d).

Shields, J. S., "An Analysis of Infrared and Visible Atmospheric Extinction Coefficient Measurements in Europe", University of California, San Diego, Scripps Institution of Oceanography, Visibility Laboratory, SIO Ref. 82-4, AFGL-TR-81-0251 (1981).

Atmospheric Environment Vol. 15, No. 10/11, pp. 1835–1845, 1981
Printed in Great Britain.

0004-6981/81/101835-11 $02.00/0

DAYTIME VISIBILITY AND NEPHELOMETER MEASUREMENTS RELATED TO ITS DETERMINATION*

RICHARD W. JOHNSON

Visibility Laboratory, Scripps Institution of Oceanography, University of California, San Diego, La Jolla, California 92093, U.S.A.

(*First received* 2 *September* 1980 *and in final form* 26 *January* 1981)

Abstract—The ability of a human observer to perform tasks involving visual search and the determination of visual ranges (i.e., visibilities), is a commonly recognized skill that is presently under increasing competition from a variety of sophisticated electro-optical systems. The paper reviews a few of the pertinent psychophysical characteristics related to the human observer's performance, how they are related to some instrumentally measured quantities, and two of the more commonly encountered sources of error in visual determinations of visibility. Comparisons between several observer and instrumental determinations illustrate the link between the two experimental regimes and introduce some appropriate specialized data obtained with an airborne nephelometer. Since the determination of visibility is the simpler special case of determining horizontal path contrast transmittance, several characteristics of the nephelometer data which influence its use in the more general determination of slant path contrast transmittance are illustrated. In this context, the implication of these data in ones ability to accurately model atmospheric influences upon contrast transmittance is introduced. The basic conclusions to be drawn from this paper are twofold. First, that although human visual performance is a complex psychophysical task, there is little doubt that for visibility determinations it can be adequately related to instrumental measurements of atmospheric volume scattering coefficient and second, that a reliable specification of the directional scattering properties of the atmospheric aerosol can be reasonably deduced from this measurement of total volume scattering coefficient alone.

1. INTRODUCTION

Since visual estimates of daytime visibility are made and recorded routinely by professionals and amateurs for a variety of purposes, it is a term one might expect to be fully and clearly understood by all. Unfortunately, this is not always the case, even among experienced personnel working in the field of atmospheric sciences. Thus, even though the modern literature on Visibility is rich, extending from the 179 entry annotated bibliography of Grimes (1969) through an additional 700 computerized references listed at the Visibility Laboratory, it was decided that yet another note might be helpful if it could provide a reasonably concise juxtaposition of the conceptual variables defining the psychophysical aspects implied in the term "visibility", with the physical characteristics of some equivalent instrumental measurements.

This note then will first present a brief review of the cogent conceptual variables related to visual determinations and their relationship to instrumental determinations of visibility. It will then illustrate a series of nephelometer measurements which are commonly associated with instrumental determinations of visibility, but which in this case can be extended to address the more general subject of determining slant path directional contrast transmittance, and the modelling of the atmospheric properties most influencing these determinations.

* Paper presented at the Symposium on Plumes and Visibility: Measurements and Model Components. Grand Canyon, Arizona, U.S.A. 10–14 November 1980.

2. DAYTIME VISIBILITY FROM VISUAL OBSERVATIONS

The determination of a human observer's capability to discern barely perceptible changes in the apparent luminance difference between an object and its surrounding background (i.e. the luminance contrast threshold), has been a fruitful field for vision research for many years. An extensive experimental effort was initiated at the Tiffany Foundation in New York during the early years of World War II, the data for which were tabulated by Duntley (1946) and the experimental results for which were discussed by Blackwell (1946). An important point well illustrated by these data is that the contrast threshold for the daylight adapted human eye changes very little as a function of background luminance, but is a strong function of the angular subtense of the target and of the time spent looking at the target.

To illustrate this rather fundamental psychophysical relationship, we have generated the composite plots shown in Fig. 1. In this figure, the contrast values shown along the horizontal axis are defined by Equation (1), and in each case have been adjusted from the experimental liminal values (i.e., 50% prob. of detection) to values appropriate for confident sighting (99% confidence). The correction factors are from Taylor (1964). Equation (1) thus represents the most fundamental relationship involved in any visual search scenario.

$$C_r = \frac{{}_tB_r - {}_bB_r}{{}_bB_r} = \frac{{}_tB_r}{{}_bB_r} - 1, \qquad (1)$$

APPENDIX B

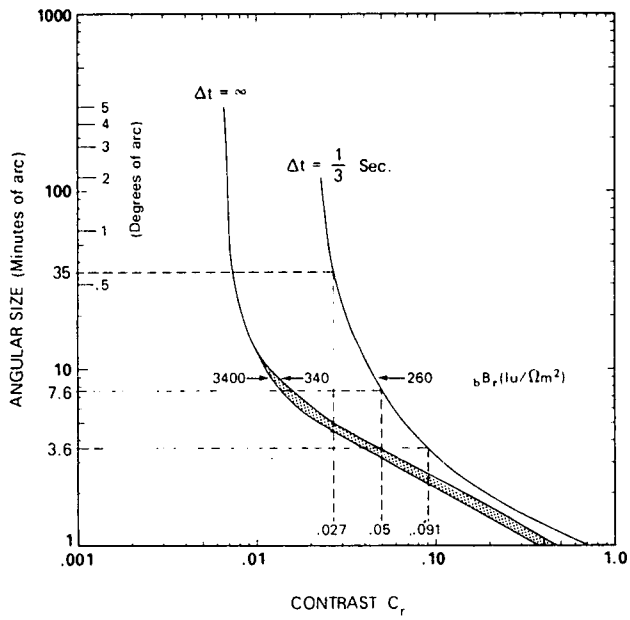

Fig. 1. Angular size as a function of contrast for a 99% probability (confidence) and a lack of knowledge of target position of ±4 deg. or more (Gordon, 1979).

where C_r represents the apparent contrast, at distance r, of the visual target t against its background b; ${}_tB_r$ represents the apparent luminance of the visual target as seen from distance r; and ${}_bB_r$ represents the apparent luminance of the background against which the target is viewed as seen from distance r.

In Fig. 1, the curves to the left, labeled $\Delta t = \infty$ are from the Tiffany data for long duration viewing, where the viewing times Δt were 24 s and longer. The curve to the right, labeled $\Delta t = 1/3$ s is from Taylor (1964). As one can note from these graphical displays, the Tiffany long duration data indicate via the slowly spreading shaded area, that large changes in the luminance of the daylight horizon background (i.e. 3400 to 340 lu Ω^{-1} m^{-2}) make little difference to the discernible threshold contrast C_r. However, as illustrated by the horizontal offset between the $\Delta t = \infty$ and the $\Delta t = 1/3$ s plots, the time used in viewing the object does have an appreciable influence on the contrast threshold, particularly for targets at the larger angular sizes.

These data also clearly illustrate the underlying rationale for the WMO (1971) recommendation: "In order that daytime visibility measurements should be representative, they should be made using objects subtending an angle of not less than 0.5 degrees at the observer's eye." The 0.5 deg angular size (e.g., equivalent to the solar or lunar disc) and the commonly recommended threshold contrast of 0.025 are clearly related through the Taylor $\Delta t = 1/3$ s data.

2.1. *Historical visual–instrumental comparisons*

Armed with the *a priori* knowledge that target size, descernible threshold contrast, and observer glimpse times are all interrelated, and oft times less than clearly defined, one might fairly ask: "What threshold contrast is actually limiting the determination of the visibility when an observer just sights a particular target?"

Fortunately, there have been a good number of well done experiments wherein the visibility range was determined visually at the same time as the degradation of the atmosphere was measured by physical instruments. If one makes a few assumptions about the performance of the man and the machine in these experiments, some encouragingly consistent results emerge. Most caveats regarding these assumptions are discussed at length by others as recently as Malm (1979) and need not be pursued further here. Thus, if one assumes that the visual determinations were made using a truly black target having an inherent contrast of -1 against a clear, cloud-free horizon; and if one also assumes that the machine measures an attenuation coefficient α which is representative of the average coefficient along the path of sight, then the apparent contrast is given by

$$|C_r| = T_r = e^{-\alpha r}, \tag{2}$$

where T_r is the transmittance of the path of sight r along which the determination of C_r is accomplished.

In Equation (2), one notes that the visibility range r is defined once a threshold contrast, C_r is specified. It is through this expression that the performance link between man and machine can be evaluated, and in fact answer the initially posed question regarding the actual limiting threshold contrasts.

The experimental works of Douglas and Young (1945), Duntley (1948), Middleton (1952), Horvath and Noll (1969) and Hering *et al.* (1971) all relate to

determining the efficacy of the relationships specified in Equation (2). The data in general are all similar in nature to those of Hering et al. (1971) illustrated in Fig. 2, which compare extinction coefficients determined from transmissometer measurements with visibilities determined by human observers.

If there is a reasonably constant threshold contrast $|C_r|$, then data of this sort can be expected to fall on a straight line when plotted in logarithmic formats which reflect Equation (2) or its simplified equivalent

$$-\ln|C_r| = \alpha r, \tag{3}$$

which is merely another way of saying that if the threshold contrast is constant, then the product αr, the threshold sighting range times the attenuation coefficient, is also constant.

In Fig. 2, the straight lines drawn through the data for comparative purposes represent the conditions which would be expected to exist for constant threshold contrasts of 0.02 and 0.05.

There is a satisfying thread of constancy running through these experimental works which illustrates the reasonableness of expecting a typical threshold contrast for human daylight observations to exist and that it be analytically relatable to instrumental measurements.

Early workers in the field of visual search recommended the use of visibility targets at least 0.5 deg in size, and the corresponding use of a threshold contrast of 0.025 which would thus yield the attenuation coefficient-sighting range product αr of 3.7. However, if one chooses to adopt a threshold contrast of 0.05, then the corresponding αr product becomes 3.0 and additional experimental consistencies emerge. Accepting a variability of $\pm 20\%$ in visually determined sighting ranges results in

$$\alpha r = 3.0 \pm 0.6, \tag{4}$$

with a corresponding variability in threshold contrast of 0.027 to 0.091. This threshold relationship is illustrated on Fig. 1 by the broken lines connecting the horizontal and vertical axes via the $\Delta t = 1/3$ s curve. From this plot it can be seen that threshold angular sizes might be expected to vary between 3.6 and 35.0 min of arc.

An examination of the experimental data referenced in the preceeding paragraphs with the visibility specification implied in Equation (4) in mind, indicates that by far the bulk of these experimental data fall within the bounds of this specification. In a way, this is a remarkable consistency considering the variability in the mechanics of the various determinations, and the conditions under which they were conducted.

It is thus a well supported contention from both psychophysical and physical measurement considerations, that *visibility* can reasonably be defined as the distance that a black target of suitable dimensions can be seen against the cloudless horizon sky, and it is related to the attenuation coefficient with an accuracy of $\pm 20\%$ by the relationship indicated in Equation (4). There are, however, specific penalties involved if one chooses to ignore the caveats associated with visual determinations of horizontal visibility.

2.2. *Non-standard effects*

2.2.1. *Non-black targets.* It is of interest to note the influence on visibility estimates induced through the

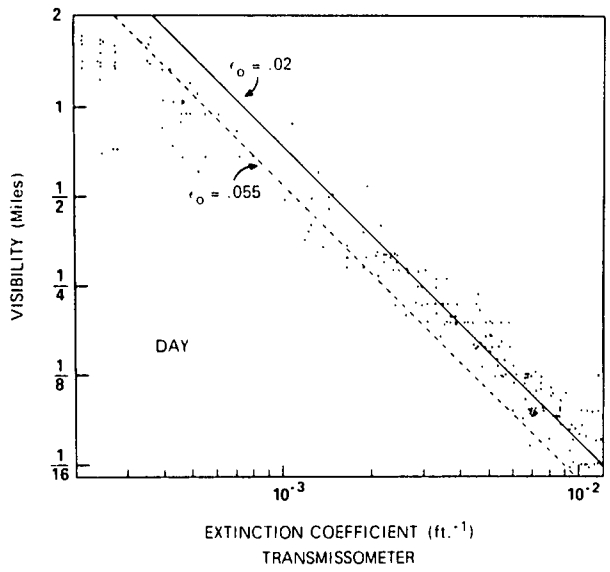

Fig. 2. Comparison between transmissometer measurements and human visibility observations during the daytime, $\varepsilon_0 = C_r$ (Hering et al., 1971).

use of either non-black targets, or backgrounds other than the horizon sky. Derivations to conveniently evaluate these influences are given in Gordon (1979) from which several summarizing illustrations are reproduced herein. As a convenience, we have chosen to use the reflectance format for most variables, hence inherent contrast is re-defined as a function of the target to background reflectance ratio,

$$C_0 = \frac{{}_tR_0}{{}_bR_0} - 1, \tag{5}$$

where C_0 represents the preceived contrast at distance zero from the visual target; and ${}_tR_0$ and ${}_bR_0$ represent the respective target and background reflectances. A similar definition is of course appropriate for the apparent contrast, C_r.

The effect on visual range determinations of using non-black targets is illustrated in Fig. 3. In this plot, the horizontal axis is conveniently marked in both inherent reflectance ratio and the equivalent inherent contrast. The vertical axis is marked as Relative Visual Range, which is defined as the ratio of the visual range one would determine observing a non-black target, to that one would determine if observing an ideal black target having the optimum inherent contrast of minus one.

It is apparent that for the relative visual range determination to be within 5% of the ideal, negative contrast can range between -1 and -0.86. However, for varying positive contrasts, the relative visual range changes quite rapidly, and the 5% variance from ideal is contained in a very narrow band between $+1.9$ and $+2.2$.

2.2.2. *Non-horizon sky.* For visual range determinations using non-horizon sky backgrounds, Middleton (1952) presented a series of expressions for comparing the relative visual range of a black object as seen against a black background with that of the black object as seen against the horizon sky. His analysis indicated that for a threshold contrast of 0.02, an acceptably accurate determination of visual range would result if the black background was at least 1.5 times as distant from the observer as was the object. Since this distance ratio is broadly recognized and is referred to as a general rule of thumb by the WMO (1971), it is appropriate at this point to enlarge slightly upon the previous references.

If one imagines the black object and its black background initially at the same distance from the observer, then it is intuitively clear and analytically correct, that in this orientation there is zero contrast between them. However, if one now begins to move the background progressively farther and farther away, the additional path radiance generated in the lengthening observer to background path will begin to develop a difference in apparent luminance between the two black surfaces. As the background distance lengthens, the apparent contrast between the object and background will increase until at some point it reaches the observers threshold contrast. When the background has reached this point, the determination of the black objects visual range will be the same as if it had been determined against the horizon sky.

In her derivations for non-standard effects, Gordon (1979) has extended this general class of analysis beyond the example of Middleton to include a selection of backgrounds other than the black, and to establish the relative visual ranges appropriate for a threshold contrast of 0.05. A key parameter in her evaluation is the ratio between the background reflectance and the equilibrium reflectance ${}_bR_0/R_q$. The equilibrium reflectance R_q is related to the equilibrium radiance N_q, i.e., the radiance of the clear horizon sky, Duntley (1948), as expressed in Equation (6).

$$R_q(0, 90°, \phi) = \frac{N_q(0, 90°, \phi)\pi}{H(0, 90°, \phi + 180°)} \tag{6}$$

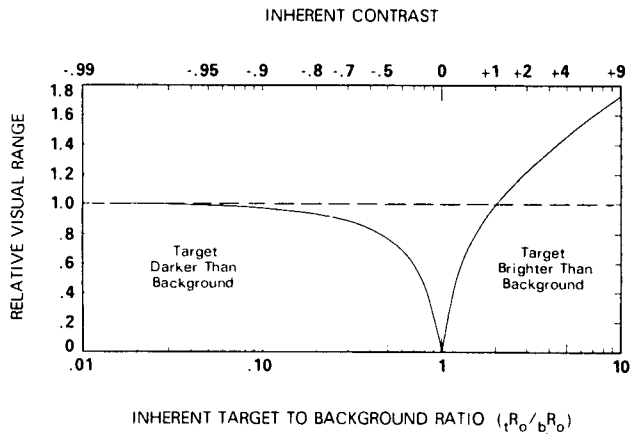

Fig. 3. Relative visual range as a function of inherent contrast and inherent target to background reflectance ratio for a contrast threshold of 0.05.

where $N_q(0, 90°, \phi)$ represents the clear horizon sky radiance as viewed at zero altitude in the direction ϕ from the sun; $H(0, 90°, \phi + 180°)$ represents the 2π irradiance falling upon a vertically oriented flat plate collector whose normal is directed in azimuth toward $\phi + 180°$; and where in all cases, the parenthetical notations denote the altitude, zenith angle and azimuth angles of the measured path of sight.

As can be seen in Fig. 4 which has been derived from the data of Gordon (1979), the use of non-black backgrounds which have reflectances less than equilibrium (${}_bR_0/R_q < 1$) at the same relative distance beyond the target yield relative visual ranges even closer to one than does the use of black background. For backgrounds brighten than equilibrium (${}_bR_0/R_q > 1$), such as a bright cloud, it is a different matter. With the use of these bright backgrounds it is necessary to have the background approximately twice as distant as the target in order for the relative visual range to become reasonably accurate.

2.2.3. *Non-horizontal paths of sight.* As one departs from the special case of determining contrast transmittances along horizontal paths through homogeneous atmospheres to the more general case of slant path transmittances, additional complexities emerge. One must now consider the variations in attenuation coefficient α as a function of altitude along the inclined path, as well as the directional scattering properties of the aerosol through which the determination is to be made. It is at this point that instrumental determinations become the preferred vehicle since they can provide this additional characterization of the atmospheric condition in a manner superior to attempts by visual observation. Experimental measurements of the sort required for these slant path determinations are presented in the following section.

3. PHYSICAL MEASUREMENTS

The direct physical measurement of air clarity in a manner appropriate for realistic comparison with determinations made by human observers has long been, and still is an endeavor spiced with gentle but lively controversy. Of the many techniques, the most common are those related to the measurement of luminance transmittance over some specified path length, the measurement of the point function attenuation or scattering coefficient, or the measurement of the apparent contrast of distant targets. In each case, the particular procedure will possess inherent shortcomings as discussed in Malm (1979), and may or may not relate well to the total human perception of visual stimuli as discussed in Malm *et al.* (1980).

Although a measured value of visible spectrum atmospheric scattering coefficient is often used with Equation (4) for the determination of daytime visibility, if one is addressing the more general case of atmospheric slant path contrast transmittance, more information is required. One must obtain a specification of both the directional scattering properties of the atmospheric aerosols, and their vertical and horizontal distribution. A multi-channel nephelometer has been used by the Visibility Laboratory to document these specific atmospheric properties.

3.1. *Airborne nephelometer design*

There are a variety of electro-optical devices designed to measure the energy scattered from an illuminated

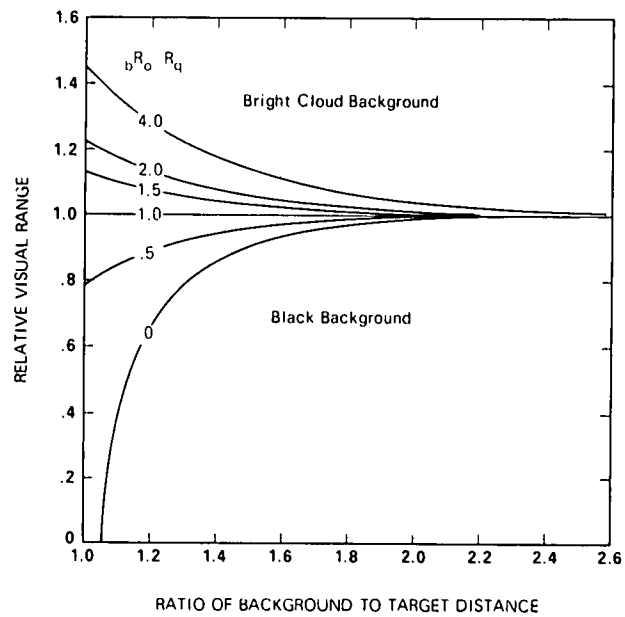

Fig. 4. Relative visual ranges for black targets viewed against backgrounds other than clear horizon sky (threshold contrast = 0.05).

volume of aerosol that are calibrated in terms of *visibility*. The EG&G Forward Scatter Visibility Meter described in Hering *et al.* (1971) is one example. Integrating nephelometers similar to those discussed in Charlson *et al.* (1967) are additional examples of devices based upon one or the other of the two techniques described by Beuttell and Brewer (1949). In all cases, these scattering meters utilize the relationship

$$s(z) = \int_{4\pi} \sigma(z, \beta)\, d\Omega, \tag{7}$$

where $\sigma(z, \beta)$ is the volume scattering function at scattering angle β and z is an altitude parameter.

Both of the procedures described by Beuttell and Brewer (1949) perform the integration of Equation (7) optically over various fractions of the 4π solid angle so as to include measurements over as broad a range of scattering angles as possible. Fundamentally the two instrumental procedures are optical inverses of one another. The first uses a diffusely emitting light source to illuminate a sample volume of aerosol which is then observed via a small field telescope assembly as in the work of Crosby and Koerber (1963), Charlson *et al.* (1967) and Horvath and Noll (1969). The second reverses the optical collector–emitter relationship by using a well collimated projector as the illuminating source and a cosine corrected irradiometer to observe the scattered flux. This second design has been used by Duntley *et al.* (1970, 1978).

The Visibility Laboratory nephelometer functionally illustrated in Fig. 5, is unique in several design aspects which make it particularly attractive experimental tool. First, the optical system used a cylindrically limited projector beam, stopped to provide a rectangular beam cross section which provides good geometrical definition of the illuminated volume. The observed scattering volume is approximately 5 cm × 9 cm in cross section, and 107 cm in length for a total sample volume of 4815 cm^3. Second, the detector assembly's primary optical channel uses a cosine corrected and mechanically shielded irradiometer head which performs the integration of Equation (7) over all scattering angles between 5 and 172° minimizing truncation losses of the sort discussed in Fitzgerald (1977), Rabinoff and Herman (1973) and Ensor and Waggoner (1970). Third, the detector assembly's secondary optical channels measure relatively narrow angle, i.e., 2° field of view, directional scattering at both 30 and 150° which allows the determination of a forward to backward scattering ratio that can be used to more thoroughly characterize the sample aerosol. Fourth, the device is multi-spectral within the visible spectrum. Thus visible spectrum blue-red scattering ratios in addition to photopically corrected measurements can be accomplished. And fifth, the entire device is designed to operate as a ratio measuring system which tends to minimize calibration errors and stability problems.

The calibration constants for the device relate the ratio of the flux scattered from the sample aerosol to the flux reflected from a calibrated reflective plaque with the physical properties of the overall optical system, and the most probable shape of the scattering function associated with the sample aerosol. Constants have been derived for scattering functions ranging

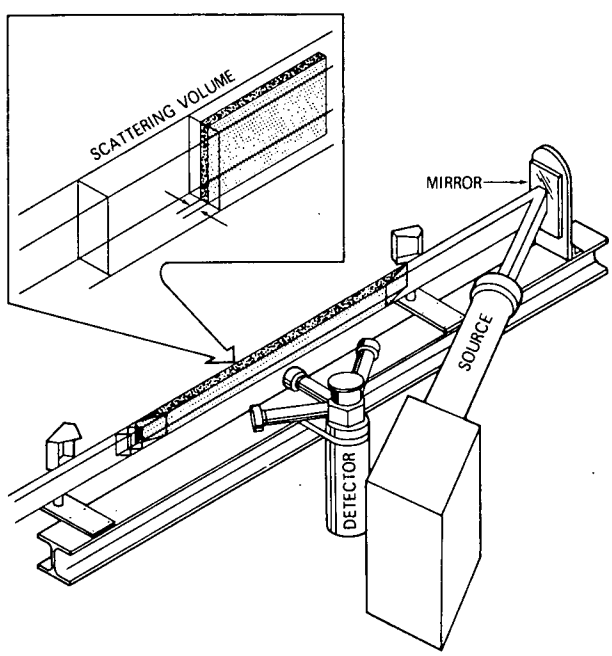

Fig. 5. Artist's rendition of modified integrating nephelometer.

from the Rayleigh molecular through ten increasingly steep functions representing a broad range of real atmospheric aerosols as determined from Barteneva (1960). Compensation for the approx. 7% variation in calibration due to aerosol variations is achieved by selecting the most appropriate constant on the basis of the nephelometers directional scattering measurements.

Inasmuch as the size and configuration of the Visibility Laboratory nephelometer preclude regular calibration by purging the sample volume with known gases as in Charlson *et al.* (1967) and Bodhaine (1979), secondary checks to validate the relative integrity of the measurements have been an important and continuous facet of our experimental procedure.

Coincident ground based measurements made by an integrating nephelometer and a long path transmissometer offer a convenient cross check under conditions of no atmospheric absorption and reasonably uniform horizontal stratification. The data in Fig. 6, illustrate a set of comparison measurements made between the Visibility Laboratory integrating nephelometer and an Eltro transmissometer similar to that illustrated in Douglas *et al.* (1977) during a joint operation in northern Germany, Duntley *et al.* (1976). These data represent two pairs of measurements made on each of two separate days, and show good comparison between the two system performances.

3.2. *Experimental measurements*

3.2.1. *Comparisons with visual observations.* One must keep in mind that the use of stable and reliable instrumentation does not imply that the measurements one gathers will describe a stable optical environment. Particularly in the lower troposphere, there are significant spatial and temporal variations in the optical state of the atmosphere that make machine vs. machine, or man vs. machine comparisons difficult. A simple illustration of this variability is shown in Fig. 7. In this illustration each rectangle represents the maximum variation in derived and reported visibilities that occurred during seventeen different data missions. The rectangular elements are typified by time intervals of approx. 2 h, and spatial intervals of approx. 60 km. This time-space interval is typical of that used during our experimental flight program for the accumulation of one set of ground level to 6 km measurements. Each rectangle represents one of 17 separate flights. Thus it is clear that even though the machine and the observer may both be doing their jobs properly as the trend of the data in Fig. 7 might indicate, it is essential that they be exactly coincident in the time and site of their performance if one is to expect precise correlation.

3.2.2. *Vertical variation of atmospheric aerosols.* If one is to address the generalized problem of slant path contrast transmittance through the atmosphere, then in addition to determining a single value of scattering coefficient which is suitable for approximating horizontal visibility via Equation (4), the spatial variation in scattering coefficient with changing altitude is also essential. These variations have been routinely documented as reported in Duntley *et al.* (1978) over large portions of the U.S.A. and Europe.

Two examples illustrating the broad variety in

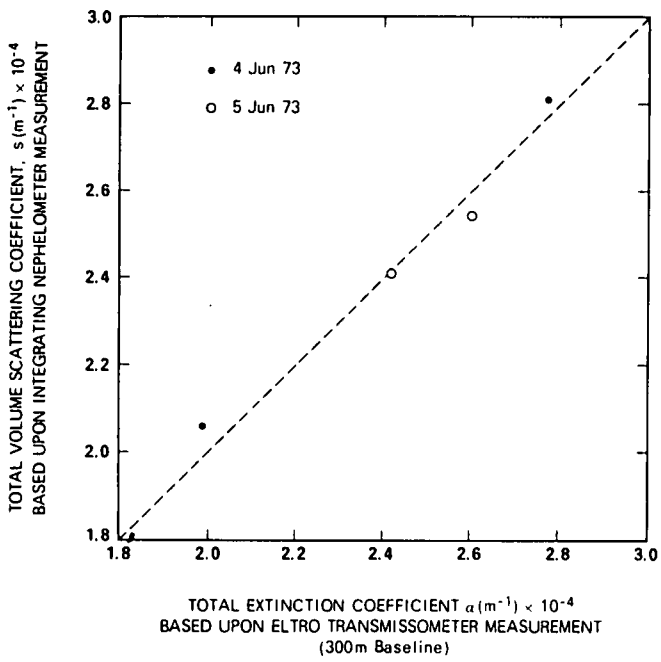

Fig. 6. Comparison of nephelometer and transmissometer data, Meppen, Germany (Duntley *et al.*, 1972).

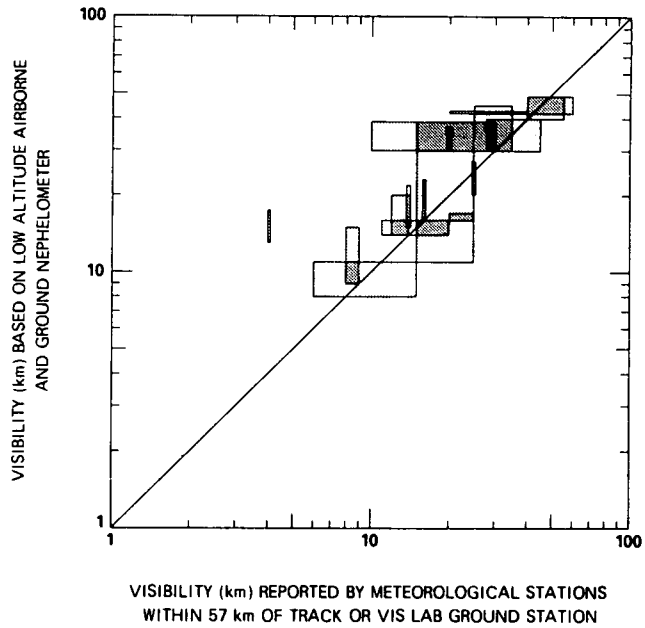

Fig. 7. Comparison of visibilities derived from nephelometer data (from Equation (4) where "visibility" $r = 3/\alpha$) with those reported by nearby meteorological stations.

vertical structure that one might anticipate are shown in Figs 8a and 8b. In these multi-spectral displays the filter identification code is as follows: Filter 2, mean wavelength at 447 nm; Filter 3, mean wavelength at 663 nm; Filter 5, mean wavelength at 750 nm, and Filter 4, mean wavelength at 550 nm, representing the pseudo photopic response which relates directly to the sensitivity of the human eye.

Flight C-372 illustrates the commonly found condition of a sharp haze top at about 2 km above ground level separating the relatively heavy low altitude haze from the clear air above. It also illustrates an additional feature not commonly shown as clearly as in this example. Whereas, one normally expects the scattering coefficient to decrease as altitude increases, it is not uncommon to find instances of increasing haziness and thus increasing coefficients as one climbs from the surface to near the haze top. This characteristic is clearly illustrated in the data for Filter 3 and is normally one found in profiles exhibiting relatively strong haze top demarcations.

Flight C-155 illustrates the extreme opposite condition which is far more appropriate to those concerned with monitoring and preserving our western desert environment. These data were obtained south of Albuquerque, New Mexico during a morning flight under clear conditions, with the flight crew reporting light haze on the horizons. These are probably as idealized a set of profiles as one might ever find. There is little or no structure with altitude, and as indicated by the high degree of parallelism between the data in each filter, there was exceptional temporal stability within the measurement interval.

Examination of profiles of the sort illustrated in Fig. 8(a) indicates that it is not uncommon for low altitude changes in scattering coefficient to exceed a factor of ten within the last 1000 m above the terrain. The magnitude and altitude of this often abrupt haze boundary are obviously major influences upon the determination of slant path transmittances through this lower altitude regime. It is equally apparent that few atmospheres are as uniform and well behaved as that represented by flight C-155, and that to assume so, as is often done in simple modelling exercises, may lead to significant error.

3.2.3. *Directional scattering of atmospheric aerosols.* The measurement of two discrete values of atmospheric directional scattering function coincidently with the measurement of total volume scattering coefficient is a powerful capability that is built into the Visibility Laboratory integrating nephelometer. It is essential, if one is to describe the optical properties of an atmosphere, either for a specific contrast transmittance determination, or for a general purpose modelling application, that a reliable entry into the directional characteristics of those properties be available. The work of Barteneva (1960) has been heavily utilized by the Visibility Laboratory as this entry, but there have been continuous queries as to the complete generality one could assign to the Barteneva data (Johnson *et al.*, 1979). Measurements made with our instrument have, I believe, answered that question beyond reasonable doubt.

Barteneva (1960) provides a catalog of proportional directional scattering functions $\sigma(\beta)/s$ for the photopic

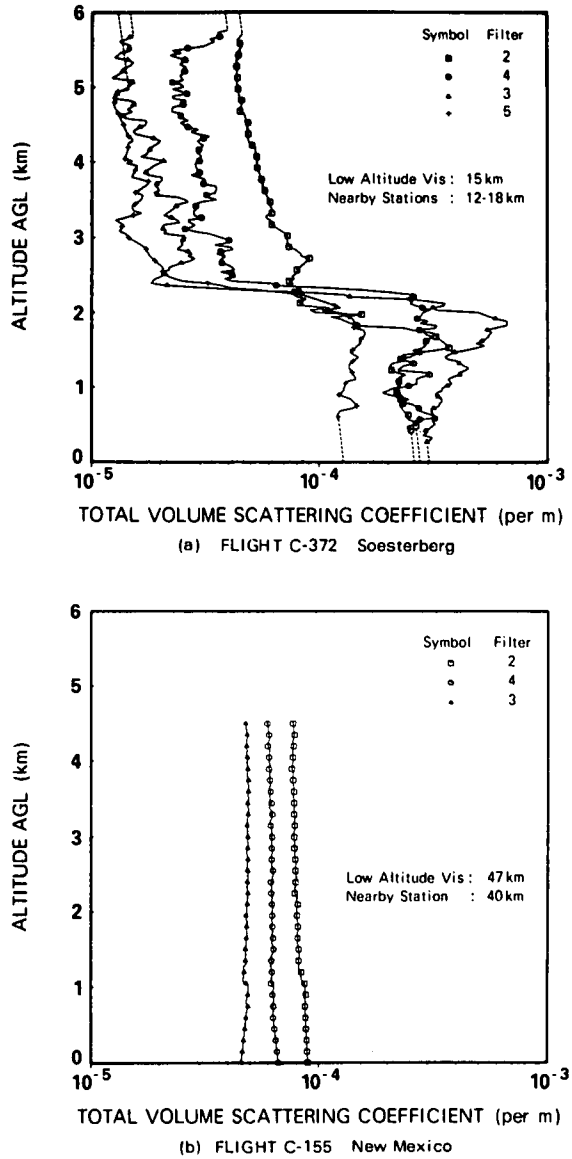

Fig. 8. Airborne measurements of volume scattering coefficient profiles under typically hazy conditions and under clear, cloud free conditions.

sensor based upon 624 measurements made during 1955–1958 at various locations in the U.S.S.R. and at sea. For each volume scattering function she gives a range of total volume scattering coefficients appropriate to that function. Median values of scattering coefficient were derived for each of the gradual scattering function classes, Nos 1–10. This resultant catalog of gradual functions and their associated median scattering coefficients is appropriate for describing atmospheres characterized as very clear to heavy haze, Nos 1 to 10 respectively.

It became apparent during the analysis of the measurements from the directional channels of Visibility Laboratory nephelometer that its data compared well to the Barteneva data. When its median scattering coefficient values and its gradual class $\sigma(\beta)/s$ curves were put into the form of their ratio to the Rayleigh (i.e., molecular scattering, as was the nephelometer data), then there was excellent correlation. Two sets of these comparative data are illustrated in Figs 9 and 10.

It is of significance to note that whereas the original Barteneva data represent photopic measurements at ground level, the Visibility Laboratory measurements include data from several separate bands within the visible spectrum and from within a broad range of altitudes.

In Figs 9 and 10, the horizontal axis is Optical Scattering Ratio $Q(z)$ which is defined as the ratio of the total volume scattering coefficient $s(z)$ to the Rayleigh scattering coefficient, ${}_{R}s(z)$ where z is the

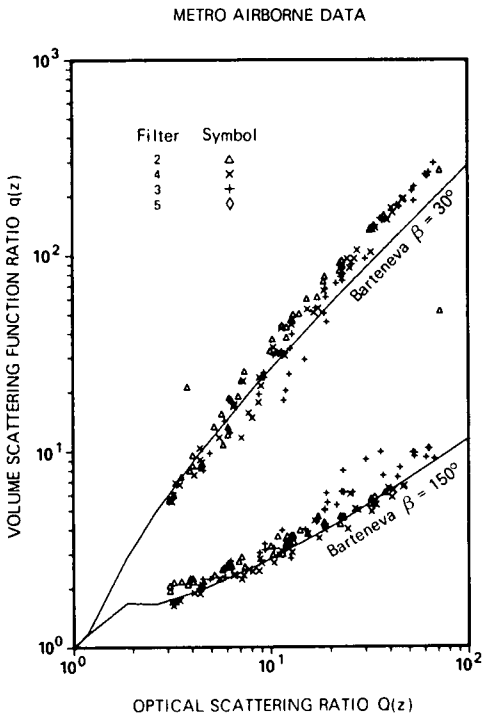

Fig. 9. Comparison of multi-spectral directional scattering ratios measured by Visibility Laboratory airborne nephelometer with the photopic ratios from Barteneva (1960).

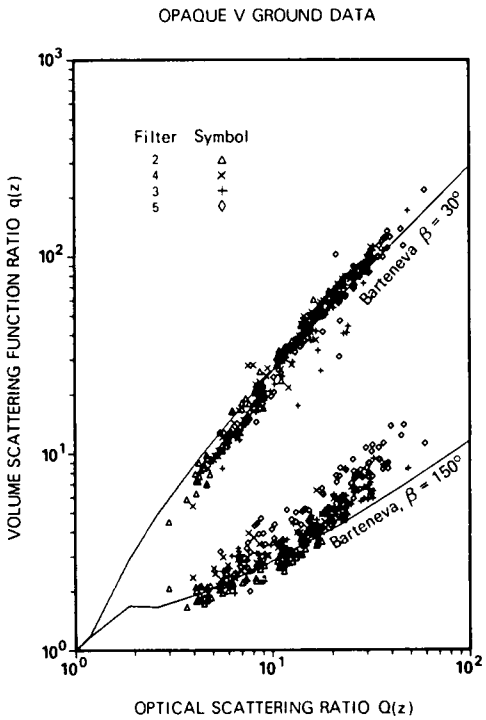

Fig. 10. Comparison of multi-spectral directional scattering ratios measured by Visibility Laboratory ground-based nephelometer with the photopic ratios from Barteneva (1960).

altitude designator:

$$Q(z) = \frac{s(z)}{{}_R s(z).} \tag{8}$$

The vertical axis is Volume Scattering Function Ratio, $q(z)$ which is the ratio of the total directional scattering function at angle beta, $\sigma(z, \beta)$ to the Rayleigh scattering function at the same angle and altitude, ${}_R\sigma(z, \beta)$:

$$q(z) = \frac{\sigma(z, \beta)}{{}_R\sigma(z, \beta)} \tag{9}$$

Figure 9 represents multi-spectral directional scattering function data measured during fourteen flights made in the vicinity of St. Louis, Ml., during the summer of 1971. In each case the measurements made at scattering angles of 30 and 150° are plotted as $q(z)$ against the coincidently measured values of total scattering coefficient converted to values of $Q(z)$. The solid lines are the equivalent data extracted from the Barteneva catalog. The correlation is good over the entire range of $Q(z)$.

Figure 10 represents additional multi-spectral data of the same sort as in Fig. 9, that was measured at ground level in conjunction with 19 flights made in western Europe during the summer of 1978. Again, the correlation is strong over a broad range of $Q(z)$.

The excellent comparisons of both the in-flight and surface measurements with the Barteneva directional data as illustrated in Figs 9 and 10 argue powerfully for accepting the general applicability of the Barteneva scattering function catalog. It is this experimental verification of general applicability that establishes the practicality of developing simple and reliable models of atmospheric directional scattering properties.

4. CONCLUSIONS

Although many early experimentalists established the viability of visual determinations of daytime contrast transmittance along horizontal paths of sight and related this determination to the concept of "visibility", there are equally well documented and sometimes not as fully understood associated caveats. However, within the boundaries established by these caveats, horizontal visibility determinations derived from instrumental measurements of atmospheric extinction coefficient are adequately relatable to visual observations.

The extension of these concepts to the more general case of contrast transmittance determinations along vertically inclined paths of sight implies knowledgability of the vertical variability in atmospheric extinction coefficient and the directional scattering properties along the path. These data have been obtained through the use of a multi-channel nephelometer and indicate a strong correlation between the measured scattering coefficient and the aerosol directional scattering function.

The modelling implications of these data are indeed enticing. The evidence to date strongly supports the contention that with an adequate specification of total

volume scattering coefficient $s(z)$ and its Rayleigh component, one can enter the Barteneva catalog or its parameterized equivalent, and obtain a truly representative expression of the directional scattering function $\sigma(z, \beta)$ for any spectral band within the visible spectrum. Thus, a reliable specification of the directional scattering properties of the atmospheric aerosol can be reasonably deduced from a measurement of the total volume scattering coefficient alone.

Acknowledgements—The author is pleased to acknowledge the contributions of Ms Jacqueline I. Gordon whose report, *Daytime Visibility, A Conceptual Review*, provided the majority of the material presented in Section 2, and who has assisted in the analysis of the data reported in Section 3. Additional interpretive insights have been contributed by Ms Janet E. Shields and Mr. Wayne S. Hering, members of the Visibility Laboratory staff.

The studies related to the preparation of this paper have been supported by the Air Force Geophysics Laboratory, Hanscom AFB, Massachusetts under Contract No. F19628-78-C-0200.

REFERENCES

Barteneva O. D. (1960) Scattering functions of light in the atmospheric boundary layer. *Bull. Acad. Sci. USSR, Geophys. Series*, 1237–1244.

Beuttell R. G. and Brewer A. W. (1949) Instruments for Measurements of Visual Range. *J. Scient. Instrum.* **26**, 357–359.

Blackwell H. R. (1946) Contrast thresholds of the human eye. *J. opt. Soc. Am.* 36, 624–643.

Bodhaine B. A. (1979) Measurements of the Rayleigh scattering properties of some gasses with a nephelometer. *App. Opt.* **18**, 1.

Charlson R. J., Horvath H. and Pueschel P. F. (1967) The direct measurement of atmospheric light scattering coefficient for studies of visibility and pollution. *Atmospheric Environment* **1**,

Crosby P. and Koerber B. W. (1963) Scattering of Light in the Lower Atmosphere. *J. opt. Soc. Am.* **53**, 358–361.

Douglas C. A. and Young L. L. (1945) Development of a transmissometer for determining visual range. U. S. Department of Commerce Civil Aeronautics Administration, Washington, D.C. Technical Development Report No. 47.

Douglas C. A. and Booker R. L. (1977) Visual range: concepts, instrumental determination, and aviation applications. U.S. Department of Transportation, Federal Aviation Administration, Systems Research and Development Service, FAA-RD-77-8, NTIS AD A041098.

Duntley S. Q. (1946) Visibility studies and some applications in the field of camouflage. Summary Technical Report, Dir. 16, NDRC, Columbia University Press, New York, Vol. 2, Appendix A.

Duntley S. Q. (1948) The reduction of apparent contrast by the atmosphere. *J. opt. Soc. Am.* **38**, 179–191.

Duntley S. Q., Johnson R. W., Gordon J. I. (1970) Airborne measurements of optical atmospheric properties at night. University of California, San Diego, Scripps Institution of Oceanography, Visibility Laboratory, SIO Ref. 70–7, AFCRL-70-0137, DDC AD 879734.

Duntley S. Q., Johnson R. W., Gordon J. I. (1976) Airborne measurements of optical atmospheric properties in northern Germany. University of California, San Diego, Scripps Institution of Oceanography, Visibility Laboratory, SIO Ref. 76–17, AFGL-TR-76-0188, NTIS AD A031496.

Duntley S. Q., Johnson R. W., Gordon J. I. (1978) Airborne measurements of optical atmospheric properties, summary and review III. University of California, San Diego, Scripps Institution of Oceanography, Visibility Laboratory, SIO Ref. 79-5, AFGL-TR-78-0286, NTIS, AD A073121.

Ensor D. S. and Waggoner A. P. (1970), Angular truncation error in the integrating nephelometer. *Atmospheric Environment* **4**, 481–487.

Fitzgerald J. W. (1977) Angular truncation error of the integrating nephelometer in the fog droplet size range. *J. appl. Met.* **16**, 198–204.

Gordon J. I. (1979) Daytime visibility, a conceptual review. University of California, San Diego, Scripps Institution of Oceanography, Visibility Laboratory, SIO Ref. 80–1, AFGL-TR-79-0257, NTIS ADA085451.

Grimes A. (1969) An annotated bibliography on methods of visibility measurement, 1950–1969. Atmospheric Sciences Library ESSA ATS/TM LIB 2, Scientific Information and Documentation Division, Rockville, MD.

Hering W. S., Muench H. S. and Brown H. A. (1971) Field test of a forward scatter visibility meter. Air Force Cambridge Research Laboratories, Hanscom Field, Bedford, Mass. AFCRL-71-0315.

Horvath H. and Noll K. E. (1969) The relationship between atmospheric light scattering coefficient and visibility. *Atmospheric Environment* **3**, 543–550.

Johnson R. W., Hering W. S., Gordon J. I., Fitch B. W., Shields, J. E. (1979) Preliminary analysis and modelling based upon Project OPAQUE profile and surface data. University of California, San Diego, Scripps Institution of Oceanography, Visibility Laboratory, SIO Ref. 80–5, AFGL-TR-79-0285.

Malm W. (1979) Considerations in the measurement of visibility. *J. Air Pollut. Control Ass.* **29**, 10.

Malm W. C., Leiker K. K. and Molenar J. V. (1980) Human perception of visual air quality. *J. Air Pollut. Control Ass.* **30**, 2.

Middleton W. E. K. (1952) Vision through the atmosphere. University of Toronto Press.

Moon P. and Spencer D. E. (1942) Illumination from a non-uniform sky. *Illum. Engng.* **37**, 707–726.

Rabinoff R. A. and Herman B. M. (1973) Effect of aerosol size distribution on the accuracy of the integrating nephelometer. *J. appl. Met.* **12**, 184–186.

Taylor J. H. (1964) The use of visual performance data in visibility prediction. *Appl. Opt.* **3**, 562–569.

World Meteorological Organization (1971) *Guide to Meteorological Instrument and Observing Practices*, Secretariat of the World Meteorological Organization, Geneva, Switzerland WMO-No. **8**, TP. 3

APPENDIX C

Reprinted from JOURNAL OF THE ATMOSPHERIC SCIENCES, Vol. 38, No. 12, December 1981
American Meteorological Society
Printed in U. S. A.

Effects of Reflection by Natural Surfaces on the Radiation Emerging from the Top of the Earth's Atmosphere

BRUCE W. FITCH[1]

Department of Land, Air and Water Resources, University of California, Davis 95616

(Manuscript received 24 March 1981, in final form 24 July 1981)

ABSTRACT

The radiation emerging from the top of the earth's atmosphere is affected by the reflection characteristics of the underlying surface. Laboratory-gathered bidirectional reflectance data were used to characterize the reflection matrix for three different types of natural surfaces. The radiation emerging from the top of a pure molecular and an aerosol-laden plane parallel atmosphere was calculated for these three diverse types of surfaces and their Lambert model equivalents. The calculations indicate that the radiation emerging from the top of the atmospheres is significantly different for a real surface compared to a Lambert model. For the molecular atmosphere the difference is most pronounced at a wavelength of 0.6 μm; this is mainly due to the light directly transmitted downward through the atmosphere, reflected, and then directly transmitted outward through the top of the atmosphere. For a turbid atmosphere the difference also is due to light with a history of diffuse transmission because the strong forward scattering of the aerosols partially offsets the smoothing effect of the diffuse multiple scattering. The calculations indicate that the polarization of the light emerging from the top of the atmosphere strongly mirrors the polarization reflected from the underlying surface. Thus, satellite-measured polarization would be an excellent parameter for distinguishing ground features with similar reflectance but different polarization characteristics.

1. Introduction

To facilitate the interpretation of data gathered from satellites and aircraft, many investigators have made computations of the radiation emerging from the earth's atmosphere overlying various types of surfaces. In most cases, the radiation reflected from the surface was considered isotropic and unpolarized, corresponding to the Lambert approximation. The radiation emerging from the top of an atmosphere overlying different natural surfaces has been investigated by Coulson *et al.* (1966) using a Rayleigh atmosphere and by Keopke and Kriebel (1978) using a turbid atmosphere overlying vegetated surfaces reflecting light of an unknown degree of polarization. These investigators found significant differences in this emergent radiation compared to the radiation emerging from an atmosphere overlying a Lambert surface, even though the albedo of the Lambert surface was equal to the albedo of the natural surface. Because surface reflection influences the emergent radiation, the characteristics of the radiation emerging from a pure molecular (Rayleigh) and an aerosol-laden atmosphere overlying different types of surface materials is investigated here.

In this paper, the radiation emerging from the top of a Rayleigh and a turbid plane parallel nonabsorbing atmospheric model overlying three types of natural surfaces of known directional reflectance and polarization is described.

2. Atmosphere-surface model

The solar radiation emerging from the top of an atmosphere illuminated by parallel radiation $\pi\mathbf{F}$ can be expressed as an infinite series, with each term in the series having its own history of transmission, scattering and surface reflection. A few of the terms depicting the radiation emerging from the atmosphere are shown in Fig. 1. By summing the terms in the series, the radiance $\mathbf{I}(\tau; \mu, \phi)$ emerging from the top of a planetary atmosphere of normal optical thickness τ_1 can be written as

$$\begin{aligned}\mathbf{I}(\tau = 0; \mu, \phi) &= \mathbf{S}\pi\mathbf{F} + e^{-\tau_1/\mu}\mathbf{E}\mathbf{R}e^{-\tau_1/\mu_0}\mathbf{E}\pi\mathbf{F} + e^{-\tau_1/\mu}\mathbf{E}\mathbf{R}\mathbf{T}\pi\mathbf{F} \\ &\quad \text{first} \qquad \text{second} \qquad \text{third} \\ &\quad + \mathbf{T}^*\mathbf{R}e^{-\tau_1/\mu_0}\mathbf{E}\pi\mathbf{F} + \mathbf{T}^*\mathbf{R}\mathbf{T}\pi\mathbf{F} + (e^{-\tau_1/\mu}\mathbf{E} + \mathbf{T}^*)\mathbf{R} \\ &\quad \text{fourth} \qquad \text{fifth} \\ &\quad \times (\mathbf{S}^*\mathbf{R} + \mathbf{S}^*\mathbf{R}\mathbf{S}^*\mathbf{R} + \cdots)(e^{-\tau_1/\mu_0}\mathbf{E} + \mathbf{T})\pi\mathbf{F}, \quad (1)\end{aligned}$$

[1] Present affiliation: Visibility Laboratory, Scripps Institution of Oceanography, University of California, San Diego 92093.

0022-4928/81/122717-13$07.25

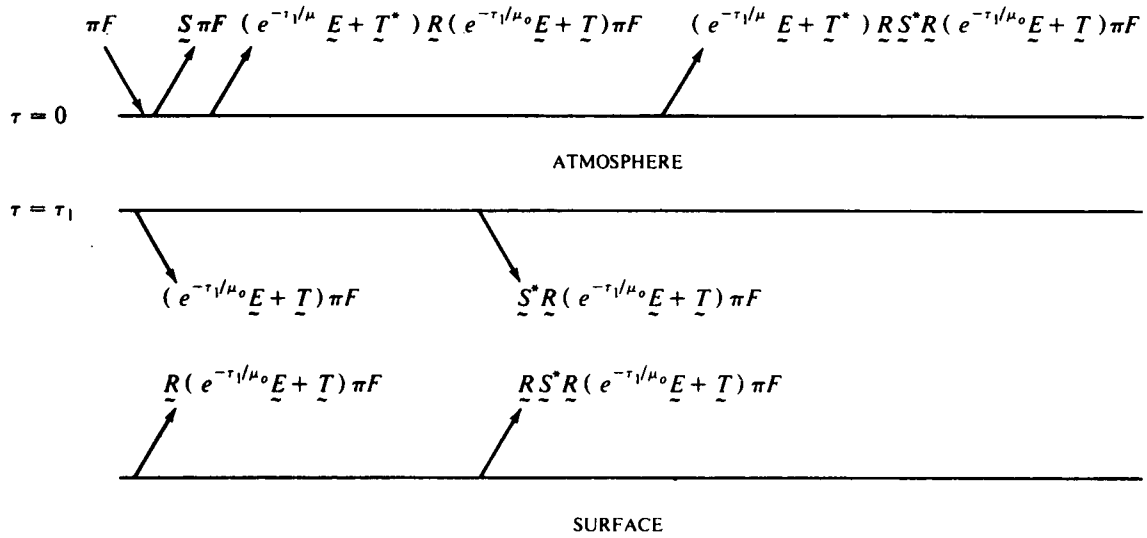

FIG. 1. Diagrammatical representation of some of the components of the total emergent light. πF is the solar radiation incident on the atmosphere having a total optical thickness τ_1, and **S** and **T** are the diffuse reflection and transmission matrices, respectively. The term $e^{-\tau_1/\mu_0}$ **E** represents direct transmission through the atmosphere, where **E** is the unit matrix. The reflection characteristics of the surface are described by **R**.

where $\theta = \cos^{-1}\mu$ is the nadir viewing angle, ϕ the azimuthal angle, $\mathbf{I}(\tau; \mu; \phi)$ and **F** are vectors, and **E** is the 3×3 unit matrix. The position of the sun, or source, is given by the zenith angle $\theta_0 = \cos^{-1}\mu_0$ and the azimuthal angle $\phi_0 = 0°$. At the top of the atmosphere $\tau = 0$.

For convenience, parallel radiation of net flux $\pi\mathbf{F}$ per unit area normal to the beam is assumed incident on the top of the atmosphere. Using the Stokes parameter representation (F_I, F_Q, F_U, F_V), **F** is (1, 0, 0, 0). Experiments show that the ellipticity of light reflected from the natural surfaces is sufficiently small to be neglected (Coulson, 1978)[2], in which case $F_V = V = 0$.

The first term of Eq. (1) represents the solar radiation diffusely reflected from the top of the atmosphere. The second, third, fourth and fifth terms represent the solar radiation that is directly or diffusely transmitted through the atmosphere, reflected from the surface, and then directly or diffusely transmitted back out from the top of the atmosphere. The last term of Eq. (1) describes the radiation reflected more than once from the surface. For clarity, the factor $(4\pi\mu)^{-1}$ is included as part of the diffuse reflection matrix **S** and the diffuse transmission matrix **T** first defined by Chandrasekhar (1960). The 3×3 reflection matrix **R** for a real surface is obtained from laboratory measurements of the bidirectional reflectance, degree of linear polarization, and angle χ between the vertical plane and the plane of polarization of the reflected light. For a Lambert surface all the elements of **R** are zero except R_{11} which is a function of the total reflectance of the surface. Although it is not specifically shown, the product of two bidirectional matrices also implies hemispherical integration. For example,

$$\mathbf{S^*R} \equiv \int_0^{2\pi}\int_0^1 \mathbf{S^*}(\tau_1; \mu, \phi; \mu', \phi') \times \mathbf{R}(\mu', \phi'; \mu_0, \phi_0)d\mu' d\phi'.$$

The matrix $\mathbf{S^*}$ is related to the diffuse reflection matrix **S** by

$$\mathbf{S^*} = \mathbf{QSQ},$$

where

$$\mathbf{Q} = \begin{pmatrix} 1 & 0 & 0 \\ 0 & 1 & 0 \\ 0 & 0 & -1 \end{pmatrix}.$$

The matrix **Q** takes into account a change in symmetry, discussed by Hovenier (1969), which occurs when the atmosphere is illuminated from the bottom rather than from the top. The definition of $\mathbf{T^*}$ is similar.

The first atmosphere used in the atmosphere-surface model was a Rayleigh atmosphere. The values of the wavelength-dependent $\tau_1(R)$ used were taken from Elterman (1968)[3] and are presented in Table 1. The diffuse reflection and transmission matrices describing the pure molecular atmosphere

[2] Coulson, K. L., 1978: Private communications.

[3] Elterman, L., 1968: UV, visible, and IR attenuation for altitudes to 50 km, 1968. AFCRL-68-0153, 49 pp.

APPENDIX C

were evaluated by utilizing a computer program developed by Dave and Warten (1968).[4]

An aerosol-laden atmosphere was introduced into the atmosphere-surface model to investigate the effects of the strong forward scattering characteristic of aerosols. The total normal optical thickness $\tau_1(t)$ of the turbid atmosphere is the sum of the Rayleigh optical thickness $\tau_1(R)$ and the normal optical thickness of the aerosol content $\tau_1(a)$. The values of $\tau_1(a)$, shown in Table 1, were taken from Elterman (1968).[3] The refractive index of the particles is assumed to be $m = 1.33 - 0i$ with a size distribution described by the Haze L model of Deirmendjian (1969). The elements of the diffuse reflection and transmission matrices describing the turbid atmosphere were calculated using the adding method with a program graciously provided by Dr. T. Takashima and described in Takashima (1974). Because of the method of numerical integration used in the adding method, the matrices **S** and **T** could not be calculated at the exact angles θ_0 used to illuminate the real surfaces in the laboratory experiments. For surface illumination $\theta_0 = 53$ and 78.5°, the difference, being less than 2.5°, was ignored. For $\theta_0 = 0°$ the difference is 11° but its influence is small because **S** and **T** as a function of θ_0 change slowly in the region $\theta_0 = 0°$.

Once the diffuse reflection and transmission matrices describing the different atmospheres have been computed, only the surface reflection matrix, describing the natural surfaces, is needed in order to evaluate the terms of Eq. (1) for the different atmosphere-surface combinations. The Stokes parameters I, Q and U, together with the degree of polarization, were computed for each of the first five terms of the equation by using the Gaussian quadrature method of integration.

3. Reflection characteristics of the natural surfaces

The surfaces used in this study, from the Lambert-like gypsum sand to the highly anisotropic polarizing Yolo loam (a dark, loamy soil) represent the reflection characteristics of a variety of natural surfaces. The reflection data for Yolo loam, gypsum sand and Mojave Desert sand are taken from the laboratory measurements by Chen *et al.* (1967).[5] For these measurements the surfaces of the three samples were level. The bidirectional reflectance and polarization of the reflected light were measured for three types of illumination: 1) natural light, 2) light polarized 90° and 3) light polarized 45° to the vertical plane. The use of the different types of illumination enabled the determination of nine elements of **R** for a specific surface, wavelength and angle of illumination. The angle χ was assumed to be perpendicular to the scattering plane; this assumption was found by observation to be reasonable.

TABLE 1. Values of the wavelength-dependent optical thicknesses used to construct the atmospheres at each of the three wavelengths.

Wavelength (μm)	$\tau_1(R)$	$\tau_1(a)$	$\tau_1(t)$
0.4	0.36	0.32	0.68
0.5	0.15	0.26	0.41
0.6	0.07	0.24	0.31

The reflected radiances measured by Chen *et al.* were normalized with the value of the radiance reflected from the given surface into the nadir (when $\theta_0 = 0°$ normalization was performed with respect to $\theta = 15°$). The correction factors used to renormalize the data to the radiance reflected from a standard surface of known reflectance were obtained from Coulson (1978)[2] and Walraven and Coulson (1972)[6] who measured the reflectance of the same surface samples at the same wavelengths. For Yolo loam and Mojave Desert sand data were available for all three types of illumination except for $\theta_0 = 0°$ where only data for illumination by natural light were available. For gypsum sand it was necessary to renormalize the directional reflectance independent of illumination type. The measured polarization of the light reflected from the surfaces was not affected by the renormalization.

The bidirectional reflectance of the three surfaces in the principal plane $\phi = 0°(180°)$ for the wavelength $\lambda = 0.6$ μm and $\theta_0 = 0°$ is shown in Fig. 2. The reflectance of a Lambert surface would be characterized by a straight horizontal line in this figure. The reflectance of the three surfaces is independent of the azimuthal angle, so that the hemispheric pattern of reflectance can be generated by a rotation around the nadir. The highly reflecting gypsum sand shows a distinct darkening at the large nadir angles and a fairly constant value of reflectance at the nadir angles $\theta < 50°$. The absorbent Yolo loam, in contrast, has a lower reflectance as well as exhibiting a backward maximum centered about $\theta = 0°$. Moreover, Yolo loam shows no distinct darkening at large nadir angles as does gypsum sand. The strong backward maximum and the lack of darkening

[4] Dave, J. V., and R. M. Warten, 1968: Program for computing the Stokes parameters of the radiation emerging from a plane-parallel, non-absorbing, Rayleigh atmosphere. Rep. No. 320-3248, IBM Scientific Center, Palo Alto, CA, 80 pp.

[5] Chen, Hsi-shu, C. R. Nagaraja Rao and A. Sekera, 1967: Investigation of the polarization of light reflected by natural surfaces. Sci. Rep. No. 2, Contract AF 19(628)-3850, University of California, Los Angeles, 96 pp.

[6] Walraven, R. L., and K. L. Coulson, 1972: Measurements of the light-reflecting properties of white gypsum sand. *Contrib. Atmos. Sci.*, No. 7, University of California, Davis.

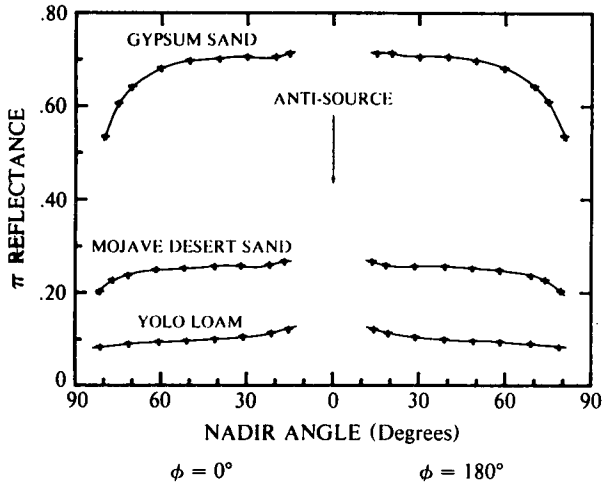

FIG. 2. Bidirectional reflectance of gypsum sand, Mojave Desert sand and Yolo loam in the principal plane for $\lambda = 0.6\ \mu m$ and $\theta_0 = 0°$.

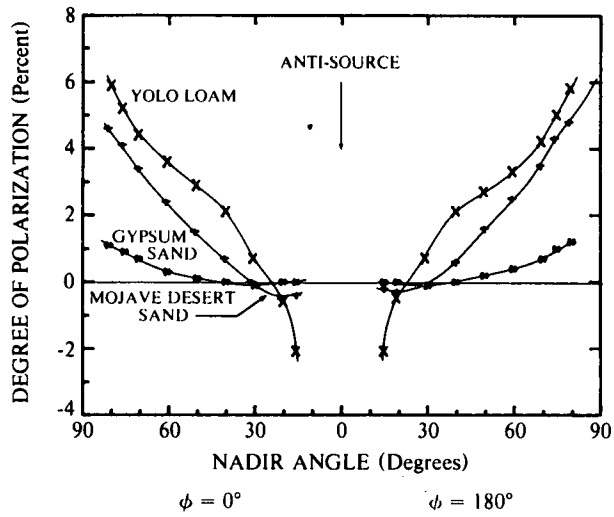

FIG. 4. Degree of polarization of radiation reflected from gypsum sand, Mojave Desert sand and Yolo loam in the principal plane for $\lambda = 0.6\ \mu m$ and $\theta_0 = 0°$.

at large angles, characteristic of Yolo loam but not of gypsum sand, is probably a result of the particles of gypsum sand being fairly translucent and those of Yolo loam opaque. The features of the curve characterizing the reflectance of Mojave Desert sand seem to be a blend of those found in gypsum sand and in Yolo loam.

The effect of increasing the zenith angle of the source is shown in Fig. 3. The measurements are for $\lambda = 0.6\ \mu m$ and $\theta_0 = 53°$. The curves for all three surfaces show a marked increase in total reflectance and an increase in the magnitude of the backward maximum. The strong forward reflection in the $\phi = 0°$ plane increases with increasing θ_0.

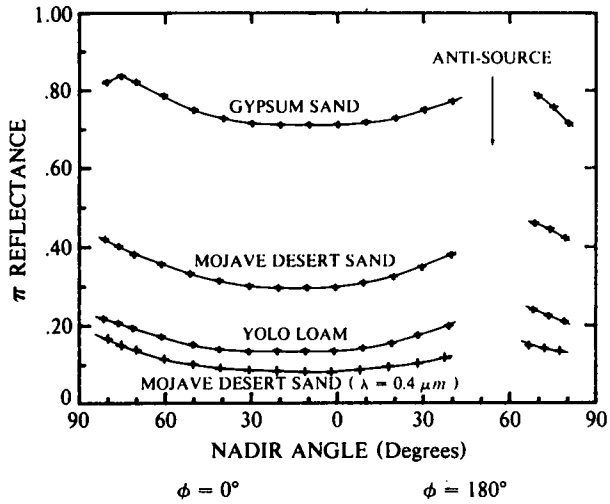

FIG. 3. Bidirectional reflectance of gypsum sand, Mojave Desert sand and Yolo loam in the principal plane for $\lambda = 0.6\ \mu m$ and $\theta_0 = 53°$, and of Mojave Desert sand for $\lambda = 0.4\ \mu m$ and $\theta_0 = 53°$.

Also shown in the figure is the bidirectional reflectance of Mojave Desert sand for $\lambda = 0.4\ \mu m$ and $\theta_0 = 53°$. The decrease in reflectance with decreasing wavelength is characteristic of all three surfaces.

The degree of linear polarization of the radiation reflected from the three surfaces in the principal plane for $\lambda = 0.6\ \mu m$ and $\theta_0 = 0°$ is presented in Fig. 4. A comparison of the profiles in Fig. 2 with those of Fig. 4 shows that the reflectance increases inversely to the maximum degree of polarization (Omov's principle). In the principal plane, positive polarization indicates that the plane of polarization is perpendicular to the plane; negative polarization indicates that the plane of polarization is parallel to this vertical plane. The positively polarized light is considered a property of singly reflected light; the negatively polarized light occurring in the region of the anti-source is considered a result of light being doubly reflected (Wolff, 1975).

Large values of polarization for the three surfaces are seen in Fig. 5 for $\theta_0 = 53°$ and $\lambda = 0.4\ \mu m$. The large values of polarization in the $\phi = 0°$ plane are probably a result of the dominance of singly reflected light in this region. The maximum degree of polarization for Mojave Desert sand is larger when the wavelength is $0.4\ \mu m$ than when it is $0.6\ \mu m$ as shown in the figure. This agrees with Omov's principle since the reflectance of the surface increases as the wavelength increases.

4. Radiance outward from a Rayleigh atmosphere

For these computations, each real surface was assumed to be an infinite plane underlying a plane

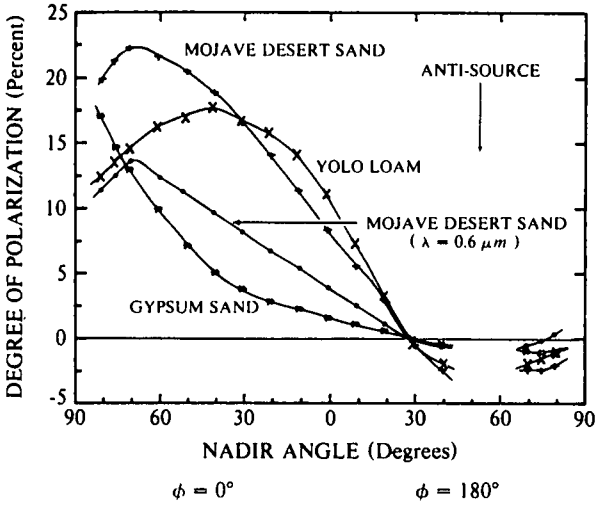

FIG. 5. Degree of polarization of radiation reflected from gypsum sand, Mojave Desert sand and Yolo loam in the principal plane for $\lambda = 0.4\ \mu$m and $\theta_0 = 53°$, and for Mojave Desert sand for $\lambda = 0.6\ \mu$m and $\theta_0 = 53°$.

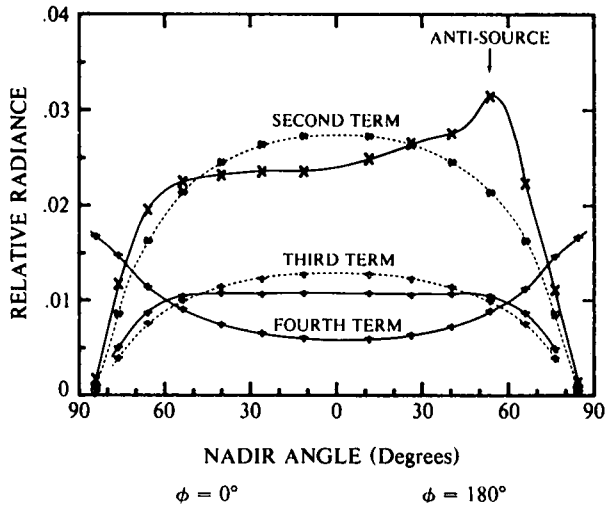

FIG. 6. Relative radiance of the major surface reflection terms of the total emergent radiation as defined by Eq. (1) for a pure molecular atmosphere overlying Mojave Desert sand (principal plane, $\lambda = 0.4\ \mu$m, $\theta_0 = 53°$). Solid lines indicate real surface reflection; dashed lines indicate Lambert surface reflection.

parallel pure molecular model of the earth's atmosphere.

a. Results for a Mojave Desert sand surface

The relative radiances of the first three surface reflection terms of Eq. (1) for the light emerging from the top of a Rayleigh atmosphere overlying Mojave Desert sand for $\lambda = 0.4\ \mu$m and $\theta_0 = 53°$ are shown by the profiles in Fig. 6. The radiance of the second term of Eq. (1) as a function of nadir angle for real surface reflection (solid line) is compared to the radiance of the same term for reflection by a Lambert surface (dashed line) of the same total monochromatic reflectance, $A = 0.12$. At large nadir angles the differences between the two curves show the effect of the forward and backscattered peaks in the reflected radiance for the desert sand depicted in Fig. 3. Though not as great, these differences are still present for the third term which represents diffuse illumination of the surface. The curves of both the second and third terms show that the Lambert approximation overestimates the real surface reflection in the region of the nadir. The strong smoothing influence of diffuse transmission out from the top of the atmosphere is illustrated by the lack of any observable difference between the fourth term of Eq. (1) and its Lambert counterpart. The differences between the remaining surface reflection terms of Eq. (1) and their Lambert counterparts are negligible.

The influence on the emergent radiance of reflection by Mojave Desert sand instead of its Lambert equivalent is shown in Fig. 7. The figure shows the percent change or needed correction in the total

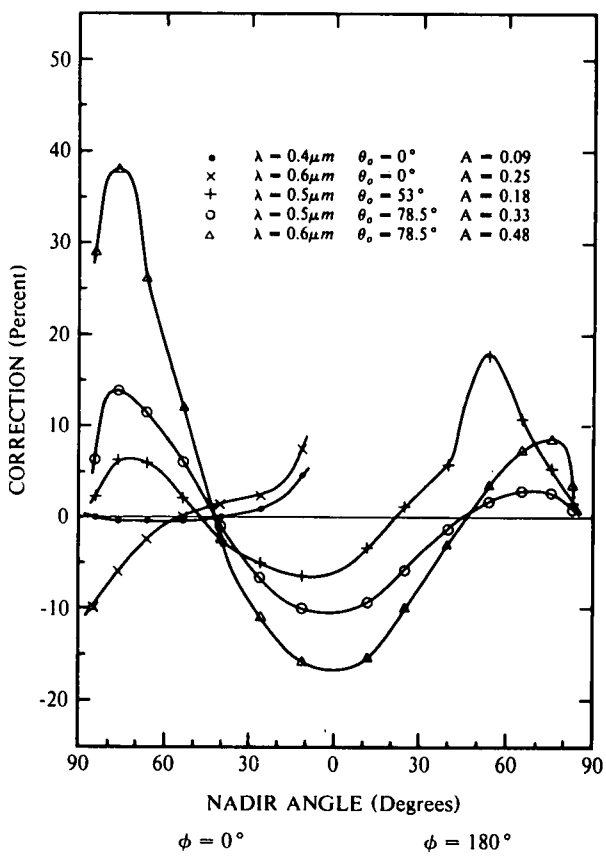

FIG. 7. Correction to the total radiance emerging from a Rayleigh atmosphere overlying a Lambert surface of total reflectance A that occurs when the reflection matrix of Mojave Desert sand is used in term two of Eq. (1).

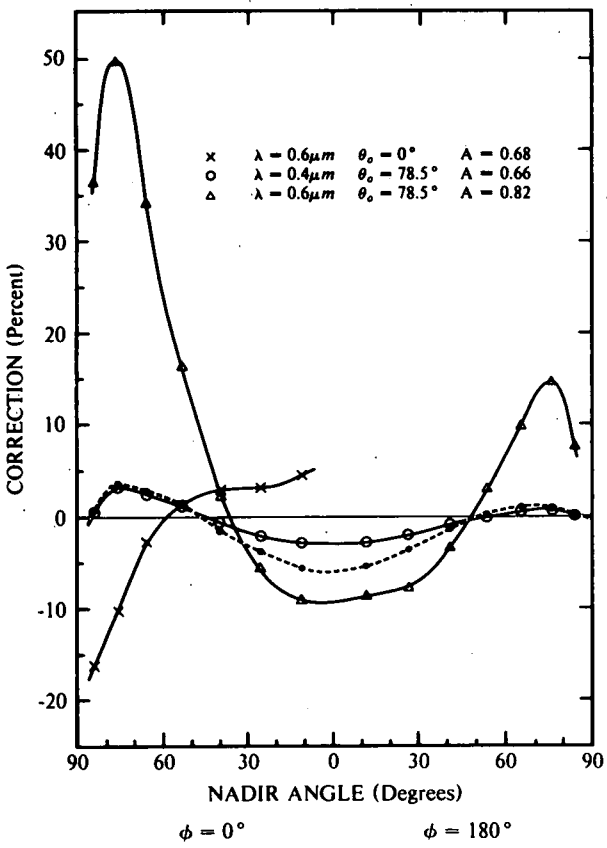

FIG. 8. Correction to the total radiance emerging from a Rayleigh atmosphere overlying a Lambert surface of total reflectance A that occurs when the reflection matrix of gypsum sand is used in term two of Eq. (1) or in terms two and three as shown by the dashed curve.

emergent radiance calculated using the Lambert approximation in Eq. (1) as compared to the results obtained when real surface reflection is included in the dominant second term and the Lambert approximation in the remaining surface reflection terms. A positive correction indicates that Lambert surface reflection underestimates the real surface reflection and vice versa. The positive values of correction in the region of the nadir and the negative values of correction at large θ for $\lambda = 0.4$ and 0.6 μm when $\theta_0 = 0°$ show the influence of the backscatter maximum and the decrease in bidirectional reflectance with increasing θ for the desert sand seen in Fig. 2. The small values of correction for the wavelength 0.4 μm are a result of the large optical thickness at this wavelength which decreases the contribution of the surface reflection terms to the total emergent light. The increasing importance of the forward scattered peak of the bidirectional reflectance as the solar zenith angle increases is also shown in Fig. 7. When $\lambda = 0.5$ μm the maximum change in the $\phi = 0°$ plane is ~14% for $\theta_0 = 78.5°$ and 7% for $\theta_0 = 53°$. As the wavelength increases to 0.6 μm, decreasing the influence of the first term of Eq. (1), the effects of the real surface become very large for $\theta_0 = 78.5°$. It is interesting that the Lambert surface approximation works well in the region $\theta = 40$–$45°$ and $\phi = 0°$ for all the cases studied in Fig. 7.

The third term of Eq. (1) is of next importance, after the second term, in introducing the effects of real surface reflection. The influence on the correction of the inclusion of real surface reflection by the third term which represents diffuse illumination of the surface is largest for the larger solar zenith angles. This term has its maximum influence in the region of the nadir where, for $\lambda = 0.5$ μm, it contributes −1.4 and −2.6% to the correction when $\theta_0 = 53$ and 78.5°, respectively. When $\theta_0 = 0°$ the cumulative influence of the surface reflection terms, other than the second, on introducing the effects of real surface reflection is negligible.

b. Results for a gypsum sand surface

The correction introduced by gypsum sand is presented in Fig. 8. The change introduced by the second term for $\lambda = 0.6$ μm and $\theta_0 = 78.5°$ again shows the importance of the forward and backscattered maxima on the total emerging light. When $\lambda = 0.4$ μm, the change is much smaller due to a decrease in the surface reflection and an increase in the optical thickness of the atmosphere. The cumulative effect of real surface reflection by the second and third terms, shown by the dashed curve, shows that in the region of the nadir the effect of these two terms is fairly equal and their total effect on the emergent radiance is significant. The influence of the darkening at large θ and the backscattered maximum present in the curves of bidirectional reflectance for gypsum sand is clearly visible in the curve for $\lambda = 0.6$ μm and $\theta_0 = 0°$. For all the cases shown in Fig. 8 the Lambert approximation works well in the region of $\theta = 40°$.

c. Results for a Yolo loam surface

To investigate the effects of a surface with a low total reflectance, a Yolo loam surface was included in the atmosphere-surface model. Fig. 9 presents the curves of correction which demonstrate the influence of real surface reflection by the second term only. The pronounced backscattered maximum characteristic of Yôlo loam is clearly shown by the positive values of correction in the region of the nadir for $\lambda = 0.4$ and 0.6 μm when $\theta_0 = 0°$. A change in solar zenith angle to 78.5° for $\lambda = 0.6$ μm produces large corrections in the region of the nadir and the forward and backscatter maxima. These corrections are effectively reduced by the larger atmospheric reflection and smaller surface reflection present when $\lambda = 0.4$ μm. Including the effect of real reflection by the third term, however, approximately doubles the correction in the region of the

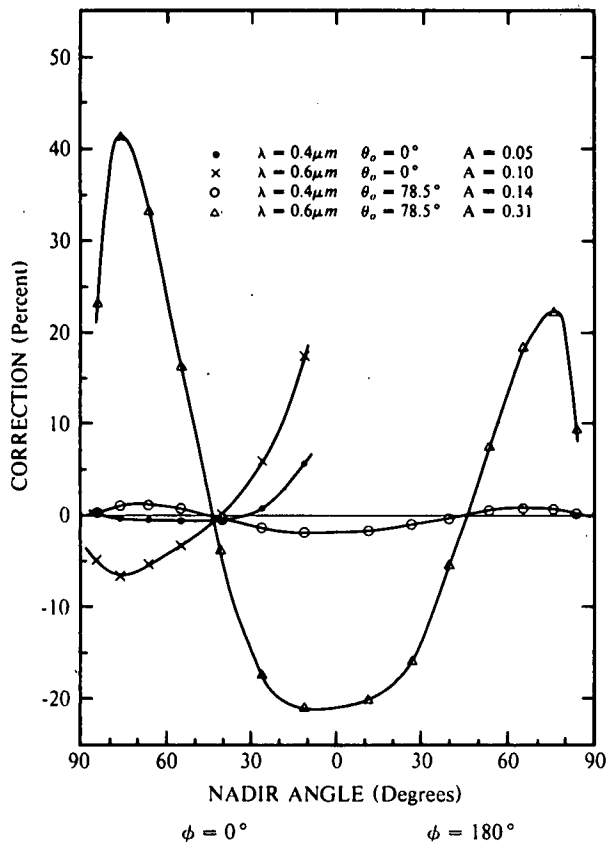

FIG. 9. Correction to the total radiance emerging from a Rayleigh atmosphere overlying a Lambert surface of total reflectance A that occurs when the reflection matrix of Yolo loam is used in term two of Eq. (1).

nadir. The Lambert approximation works well in the region of $\theta = 45°$ for the cases presented in Fig. 9.

The previous discussions were confined to the $\phi = 0°$ (180°) plane. The difference in radiance of the second term for reflection by Mojave Desert sand and its Lambert equivalent is presented in the hemisphere map (Fig. 10). The source zenith angle is 53° and the wavelength is 0.5 μm. The large differences are centered on the principal plane, indicating the importance of this plane. The positive differences at large nadir angles are a result of the forward and backscattered maxima. The negative values in the region of the nadir indicate the Lambert surface approximation overestimates the reflected radiance in this region. Because the surface reflection characteristics are symmetrical about the plane $\phi = 0°$ (180°) the values in Fig. 10 are representative of the values occurring in the opposite hemisphere.

5. Radiance outward from a turbid atmosphere

A turbid atmosphere was used in the atmosphere-surface model with Mojave Desert sand to study the effects of aerosol scattering on the emergent light. The effect of real surface reflection by the second term on the total radiance is shown for both the turbid and pure molecular atmospheres in Fig. 11. The decrease in correction caused by the increased multiple scattering of the turbid atmosphere is evident by comparing curves representing the different atmospheres but the same wavelength and solar zenith angle. In addition, the figure compares the effect of the second and third terms. The combined influence of real surface reflection by the second and third terms for $\lambda = 0.6$ μm and $\theta_0 = 78.5°$ is shown by the dashed line in Fig. 11. The effect of the third term, depicted by the large differences between the dashed line and the line symbolized by plus marks indicate that the strong forward scattering of the aerosols have significantly offset the smoothing effect of multiple scattering by the aerosols. The influence of the third term is also significant at

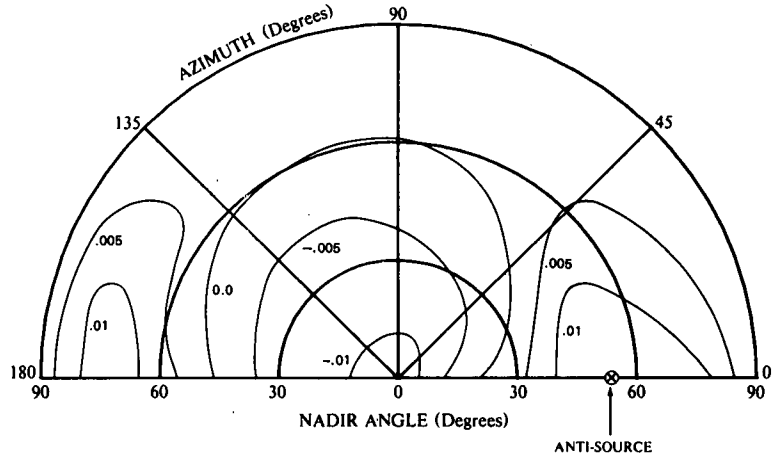

FIG. 10. Hemispheric map of the difference in relative radiance of the second term of Eq. (1) for real and Lambert surface reflection (Mojave Desert sand, $\lambda = 0.5$ μm, $\theta_0 = 53°$).

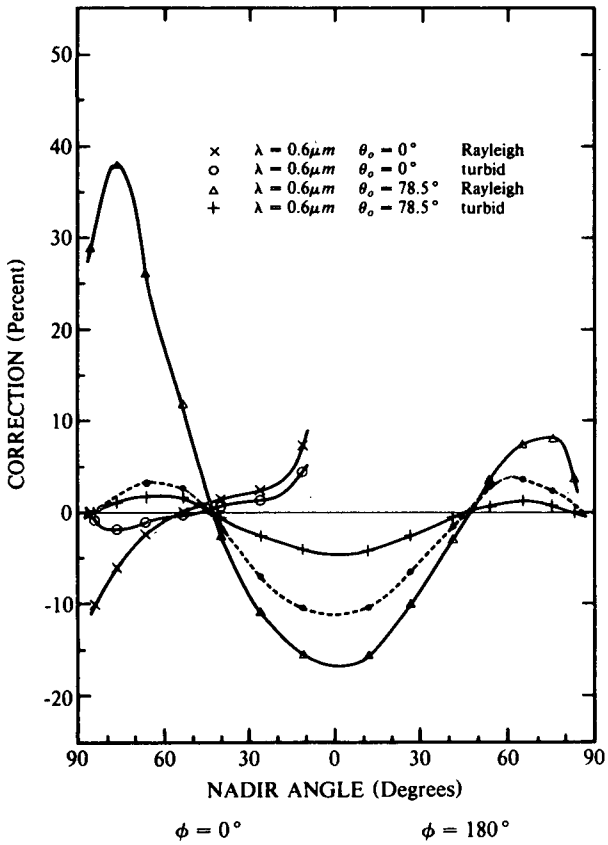

FIG. 11. Correction to the total radiance emerging from Rayleigh and turbid atmospheres overlying a Lambert surface of total reflectance A that occurs when the reflection matrix of Mojave Desert sand is used in term two of Eq. (1) or in terms two and three as shown by the dashed curve.

$\lambda = 0.4$ μm, though not shown in the figure. When $\theta_0 = 78.5°$ and $\lambda = 0.4$ μm the maximum correction in the region of the nadir is increased from less than 0.3% to slightly over 2% when the effect of this term is included. When $\theta_0 = 0°$ the cumulative influence of the surface reflection terms, other than the second, is negligible, except at $\lambda = 0.6$ μm. In this case, the second and fourth terms can combine at large θ to give a total correction of -3%. In general, the corrections occurring for the turbid atmosphere increase with increasing wavelength but remain below those found in the pure molecular atmosphere. The Lambert surface approximation works well in the region of $\theta = 45°$ for the Rayleigh and turbid atmospheres presented in Fig. 11.

Including the effects of aerosol scattering in the atmosphere-surface model tends to decrease the importance of using a real surface for calculating the emergent radiance. Nevertheless, the influence of real surface reflection for an aerosol-laden atmosphere is still significant. The apparent importance of the fourth term at large nadir angles when $\theta_0 = 0°$ is probably the result of a relatively large direct transmission of light to the surface, followed by a large diffuse transmission out from the top of the atmosphere at large nadir angles. When $\theta_0 = 78.5°$ the importance of the third term at small nadir angles is likely due to a highly anisotropic beam of diffuse light incident on the surface which, after surface reflection, is directly transmitted out through the atmosphere at the smaller optical thickness occurring in the region of the nadir. The strong forward scattering of the aerosols preserves some of the anisotropy of the surface reflected light even in an optically thick atmosphere with large multiple scattering.

6. Polarization outward from a Rayleigh atmosphere

Another interesting feature of reflection by natural surfaces is their effect on the behavior of the polarization of the emergent light.

a. Results for a Mojave Desert sand surface

The degree of polarization of the emergent radiation in the principal plane for Mojave Desert sand is shown in Fig. 12 for $\lambda = 0.5$ μm and $\theta_0 = 53°$. Included for comparison are the curves of polarization for a Rayleigh atmosphere overlying a Lambert surface of equivalent total reflectance and the polarization of the light reflected from the desert sand surface itself. The maximum polarization of the outward directed light for the sand surface is ~8% more than that for the Lambert surface, and is shifted ~5° toward the nadir. There is no apparent shift in the neutral points (points of zero polarization) which may be a result of the small change in polarization in this region for the sand-reflected light.

The difference between the degree of linear polarization emerging from the top of a Rayleigh atmosphere overlying Mojave Desert sand and a Lambert surface of the same total reflectance as a function of nadir angle is shown in Fig. 13 for several wavelength and solar zenith angle combinations. The increasing values of the difference with increasing θ for $\lambda = 0.6$ μm and $\theta_0 = 0°$ agree with the trend in polarization shown in Fig. 4 for the desert sand. In a similar manner, the other curves in the figure follow the trend of the measured degree of polarization of light reflected from the desert sand. To place the differences of Fig. 13 in perspective for sensing from space, ground-based polarizing radiometers have been constructed that measure the degree of polarization to $\pm 0.1\%$, but a satellite-borne instrument will probably measure the degree of polarization to $\pm 1.0\%$ (Walraven, 1980).

The section on emergent radiance showed that the second term of Eq. (1) was dominant in transmitting the characteristics of the natural surfaces. The

second term and any term representing direct transmission out from the top of the atmosphere will not be polarized when reflection is from a Lambert surface. Approximating the polarization of the emergent light using the total emergent radiance for real surface reflection but only using the polarization introduced by the first and second terms gives close agreement with the results obtained when the polarization introduced by all the terms of Eq. (1) is used. For the three wavelengths the maximum difference in degree of polarization between the approximation and the rigorous case for Mojave Desert sand when $\theta_0 = 0°$ occurs at large θ and is 1.4%. If the polarization of the next important term, the fourth, is included in the approximation,

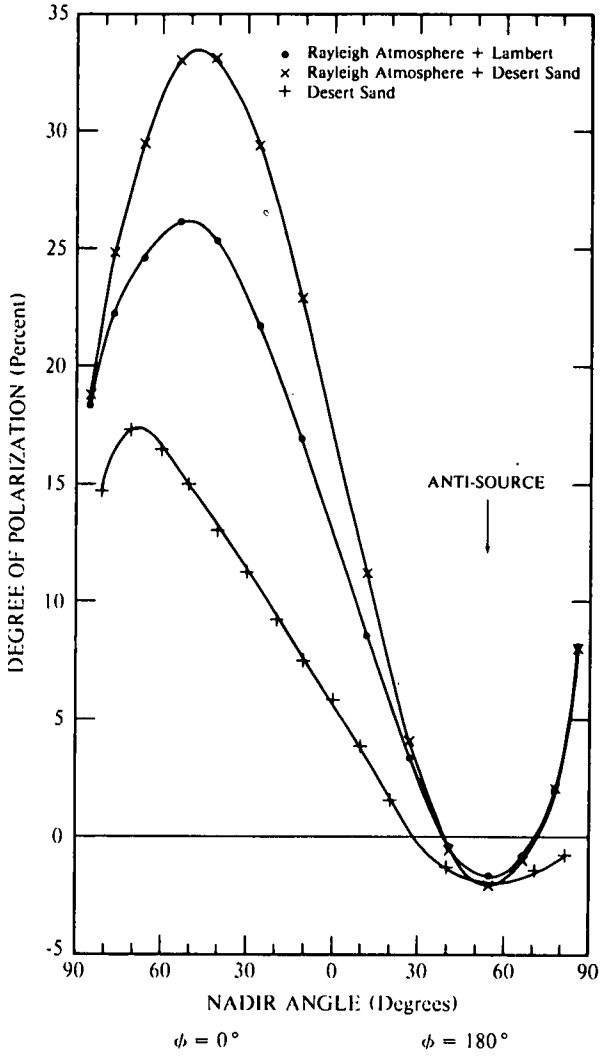

FIG. 12. A comparison of the degree of polarization of the light emerging from the top of a Rayleigh atmosphere overlying a Mojave Desert sand surface and its Lambert equivalent. Also shown is the degree of polarization of light reflected from the desert sand (principal plane, $\lambda = 0.5\ \mu m$, $\theta_0 = 53°$).

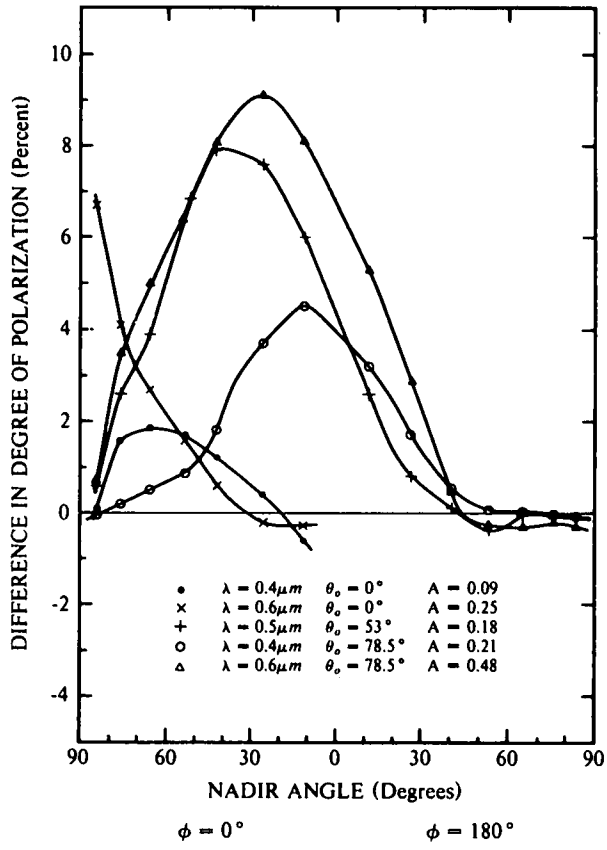

FIG. 13. The difference in the degree of polarization of the radiation emerging from the top of a Rayleigh atmosphere that occurs for reflection by Mojave Desert sand and its Lambert equivalent.

the maximum difference, as shown in column II of Table 2, is reduced to 0.2%. For solar zenith angles of 53 and 78.5° the maximum difference between the approximation and the rigorous case is reduced to a maximum of 0.3% if the third term of Eq. (1) is included in the approximation.

b. Results for a gypsum sand surface

Gypsum or white quartz sand is a highly reflecting surface, but the light reflected from the sand is not highly polarized. However, as shown in Fig. 14, there are significant departures of the degree of polarization from the Lambert case when the effects of the real polarizing surface are taken into account. For a wavelength of 0.4 and 0.6 μm when $\theta_0 = 0°$ the differences in degree of polarization increase with increasing values of nadir angle, except for $\theta > 75°$ and $\lambda = 0.4\ \mu m$ where the large optical thicknesses decrease the effect of the real surface. The importance of the fourth term is demonstrated by the decrease of the maximum difference from 1.8 to 0.2%, as shown in Table 2, when real surface reflection by this term is included in the approxima-

TABLE 2. The maximum difference (I) between the approximated and rigorously calculated values of polarization for the different atmosphere-surface models, and the maximum difference (II) when the next important term of Eq. (1) is included in the approximation.

Atmosphere	Surface	θ_0 (deg)	(I) Maximum difference (%)	(II) Maximum difference (%)	Added term
Rayleigh	desert sand	0	1.4	0.2	fourth
		53, 78.5	0.8	0.3	third
	gypsum sand	0	1.8	0.2	fourth
		78.5	0.5	0.2	third
	Yolo loam	0	0.8	0.05	fourth
		78.5	0.5	0.3	third
Turbid	desert sand	0	1.2	0.5	fourth
		78.5	1.4	0.3	third

tion. The influence of large optical depths is seen by comparing the curves in the $\phi = 0°$ plane for $\lambda = 0.4$ μm and $\lambda = 0.6$ μm when $\theta_0 = 78.5°$. The increased multiple scattering occurring for $\lambda = 0.4$ μm, compared to $\lambda = 0.6$ μm, masks the contribution of the real surface to the total polarization. For both wavelengths, however, the approximation works well, as shown in Table 2, showing the dominance of the first and second terms of Eq. (1) in contributing to the polarization.

c. Results for a Yolo loam surface

The polarization emerging from a Rayleigh atmosphere overlying the dark, but highly polarizing, Yolo loam surface is shown in Fig. 15 for $\lambda = 0.6$ μm and $\theta_0 = 0°$. The higher values of polarization for the atmosphere-loam model at $\theta > 30°$ compared to the atmosphere-Lambert model reflect the polarization characteristics of the loam in this region. In the region of the nadir, the negatively polarized light reflected by the surface introduces a neutral point for the atmosphere-loam model, whereas there was apparently none for the atmosphere-Lambert model.

The departures from the Lambert case caused by the highly polarizing Yolo loam surface are shown in Fig. 16 for a number of wavelength and solar zenith angle combinations. The shape and orientation of the curves with respect to one another are similar to the case of reflection by Mojave Desert sand (Fig. 13). However, unlike the other surfaces, Yolo loam shows a large negative difference in the region of the nadir for $\theta_0 = 0°$. This is due to the presence of large values of negative polarization of the reflected light in this region, as shown in Fig. 4. The approximation again, as shown in Table 2, works well in estimating the polarization of the light outward from the atmosphere overlying the loam.

7. Polarization outward from a turbid atmosphere

The polarization of the total radiance emerging from a turbid atmosphere is generally smaller than for a Rayleigh atmosphere as shown in Fig. 17 for the Mojave Desert sand surface. The wavelength is 0.6 μm and the zenith angle of the sun is 78.5°. Also compared in the figure are the polarization curves of the light emerging from the turbid atmosphere overlying the desert sand and its equivalent Lambert surface. Both curves show the existence of the neutral point (Arago) at $\phi = 0°$. The point is predicted for Rayleigh scattering alone when values of θ_0 are large but its occurrence was probably suppressed

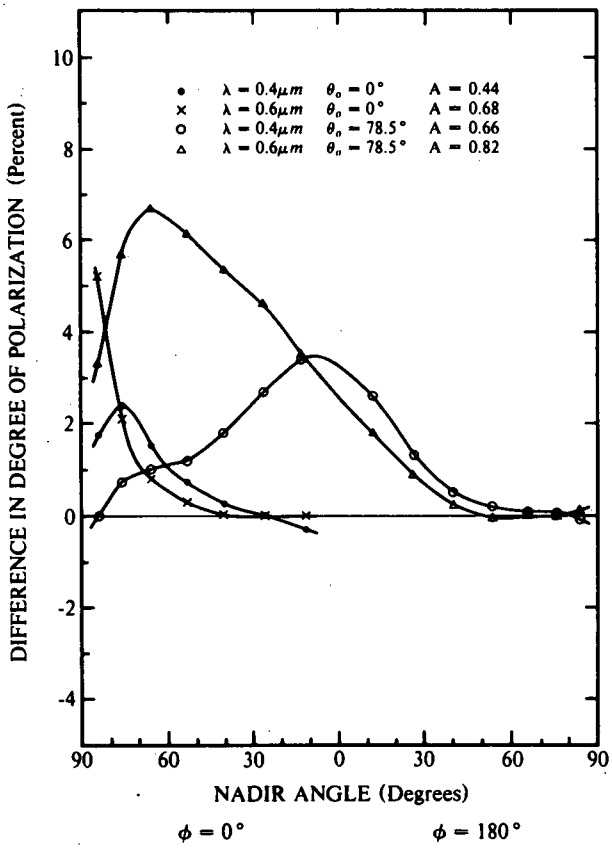

FIG. 14. The difference in the degree of polarization of the radiation emerging from the top of a Rayleigh atmosphere that occurs for reflection by gypsum sand and its Lambert equivalent.

because of the large contribution of positive polarization by the desert sand in the $\phi = 0°$ plane. It is interesting that the differences in polarization between the curves for the turbid and Rayleigh atmospheres overlying desert sand can be as large as the differences occurring between the curves for the turbid atmosphere overlying the sand and the Lambert surface.

The difference in degree of polarization as a function of nadir angle between real surface and Lambert surface reflection is presented in Fig. 18 for turbid and Rayleigh atmospheres overlying Mojave Desert sand. For angles $\leq 70°$ and $\theta_0 = 0°$ the differences in polarization for the turbid atmosphere are close to those for the molecular atmosphere. At larger nadir angles the two cases diverge from one another, a result of an increase in multiple scattering. At a solar zenith angle of 78.5° the effect of the turbid atmosphere in reducing the departures from Lambert

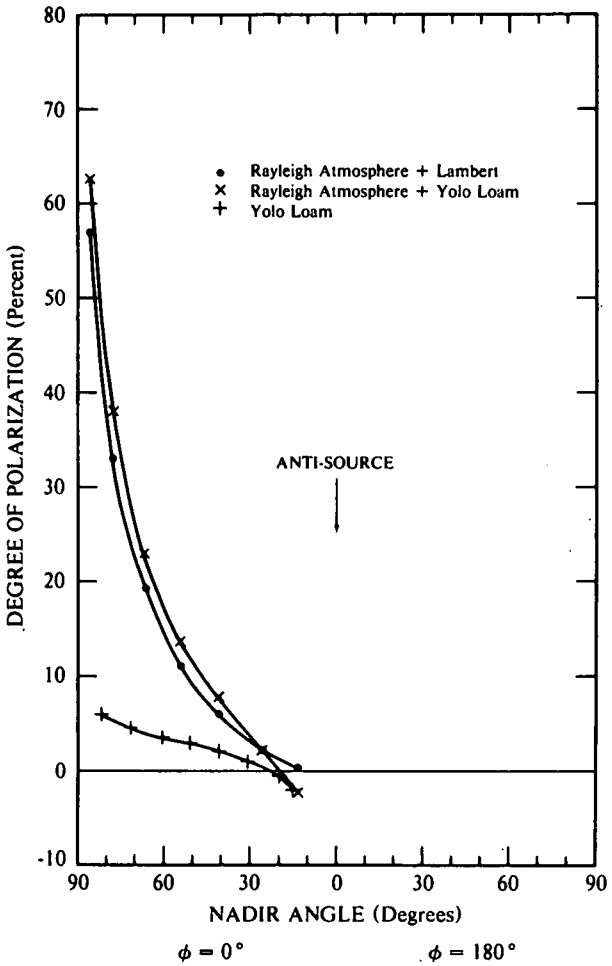

FIG. 15. A comparison of the degree of polarization of the light emerging from the top of a Rayleigh atmosphere overlying a Yolo loam surface and its Lambert equivalent. Also shown is the degree of polarization of light reflected from the loam (principal plane, $\lambda = 0.6$ μm, $\theta_0 = 0°$).

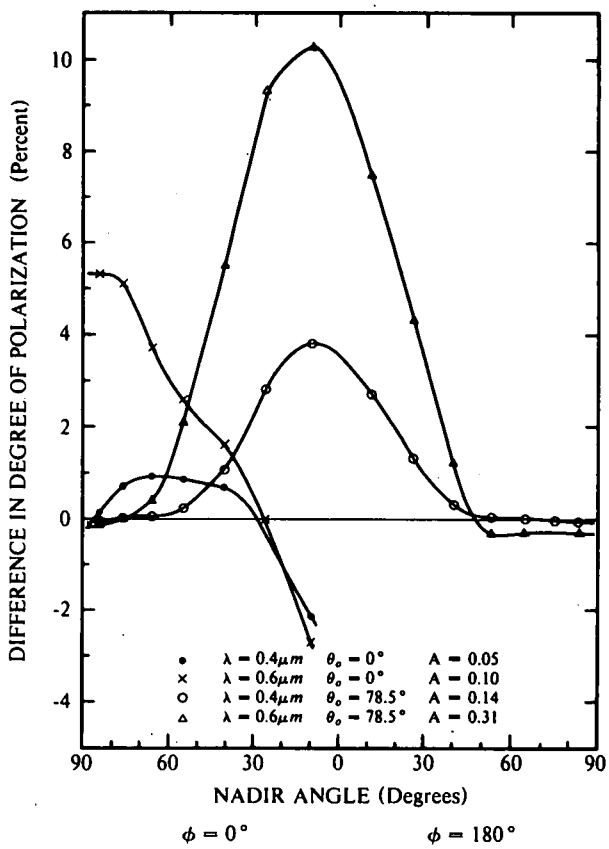

FIG. 16. The difference in the degree of polarization of the radiation emerging from the top of a Rayleigh atmosphere that occurs for reflection by Yolo loam and its Lambert equivalent.

are large compared to the Rayleigh atmosphere. The departures from Lambert for the turbid atmosphere, however, are still significantly large. The increased importance of the terms of Eq. (1) with histories of diffuse transmission are evident by the large differences occurring (shown in Table 2) for a turbid atmosphere overlying desert sand. With the addition of either the third or fourth terms, however, the approximation of the polarization is greatly improved.

8. Conclusions

The surfaces used in this study represent a variety of reflection characteristics from the Lambert-like gypsum sand to the highly anisotropic polarizing Yolo loam. The calculations support the following conclusions:

1) The radiance emerging from the top of a Rayleigh atmosphere can be significantly different for a real surface compared to its Lambert equivalent and the difference, in general, increases as the solar zenith angle and the wavelength increase.

2) The surface reflection characteristics are carried mainly by the second term of Eq. (1). This fact

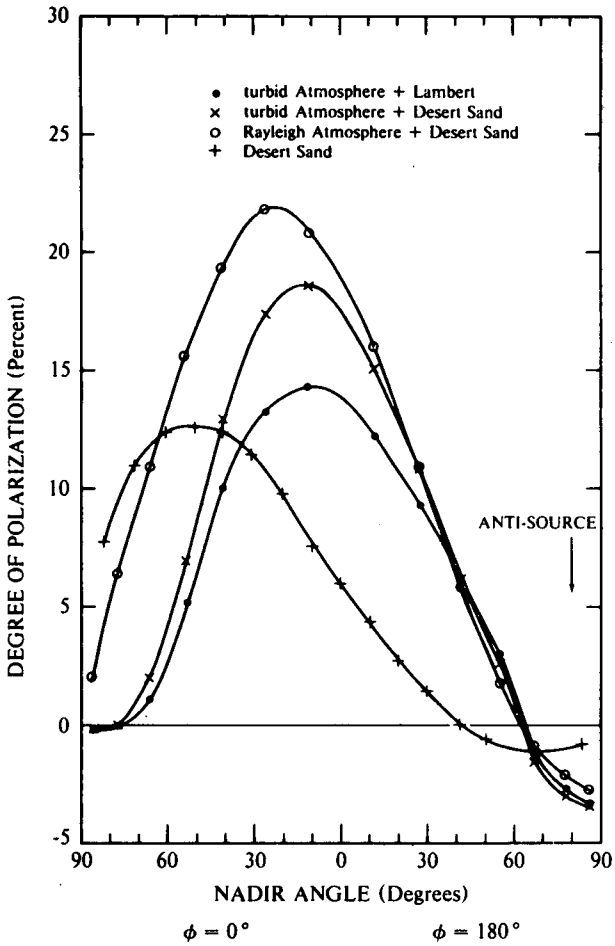

FIG. 17. A comparison of the degree of polarization of the light emerging from the top of the turbid atmosphere plus desert sand, Rayleigh atmosphere plus desert sand, and turbid atmosphere plus Lambert surface models. Also shown is the degree of polarization of light reflected from the desert sand (principal plane, $\lambda = 0.6\ \mu m$, $\theta_0 = 78.5°$).

has been used by Coulson *et al.* (1966) and Tanre *et al.* (1979) to simplify their calculations.

3) The third term is of next importance; its influence in the region of the nadir can exceed that of the second term at the shorter wavelengths and larger solar zenith angles.

4) The increased multiple scattering of the turbid atmosphere decreases the importance of including the characteristics of real surface reflection in calculating the emergent light. The maximum correction, however, may reach 3.0% for $\lambda = 0.4\ \mu m$ and $\theta_0 = 0°$ or 78.5° and more than 10% for $\lambda = 0.6\ \mu m$ and $\theta_0 = 78.5°$.

5) The Lambert approximation works well in the range $\theta = 40–45°$, $\phi = 0°$ for all of the atmosphere-surface combinations studied. It may be possible to use the radiance measured in this range to normalize the entire radiance field producing a representation of the non-Lambertian reflection characteristics of the surface.

6) Large differences can occur between the degree of polarization of radiation emerging from the top of a pure molecular atmosphere overlying a natural as compared to a Lambert surface. The profiles of these differences are directly related to the curves of polarization of the light reflected by the surfaces. As was the case with radiance, the departures of the polarization from the Lambert case are largest for the larger solar zenith angles and wavelengths.

7) The degree of polarization of the light emerging from the top of the Rayleigh atmosphere overlying a real surface can be approximated to an uncertainty of 0.3% or less by including real surface reflection in only the second and either the third or fourth terms of Eq. (1).

8) Compared to a Rayleigh atmosphere the differences in polarization are smaller for the turbid atmosphere, but they are still significant. Again, the polarization of the emergent light can be accurately approximated, in this case to 0.5% or less, by using only the second and either the third or fourth terms of Eq. (1).

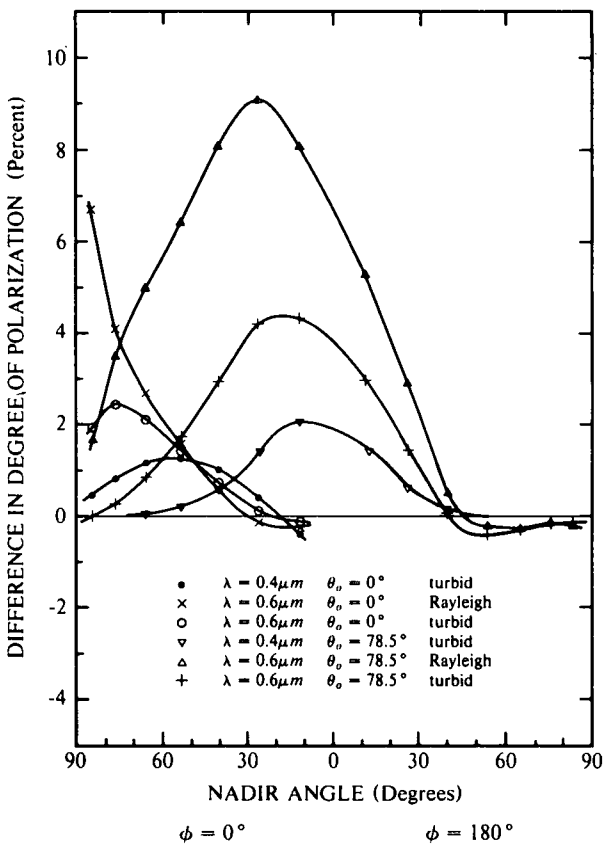

FIG. 18. The difference in the degree of polarization of the radiation emerging from the top of Rayleigh and turbid atmospheres that occurs for reflection by Mojave Desert sand and its Lambert equivalent.

There are surprisingly large departures in the polarization of radiation emerging from the top of the Rayleigh and turbid atmospheres for a real as compared to a Lambert surface. These departures show that there is a significant amount of information about the real polarizing surface in the polarization of the emergent light. Polarization appears to be a very good parameter for obtaining additional information about the features of a natural ground surface.

This work needs to be extended into several areas. One area is the study of how much large-scale topographic relief will reduce the effect of real surface reflection on the emergent radiation. In addition, the study of the effects of a surface composed of two or more distinct surface types is of interest.

Acknowledgments. It is my pleasure to thank Prof. Kinsell L. Coulson for the many constructive discussions we had. I also wish to thank Dr. Robert Walraven for his helpful comments and suggestions. Dr. Tsutomu Takashima generously made his program available to model the inhomogeneous atmosphere. The phase functions describing the aerosol were graciously provided by Dr. Robert Fraser. The aid of Mr. Keith Grant is gratefully acknowledged. Computer time was kindly provided by the Atmospheric and Geophysics Division of Lawrence Livermore Laboratories. The support for this investigation, which was provided by the National Science Foundation under Grants DV40893, DPP76-22260 and DPP77-19362, and by the Air Force Geophysics Laboratory under Contract F19628-78-C-0200, is gratefully acknowledged.

REFERENCES

Chandrasekhar, S., 1960: *Radiative Transfer.* Dover, 393 pp.

Coulson, K. L., E. L. Gray and G. M. B. Bouricius, 1966: Effect of surface reflection on planetary albedo. *Icarus*, **5**, 139–148.

Deirmendjian, D., 1969: *Electromagnetic Scattering on Spherical Polydispersions.* Elsevier, 290 pp.

Hovenier, J. W., 1969: Symmetry relationships for scattering of polarized light in a slab of randomly oriented particles. *J. Atmos. Sci.*, **26**, 488–499.

Koepke, P., and K. T. Kriebel, 1978: Influence of measured reflection properties of vegetated surfaces on atmospheric radiance and its polarization. *Appl. Opt.*, **17**, 260–264.

Takashima, T., 1974: Method of computing the effect of surface reflection on the atmospheric radiation. *Publ. Astron. Soc. Japan*, **26**, 361–366.

Tanre, D., M. Herman, P. Y. Deschamps and A. de Leffe, 1979: Atmospheric modeling for space measurements of ground reflectances, including bidirectional properties. *Appl. Opt.*, **18**, 3587–3594.

Walraven, R. L., 1980: Polarization imagery. *Opt. Eng.*, **20**, 14–18.

Wolff, M., 1975: Polarization of light reflected from rough planetary surface. *Appl. Opt.*, **14**, 1395–1405.

Reprinted from JOURNAL OF APPLIED METEOROLOGY, Vol. 20, No. 10, October 1981
American Meteorological Society
Printed in U. S. A.

Measurements of Aerosol Size Distributions in the Lower Troposphere over Northern Europe

BRUCE W. FITCH

Visibility Laboratory, Scripps Institution of Oceanography, University of California, San Diego, 92093

TED S. CRESS[1]

Air Force Geophysics Laboratory, Hanscom AFB, MA 01731

(Manuscript received 11 November 1980, in final form 23 June 1981)

ABSTRACT

Airborne measurements of particle size distributions were made at several altitudes within and above the mixing layer at sites near Ahlhorn and Meppen (West Germany), Rodby (Denmark), and Bruz (France). The distributions were measured over the range 0.2–5.9 μm in particle radius using a Royco model 220 particle counter. The experimental data gathered at the sites were analyzed in terms of volume-size distributions instead of the commonly used particle number distributions. The volume distribution plots were found to be bimodal with the accumulation mode centered at a mean radius in the range 0.26–0.49 μm and the coarse particle mode existing beyond 1.0 μm. The data show the accumulation mode is well defined by a log-normal distribution. The values of the measured volume scattering coefficient and mean particle radius of the accumulation mode increase as the maximum particle volume of the mode increases. The existence of an accumulation mode was almost always confined to the mixing layer. It is interesting that haze layers above the mixing layer were found to have a distinct coarse particle mode but, generally, no distinct accumulation mode. The total concentration of particles in each of the two modes appear related for larger values of concentration in the coarse particle mode.

1. Introduction

Sophisticated numerical techniques have been developed by a number of investigators, including Dave (1978) and Takashima (1975), to solve for the radiation emerging from an atmosphere. These investigators and others, however, must in some way rely upon a knowledge of the size distribution of the atmospheric aerosol as a function of altitude, season, and location. The size distributions frequently used are the haze models of Deirmendjian (1969), who used a modified gamma function; the power-law size distribution function of Junge (1963); or a log-normal distribution as described by Aitchison and Brown (1957). Generally, the shape of the distribution is held constant while only the particle concentration changes with altitude.

There are few measurements to support the use of these model size distributions. A series of airborne measurements were made by Blifford and Ringer (1969), who collected aerosol samples in the central United States during 1966 at altitudes from 0.3 to 9 km above the ground. A majority of the samples, 22 of them, were acquired near Scottsbluff, Nebraska. Sampling of the troposphere has also been conducted by Laulainen *et al.* (1978). To augment these data and increase our understanding of the atmospheric aerosol content, an extensive measurement program was conducted in the lower troposphere at seven sites in northern Europe and Great Britain during each of the four seasons. This report presents the results of analysis of some of these data.

2. Method of measurement

Aircraft measurements of the number and size distribution of the atmospheric aerosol were conducted along tracks of constant altitude above the ground near Bruz (France), Rodby (Denmark), Ahlhorn and Meppen (W. Germany) during the spring and fall of 1976 and the summer of 1977. All of the 50 km long sampling tracks, the locations of which are shown in Fig. 1, were over land, except for the Rodby track which was over the Baltic Sea. These airborne aerosol measurements, described by Cress (1980),[2] were part of a larger atmospheric optical measurement program (Duntley *et al.*, 1978)[3] conducted under

[1] Present affiliation: Air Force Office of Scientific Research, Bolling AFB, Washington, DC 20332.

[2] Cress, T. S., 1980: Airborne measurements of aerosol size distributions over northern Europe, Vol. 1. Rep. AFGL-TR-80-0178, Air Force Geophysics Laboratory, 124 pp.

[3] Duntley, S. Q., R. W. Johnson and J. I. Gordon, 1978: Airborne measurements of optical atmospheric properties, summary

0021-8952/81/101119-10$06.50

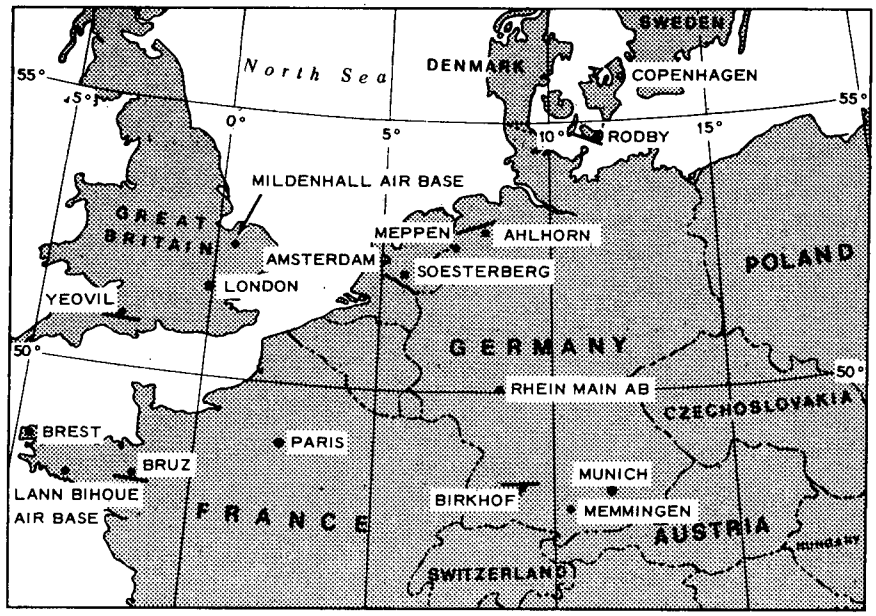

FIG. 1. Location of the ground-base data sites (circles) and the aircraft tracks (line segments).

the sponsorship of the Air Force Geophysics Laboratory.

Sampling was performed in cloud-free air at altitudes from ~150–6100 m above the surface. The altitudes varied from one flight to another because of changes in cloud height and mixing layer depth. Whenever possible, two samples were made at different altitudes within the mixing layer and two more above. The mixing layer was generally capped by an inversion layer. The sampling time of the Royco was typically 4 min, but occasionally samples were taken for 1 min or as long as 10 min, depending on the situation and the density of particles being counted. A single flight required from 30 min to 220 min depending on the number of altitudes flown.

The instrumentation on the C-130 aircraft included a Royco 220 single particle counter and an integrating nephelometer. Sample air for the Royco was provided by a ram air isokinetic sampling probe located on top of the C-130 fuselage with the probe entrance 33 cm above the aircraft skin and 45 cm to the right of the radome which housed the nephelometer. The entire Royco system consisted of the Royco counter, a Technical Measurement Corporation Model 102 Gamma Scope II Pulse Height Analyzer, and a Hewlett-Packard Clock/Printer. The electronics of the analyzer were adjusted to position the counting of 0.4 μm radius size particles in channel 18 of the total 89 channel range covering particle sizes 0.2 to 5.9 μm.

The Royco is a right-angle scattering counter that was calibrated with submicrometer size polystyrene spheres. The operating characteristics of this instrument have been the subject of a number of investigations including those of Quenzel (1969), Liu *et al.* (1974), and Cooke and Kerker (1975). The two fundamental sources of error result from an inadequate knowledge of the index of refraction of the ambient aerosol and modifications to the particle size distribution which may occur in the plumbing between the ambient air and the counter.

Investigations by Cooke and Kerker (1975) and Quenzel (1969) have demonstrated that significant errors in the determination of particle size can occur when the refractive index m of the particles is not known. Assuming a calibration with polystyrene-latex spheres ($m = 1.58-0i$), Quenzel ($= 1.33-0i$) or an average atmospheric aerosol ($m = 1.50-0i$) is used, the sizing error is less than a ($m = 1.95-0.66i$) over the range of particle radius 0.1–3.0 μm. If the refractive index of water ($m = 1.33-0i$) or an average atmospheric aerosol ($m = 1.50-0i$) is used, the sizing error is less than a factor of 2.0. A value of $m = 1.50-0.02i$, that includes absorption, produced a sizing error that increased with increasing particle radius. The magnitude of the error was difficult to determine from Fig. 2 of Quenzel (1969) but its maximum is estimated to be in the range 2 to 3. A ground based intercomparison study between a Royco 220 and active and classical Particle Measurement Systems

and review III. Rep. AFGL-TR-78-0286, Visibility Laboratory, University of California, San Diego, Scripps Institution of Oceanography, La Jolla, 108 pp. [NTIS AD A073121].

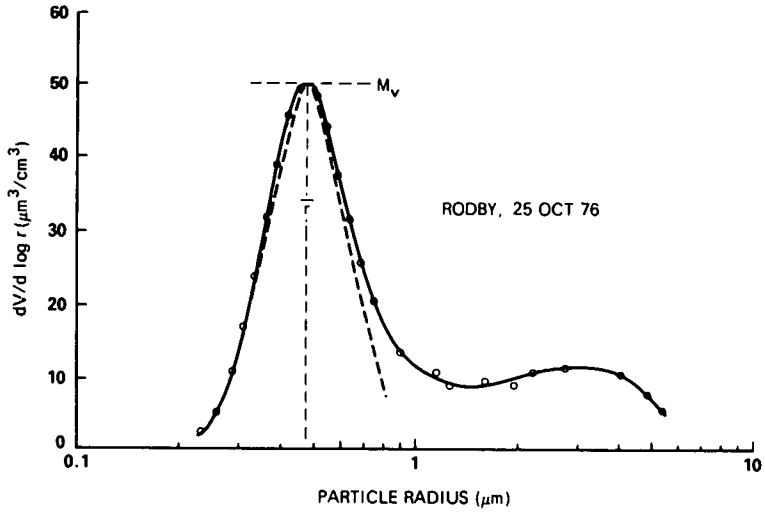

FIG. 2. The aerosol volume per increment d log$r$ as a function of particle radius for data taken at Rodby (Denmark) on 25 October 1976 at an altitude of 305 m above the sea surface (solid line). The mode radius $\bar{r}$ and maximum M_v of the volume distribution accumulation mode are shown. A log-normal distribution with $\bar{r} = 0.45$ μm and standard deviation $\sigma = 0.13$ is shown (dashed line) for comparison.

aerosol counters showed agreement to within a factor of 2 to 5 in particle concentration (Cress and Fenn, 1978).[4]

The physical properties of the ambient aerosol sample may have been modified in its passage from outside the aircraft to the Royco scattering chamber. Comparison of consecutive 1 min data samples, however, indicate that the repeatability of the airborne Royco was good. The flow rate was approximately 47 cubic centimeters per second. Possible modifications to the aerosol sample may be a result of a drying of the particles or a selective loss of particles. The small number of changes in the direction of flow within the plumbing probably minimized the effects of particle loss. This is supported by the good agreement between this data set and the impactor data of Blifford and Ringer (1969) as shown by Cress.[2] The aerosol measurements most likely represent a low humidity or dry particle distribution because some evaporation probably occurred in the plumbing. The shape of the distribution was probably preserved due to the small size range measured. These sources of error are discussed in greater detail by Cress.[2]

The integrating nephelometer, described by Duntley *et al.*,[3] measures the volume scattering coefficient s over the range of scattering angle 5° to 170° and the scattering coefficient at 30° and 150°. The nephelometer operated at the photopic and in narrow wavelength bands centered at 0.478, 0.664 and 0.765 μm. Calibration using dry nitrogen and comparisons with an Eltro transmissometer indicate that the accuracy of the volume scattering coefficient is within 20% (Duntley *et al.*, 1976).[5]

3. Results of measurements

Traditionally, size distribution data have been presented in figures of log(dN/d log$r$) versus log$r$, where r is the particle radius and N is the total number density of particles smaller than r. A presentation of this type has been found to mask the multimode nature of distributions that appears when the data are plotted as volume (or mass) versus particle size, as pointed out by Whitby *et al.* (1972) and Shettle (1975). For this reason it was decided to use the volume size display in this analysis.

A plot of dV/d log$r$ versus log$r$ for the measurements taken at Rodby on 25 October, 1976 at an altitude of 305 m above the sea surface is shown in Fig. 2. Values of the total particulate volume, dV/d log$r$, over an increment d log$r$ are shown in the figure by circles for a few of the 89 data channels. The solid curve represents a fit to the data of all the channels. The inversion height was about 700 m in this case as determined from temperature profile measurements made concurrently with the Royco

[4] Cress, T. S. and R. W. Fenn, 1978: OPAQUE aerosol counter intercomparison 25 April 1977–4 May 1977. Rep. AFGL-TR-78004, Air Force Geophysics Laboratory, 56 pp.

[5] Duntley, S. Q., R. W. Johnson and J. I. Gordon, 1976: Airborne measurements of optical atmospheric properties in Northern Germany. Rep. AFGL-TR-76-0188, Visibility Laboratory, University of California, San Diego, Scripps Institution of Oceanography, La Jolla, 221 pp. [NTIS AD A031496].

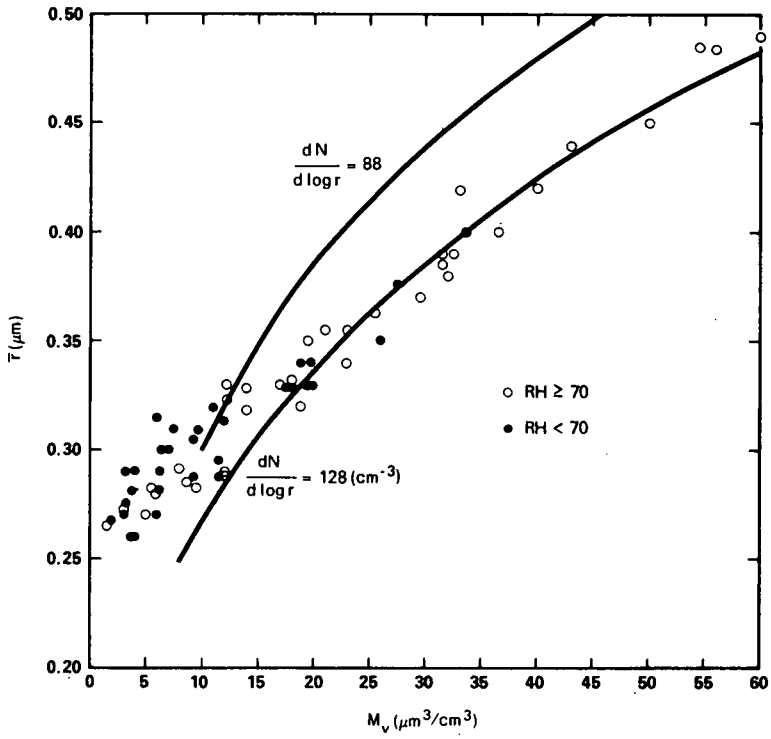

FIG. 3. The mode radius $\bar{r}$ as a function of the maximum volume M_v for all the data collected within the mixing layer. Curves of $dV/d\log r$ for constant particle number density $dN/d\log r$ (solid lines) show the $\bar{r}^3$ dependence of M_v. Data for which the relative humidity is greater than or equal to 70% are indicated by the open circles.

measurements and from estimates of the surface haze layer thickness made by an on-board observer. The curve, shown in Fig. 2 centered about the radius 0.45 μm, is closely approximated by a log-normal curve (dashed line). The symmetry and shape of the data curve is typical of the analytical data. Whitby (1978) termed this the accumulation mode and stated that its main source of mass is from the coagulation of the smaller size aerosols and from gas to particle conversion. The peak in the curve at about 3 μm indicates the presence of the coarse particle mode, which according to Whitby (1978) generally results from mechanical processes such as those that create wind-blown dust or sea spray.

a. Accumulation mode

For this study the accumulation mode is modeled by the value of the mode radius $\bar{r}$ the standard deviation σ, and M_v—the value of $dV/d\log r$ occurring at the mode radius. Values of M_v are plotted against those of $\bar{r}$ in Fig. 3 for all of the seasons, stations, and altitudes below the inversion height that were available for this study. Values of $M_v > 40$ μm^3 cm^{-3} represent data collected only at Rodby during the winter. The figure shows values of M_v increasing with values of $\bar{r}$. Increasing values of M_v do not necessarily imply, however, that the particle number is increasing. Also shown in the figure are curves of $dV/d\log r$ for constant particle number, $dN/d\log r$, which illustrates the r^3 dependence inherent in the volume size distribution. For values of $\bar{r} < 0.34$ μm there is an increase in the measured particle number with increasing $\bar{r}$. For values of $\bar{r} > 0.34$ μm, however, the particle number appears to be constant with increasing values of $\bar{r}$. The data presented in Fig. 3 suggest that there is a functional relationship between $\bar{r}$ and M_v. This relationship will be more fully explored for different air mass types using the complete set of Royco measurements. Plots comparing σ, which range in value from 0.08 to 0.20, with values of both M_v and total particle volume V of the mode show no discernible relationship between these parameters. This is probably due to the sensitivity of the determination of σ to the fitting procedure. In order to more easily visualize the character of the accumulation mode and to simplify its log-normal description, the value $M_v = V/\sigma(2\pi)^{1/2}$ is used for the analysis of this mode.

There does not appear to be a clear dependence on relative humidity as measured with a Cambridge Model 137-C3 aircraft hygrometer system. The open

circles, representing cases where the relative humidity was greater than or equal to 70%, predominate at the larger radii as shown in Fig. 3. This apparent dependence on relative humidity, however, is mainly due to a small data sample taken at Rodby in an unusually heavy haze. If this Rodby data is neglected from the figure, then any tendency for the relative humidity to be $\geq 70\%$ when the value of the mode radius is ≥ 0.34 μm is probably not significant. There is a probability level of ~ 0.05 that the value of chi square will be equalled or exceeded by a random sample. If values greater than or equal to 80% are considered there again appears to be no clear dependence on relative humidity. This lack of a clear dependence on relative humidity may be a result of drying of the aerosol in the intake plumbing.

In addition to measurements of the aerosol size distribution, the volume scattering coefficient s at $\lambda = 0.664$ μm was also measured. The scattering coefficient may be expressed as

$$s = \pi \int_{\log r_1}^{\log r_2} Q_s(m, x) r^2 \frac{dN}{d \log r} d \log r,$$

where $x = 2\pi r/\lambda$ is the size parameter of a spherical particle, $Q_s(m, x)$ is the efficiency factor for scattering (Van de Hulst, 1957), and r_1 and r_2 are the lower and upper limits of the particle radii under consideration. The relationship between s and the model parameters can be shown by using a log-normal description of the aerosol volume distribution and the expression $dV/d \log r = \frac{4}{3} \pi r^3 (dN/d \log r)$. After simple manipulation, s can be written in the form

$$s = \frac{3}{4} \int_{\log r_1}^{\log r_2} Q_s(m, x) r^{-1} M_v \times \exp\{-0.5[(\log r - \log \bar{r})/\sigma]^2\} d \log r. \quad (1)$$

Even though the Royco is sensitive to a narrower particle size range than the nephelometer, calculations show that the distribution below 0.4 μm, typically, adds $<15\%$ to the total scattering at $\lambda = 0.455$ μm. At the wavelength 0.664 μm this percent contribution is even smaller, so the results of measurements by the Royco and the nephelometer should, as seen in Eq. (1), be strongly related.

Values of the volume scattering coefficient s for the wavelength 0.664 μm are plotted in Fig. 4 as a function of M_v. Though values of s are not uniquely dependent upon values of M_v, as seen in Eq. (1), the figure does show a trend of increasing s with increasing M_v. This trend can be explained by a shift in the volume distribution to larger radii for constant particle number, which increases M_v, and by increases in particle number which occur at the smaller values of M_v as shown in Fig. 3. The scatter in the data, in part, is a result of the fact that s was not always

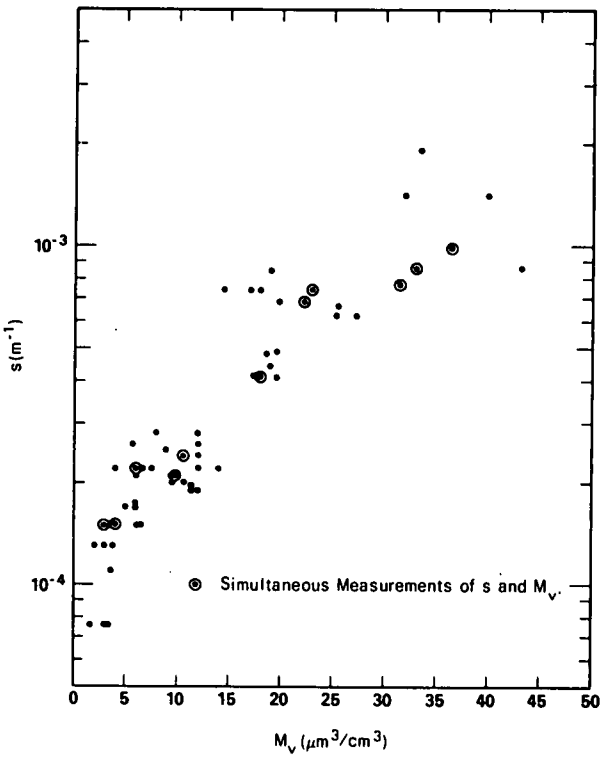

FIG. 4. The volume scattering coefficient s for the wavelength 0.664 μm as a function of the maximum volume M_v. Cases were s and M_v were measured simultaneously are circled.

measured simultaneously with M_v. At times there was a two to three hour difference between the measurements. There is an apparent decrease in the scatter of the data when simultaneous measurements of s and M_v are plotted (circled data points). Some residual scatter can be expected due to the effects of variations in relative humidity which were detected by the nephelometer but probably not by the Royco due to drying in the intake plumbing.

In five of the flights studied, the air was so clear and the particle counts so low that there was no distinct accumulation mode measured at altitudes below the inversion height. All of these cases occurred during the winter season at Bruz, Rodby and Meppen and, in all but one case, the air mass type was maritime. The average meteorological range, as estimated by the on-board observer, was always >14 km. The values of $dV/d \log r$ at 0.3 μm were rarely >2 μm^3 cm^{-3} (corresponding to a measured V over the range of the mode of <1 μm^3 cm^{-3}) and s measured for the 0.664 μm band was $<6.8 \times 10^{-5}$ m^{-1}. These values of $dV/d \log r$ and s are in agreement with the general trend of the data in Fig. 4, even though no value of M_v could be determined for these five cases.

To investigate the variation of M_v with respect to altitude, values of M_v were plotted against the ratio

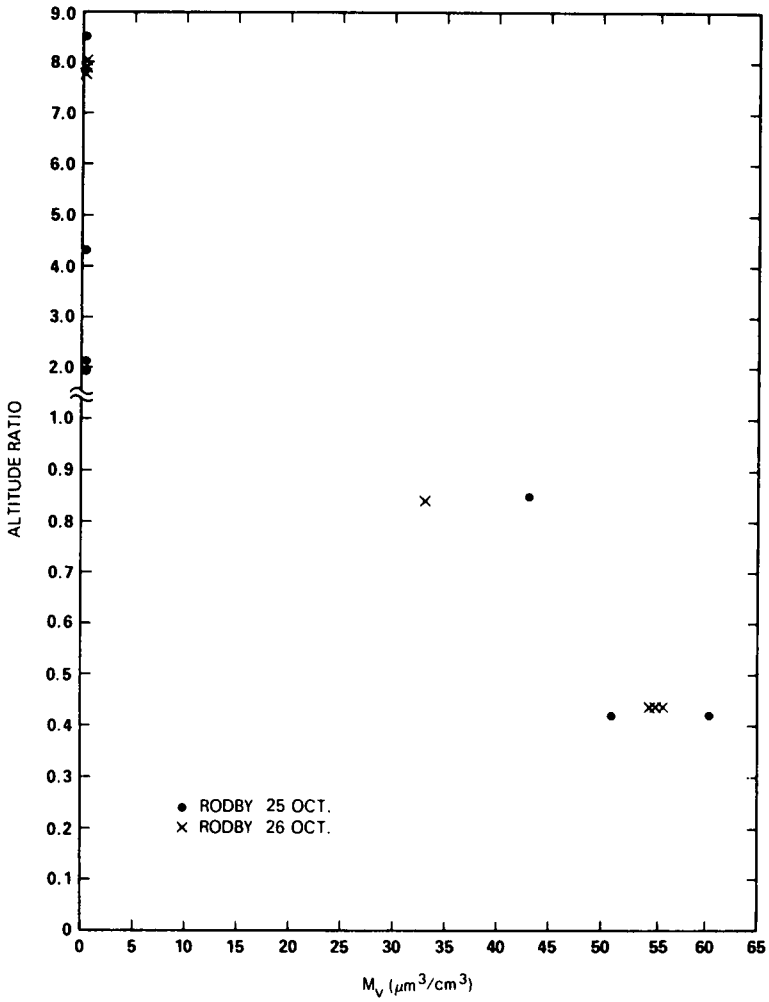

FIG. 5. The maximum volume in the accumulation mode M_v measured at Rodby on 25 October 1976 (circles) and on 26 October 1976 (crosses) as a function of altitude ratio, the ratio of the aircraft altitude during measurement to the thickness of the mixing layer.

of the measurement altitude to the altitude of the inversion base. Data taken at Rodby on 25 and 26 October are presented in Fig. 5. In the mixing layer—an altitude ratio of <1.0—the values of M_v decrease with increasing altitude for both days. For ratios > 1.0 (note the change of scale) the values of M_v are near zero.

All of the flights investigated show small values of M_v at altitude ratios of >1.0. The decrease in M_v with increasing altitude in the mixing layer, however, is not always present. The results of measurements made at Bruz on 4 and 7 July are presented in Fig. 6. There is a decrease in the values of M_v with increasing altitude in the mixing layer for the 7 July data but not for the 4 July data, which appears invariant with altitude. The temperature profile to an altitude ratio of 0.4 shows 7 July as more thermally stable than 4 July at the time of the aerosol measurements. From the altitude 0.4 to 1.0 the temperature profile for both days was close to the dry adiabatic lapse rate. In addition, below the altitude ratio 0.4 the temperatures for 4 July were larger than those for 7 July. This is probably because the 7 July data was taken in the morning and the 4 July data was collected in the afternoon. The scatter in the 7 July data at the low altitude ratios is in part a result of the time required to take these data, ~3.5 h. In contrast, three measurements made at Bruz on 6 July over a 4 min period at an altitude ratio of 0.3 show M_v ranging from only 15–18 μm^3 cm^{-3}.

b. Coarse particle mode

Very often, low particle counts were measured in the size range of the coarse particle mode. These low

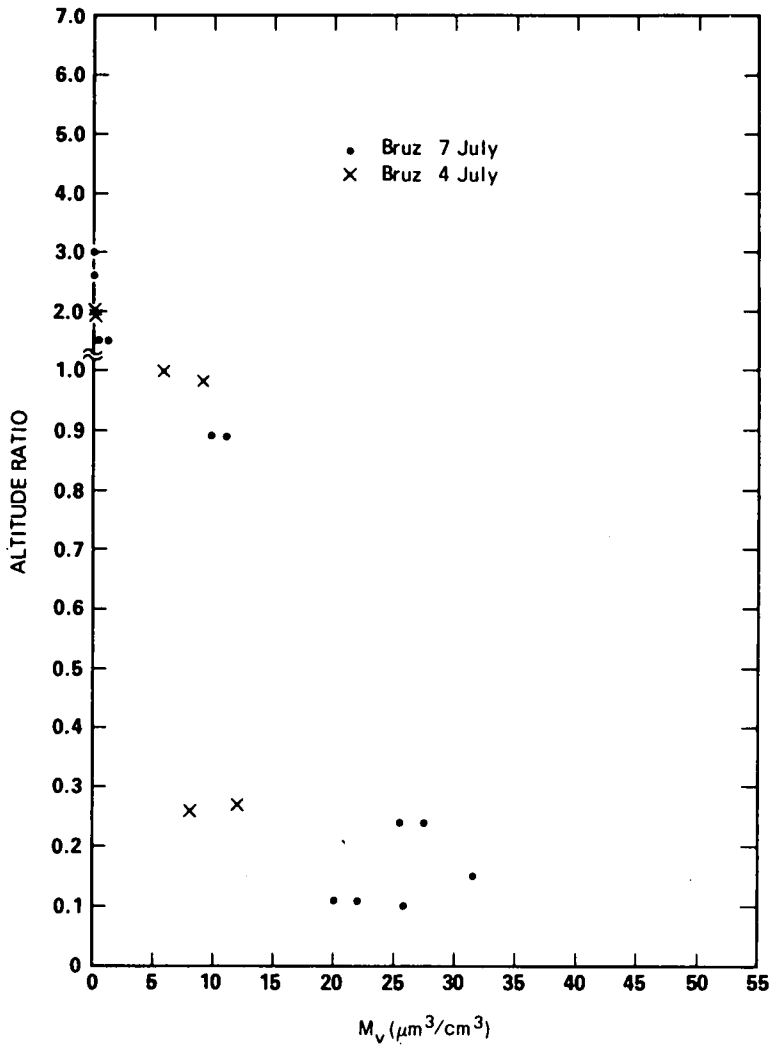

FIG. 6. The maximum volume in the accumulation mode M_v as a function of altitude ratio for data collected at Bruz on 7 July 1977 (circles) and on 4 July 1977 (crosses).

counts made it difficult to determine values of the model parameters M_v, σ and $\bar{r}$ for this mode. Consequently, the coarse particle mode was represented by the integrated volume concentration V of particles from particle radius 2.0 to 5.7 μm. A plot of V versus the altitude ratio for Bruz on 4 and 7 July is shown in Fig. 7. Within the mixing layer, the values of V decrease with increasing altitude for both days. Above the mixing layer, the increase in the values of volume concentration with increasing altitude ratio indicate the presence of a second haze layer. The on-board observer confirmed the existence of this second haze layer. It is interesting that there is no indication of a second haze layer in the accumulation mode data of Fig. 6. When there was no second haze layer above the mixing layer, the trend of V and M_v with altitude was similar.

The relationship between M_v of the accumulation mode and V of the coarse particle mode is represented in Fig. 8, which includes all the analyzed data from the mixing layer. The total volume concentration based on a log-normal fit to the accumulation mode can be determined by using the expression $V = M_v\bar{\sigma}(2\pi)^{1/2}$ where the average $\bar{\sigma}$ for the data set is 0.11. Values of volume concentration greater than 3.5 $\mu m^3\ cm^{-3}$ represent data from Rodby (25 and 26 October) taken in a saturated layer caused by the warm water of the Baltic and strong winds. The connected values in Fig. 8 show the variations that can occur over 2–3 h at a given site and altitude. The set of data points occurring at $M_v > 15$ $\mu m^3\ cm^{-3}$ and $V < 1.0\ \mu m^3\ cm^{-3}$ are from two flights conducted on 4 August at the Meppen site. During the measurements, the air mass was classified as

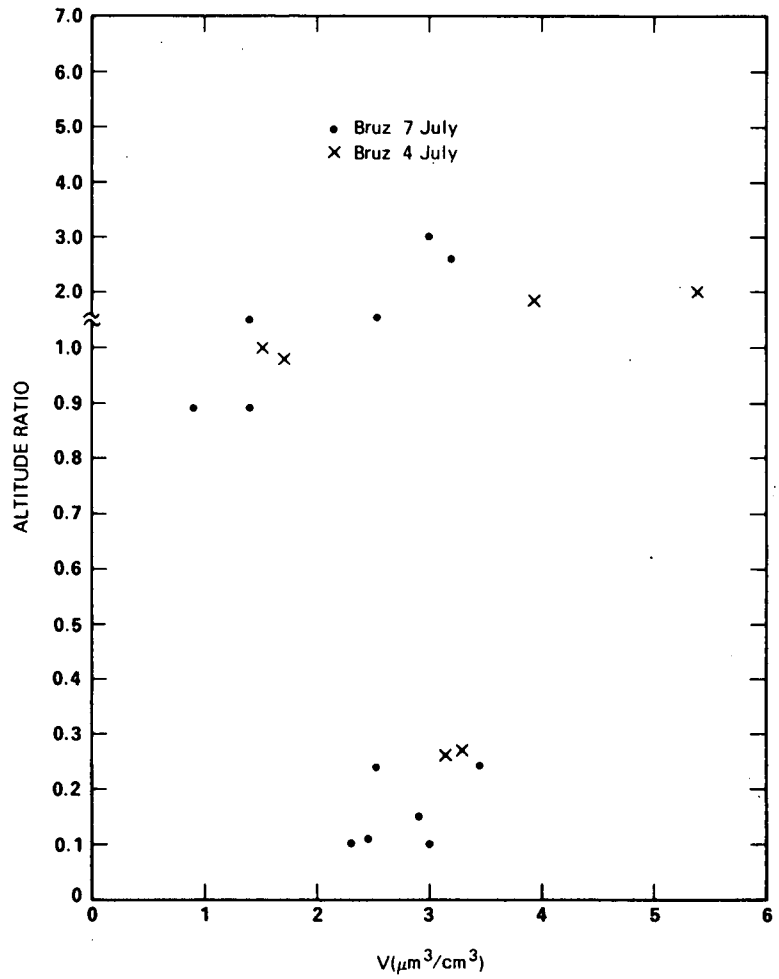

FIG. 7. The volume concentration of particles in the coarse particle mode V as a function of altitude ratio for data collected at Bruz on 7 July 1977 (circles) and on 4 July 1977 (crosses).

stagnant with ground stations in the area reporting haze, and winds < 4 m s^{-1}. The data in Fig. 8 indicate that values of M_v generally increase with values of V, except for the 4 August data. The increase, however, is strongly dependent on only two days of data from Rodby. It probably represents the effect of different air mass types on values of V and M_v and not the effect of a correlation between the two parameters. According to Whitby (1978), the two modes have different source and production mechanisms, so no strong correlation need exist between the two modes.

4. Discussion and conclusions

Aircraft measurements of particle size distributions were made at several altitudes within and above the mixing layer at sites near Ahlhorn and Meppen (W. Germany), Rodby (Denmark) and Bruz (France). The experimental information gathered at the sites was analyzed in terms of volume-size distributions instead of the standard particle number distributions. The data support the following conclusions for the aerosol characteristics at the measurement sites:

1) There are at least two distinct modes comprising the size distribution. The accumulation mode is well defined by a log-normal distribution characterized by σ, $\bar{r}$ and M_v. Values of M_v appear to increase with values of $\bar{r}$. This is caused by an increase in particle number with increasing $\bar{r}$ for $\bar{r}$ less than 0.34 μm, and it is a result of the $\bar{r}^3$ dependence of M_v. No clear relationship could be found between σ and the other model variables. An apparent relationship between M_v and the volume concentration of particles in the coarse particle mode V is probably the result of the different air mass types present during the study.

2) The values of M_v measured in the mixing layer

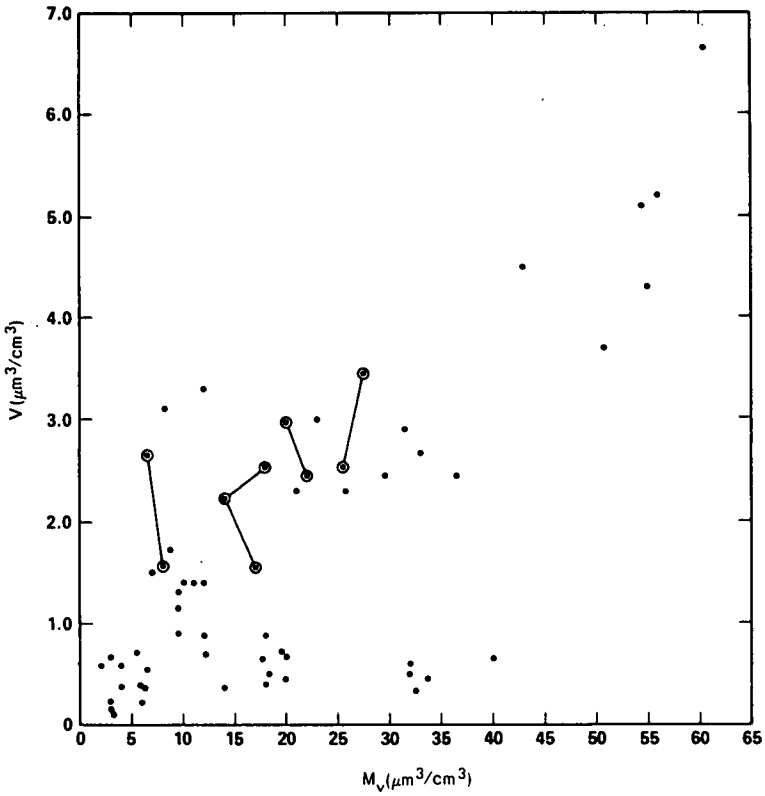

FIG. 8. The volume concentration of particles in the coarse particle mode V as a function of maximum volume in the accumulation mode M_v for data collected within the mixing layer. The connected points show typical variations occurring over a period of 2–3 h at a particular site and altitude.

appear well correlated with the measured values of the volume scattering coefficient.

3) The existence of an accumulation mode was confined to the mixing layer for the majority of the cases studied. During the winter season for conditions of good visibility in a maritime airmass, however, the particle counts were generally so low in the mixing layer that a distinct accumulation mode was not evident.

4) Within the mixing layer the value of M_v is not always constant with altitude, but may depend on the stability of the layer and the strength of the capping inversion.

5) Size distribution models for a specific air mass type which change only the total number of particles may not always be correct. Significant changes in $\bar{r}$ with changing M_v for a given air mass were observed. Work is currently underway to improve the determination of air mass type and to better understand its influence on the properties of the two modes.

6) The coarse particle mode was not confined to the mixing layer. It is interesting that haze layers above the mixing layer were found to have a distinct coarse particle mode but, generally, no accumulation mode. Its difficult to determine the origin of these layers which may be a specific source, or they may simply be aged aerosols.

7) The aerosol measurements probably represent a low humidity or dry particle distribution due to evaporation in the intake plumbing. Its likely that the shape of the distribution of each mode was preserved because of the small range in radius spanned by each of the two modes. Each of the modes may have been affected differently, however, due to differences in particle size and possible differences in chemical composition.

The rest of the aerosol data collected in northern Europe are being studied at present. With the added data set, which is approximately twice as large as was used in this investigation, attention will be focused on how the characteristics of the accumulation and coarse particle modes change with air mass type and season. Techniques to better determine σ for the accumulation mode and M_v, $\bar{r}$ and σ for the coarse particle mode are being developed. In addition, the modeling of these modes at different altitudes in the lower troposphere based on a knowl-

edge of the inversion height, volume scattering coefficient and air mass type is being pursued.

Acknowledgments. The authors wish to thank Maj. John D. Mill, Mr. Eric Shettle and Dr. Robert Fenn for their helpful comments and suggestions. The support for this investigation, which was provided by the Air Force Geophysics Laboratory under Contract F19628-78-C-0200, is gratefully acknowledged.

REFERENCES

Aitchison, J., and J. A. C. Brown, 1957: *The Lognormal Distribution*. Cambridge University Press, 176 pp.

Blifford, I. H., Jr., and L. D. Ringer, 1969: The size and number distribution of aerosols in the continental troposphere. *J. Atmos. Sci.*, **26**, 716–726.

Cooke, D. D. and M. Kerker, 1975: Response calculations for light scattering aerosol particle counters. *Appl. Opt.*, **14**, 734–739.

Dave, J. V., 1978: Extensive data sets of the diffuse radiation in realistic atmospheric models with aerosols and common absorbing gases. *Solar Energy*, **21**, 361–369.

Deirmendjian, D., 1969: *Electromagnetic Scattering on Spherical Polydispersions*. Elsevier, 290 pp.

Junge, C. E., 1963: *Air Chemistry and Radioactivity*. Academic Press, 382 pp.

Laulainen, N. S., A. J. Alkezweeny and J. M. Thorp, 1978: Simultaneous aerosol size distribution and turbidity measurements over St. Louis during METROMEX 1975. *J. Appl. Meteor.*, **17**, 615–626.

Liu, B. Y. H., R. N. Berglund and J. K. Agarwal, 1974: Experimental studies of optical particle counters. *Atmos. Environ.*, **8**, 717–732.

Quenzel, H., 1969: Influence of refractive index on the accuracy of size determination of aerosol particles with light-scattering aerosol counters. *Appl. Opt.*, **8**, 165–169.

Shettle, E. P., 1975: Comment on "Atmospheric aerosol size spectra: Rapid concentration fluctuations and bimodality" by T. E. Graedel and J. P. Franey. *J. Geophys. Res.*, **80**, 3050–3051.

Takashima, T., 1975: A new approach of the adding method for the computations of emergent radiation of an inhomogeneous plane-parallel planetary atmosphere. *Astrophys. Space Sci.*, **36**, 319–328.

Van de Hulst, H. C., 1957: *Light Scattering by Small Particles*. Wiley, 470 pp.

Whitby, K. T., R. B. Husar and B. Y. H. Liu, 1972: The aerosol size distribution of Los Angeles smog. *J. Colloid Interface Sci.*, **39**, 177–204.

Whitby, K. T., 1978: The physical characteristics of sulfur aerosols. *Atmos. Environ.*, **12**, 135–159.